

POLISH ACADEMY OF SCIENCES – WROCLAW BRANCH
WROCLAW UNIVERSITY OF TECHNOLOGY

ARCHIVES OF CIVIL AND MECHANICAL ENGINEERING

Quarterly
Vol. IX, No. 1

WROCLAW 2009

EDITOR IN CHIEF

ZBIGNIEW GRONOSTAJSKI

EDITORIAL LAYOUT AND PROOF-READING

WIOLETTA GÓRALCZYK

TYPESETTING

SEBASTIAN ŁAWRUSEWICZ

SECRETARY

WIOLETTA GÓRALCZYK

Publisher: Committee of Civil and Mechanical Engineering
of Polish Academy of Sciences – Wrocław Branch,
Faculty of Civil Engineering and Faculty of Mechanical Engineering
of Wrocław University of Technology

© Copyright by Oficyna Wydawnicza Politechniki Wrocławskiej, Wrocław 2009

OFICyna WYDAWNICZA POLITECHNIKI WROCLAWSKIEJ

Wybrzeże Wyspiańskiego 27, 50-370 Wrocław

<http://www.oficyna.pwr.wroc.pl>

e-mail: ofiewyd@pwr.wroc.pl

ISSN 1644-9665

Drukarnia Oficyny Wydawniczej Politechniki Wrocławskiej. Zam. nr 160/2009.

Contents

D. M. FARSHCHI, M. MOTAVALLI, A. SCHUMACHER, M.S. MAREFAT, Numerical modeling of in-plane behaviour of URM walls and an investigation into the aspect ratio, vertical and horizontal post-tensioning and head joint as a parametric study	5
B. HOŁA, Methodology of estimation of accident situation in building industry	29
J. HOŁA, M. KSIĄŻEK, Research on usability of sulphur polymer composite for corrosion protection of reinforcing steel in concrete	47
W. HUFENBACH, J. JASCHINSKI, R. GOTTWALD, B.-A. BEHRENS, M. DEMIR, Investigations on the applicability of chemically deposited Ni-shell tools for deep-drawing processes	61
M. HYRCZA-MICHALSKA, F. GROSMAN, The evaluate of laser welded tailor and tubular blanks formability for automotive vehicle elements stamping	69
T. KISILEWICZ, Glazed building wall as a solar thermal collector	83
A. PLEWIŃSKI, T. DRENGER, Spinning and flow forming hard-to-deform metal alloys	101
K. P. SOLEK, A. ŁUKASZEK-SOLEK, R. KUZIĄK, Rheological properties of alloys near solidus point intended for thixoforming	111
M. SZATA, G. LESIUK, Algorithms for the estimation of fatigue crack growth using energy method	119
H. WOŹNIAK, The results of the so far performed investigations of Al-Cu butt cold pressure welding by the method of upsetting	135

Spis treści

D. M. FARSHCHI, M. MOTAVALLI, A. SCHUMACHER, M.S. MAREFAT, Numeryczne modelowanie płaskiego zagadnienia pracy ścian URM oraz analiza ich nośności z uwzględnieniem wpływu pionowych i poziomych stężeń oraz kotew czołowych	5
B. HOŁA, Metodyka oceny wypadkowości w budownictwie	29
J. HOŁA, M. KSIĄŻEK, Badania przydatności polimerowego kompozytu siarkowego do ochrony przed korozją stali zbrojeniowej w żelbecie	47
W. HUFENBACH, J. JASCHINSKI, R. GOTTWALD, B.-A. BEHRENS, M. DEMIR, Badania przydatności nanoszonych chemicznie powłok niklowych na narzędzia stosowane w procesach głębokiego tłoczenia	61
M. HYRCZA-MICHALSKA, F. GROSMAN, Ocena podatności wsadów w postaci blach i rur spawanych laserowo do tłoczenia elementów pojazdów samochodowych	69
T. KISILEWICZ, Przeszkłona ściana jako kolektor energii słonecznej dla budynku	83
A. PLEWIŃSKI, T. DRENGER, Wyoblanie i zginięcie obrotowe trudno odkształcalnych stopów metali	101
K. SOLEK, A. ŁUKASZEK-SOLEK, R. KUZIĄK, Własności reologiczne stopów metali formowanych tiksotropowo w temperaturach bliskich punktowi solidus	111
M. SZATA, G. LESIUK, Algorytmy szacowania wzrostu pęknięć zmęczeniowych metodą energetyczną	119
H. WOŹNIAK, Wyniki dotychczasowych badań spajania doczołowego na zimno Al-Cu metodą spęczania	135



Numerical modelling of in-plane behaviour of URM walls and an investigation into the aspect ratio, vertical and horizontal post-tensioning and head joint as a parametric study

DARYUSH MAHJOOB FARSHCHI, MASOUD MOTAVALLI

School of Civil Engineering, University of Tehran, P.O. Box 11365-4563, Iran

EMPA, Swiss Federal Laboratories for Materials Testing and Research, Structural Engineering Research Laboratory, Ueberlandstrasse 129, 8600 Dübendorf, Switzerland

ANN SCHUMACHER

EMPA, Swiss Federal Laboratories for Materials Testing and Research, Structural Engineering Research Laboratory, Ueberlandstrasse 129, 8600 Dübendorf, Switzerland

MOHAMMAD SADEGH MAREFAT

School of Civil Engineering, University of Tehran, P.O. Box 11365-4563, Iran

Masonry is a complex composite material with non-linear material properties, which make the numerical investigation of its structural behaviour a difficult task. In this paper, a micro non-linear model created using a general purpose finite element code, is discussed with respect to its ability to simulate the in-plane behaviour of unreinforced masonry walls. That is, the capability of model in predicting the cracking, crushing, and sliding phenomena, as well as the global-orthotropic behaviour of previously tested masonry walls are examined. The model is then used within a parametric study to investigate the effect of different aspect ratios, vertical and horizontal post-tensioning as well as the effect of head joints on the capacity of the masonry walls. It will be shown that, while enhancing the lateral in-plane strength of the masonry walls, vertical post-tensioning can also reduce their ductility. On the contrary, horizontal post-tensioning can cause a small reduction in the initial stiffness and yielding shear force of the masonry walls, but increases their integrity, thereby preventing them from sliding and shear failure. Furthermore, it will be shown that, in spite of having a significant influence on local behaviour, head joints do not influence the global behaviour of the masonry walls.

Keywords: *post-tensioning, in-plane behaviour, aspect ratio, masonry*

1. Introduction

There are many masonry structures throughout the world that have been built in the past decades and lack sufficient strength and enough ductility to resist strong ground motions and heavy live loads. To assess vulnerability of such structures, and to examine the efficiency of different retrofitting methods, a numerical tool is needed that can take into account non-linear behaviour and orthotropic characteristics of masonry. Various authors have carried out different numerical analyses on masonry buildings [e.g. 1–6]. An elastic homogenized macro model was used to study the

behaviour of different masonry structures [1–3]. The model did not deal with nonlinear characteristics of masonry materials. Luciano et al. [4] carried out both experimental and numerical studies on masonry arches under vertical loading before and after reinforcing by fibre composite materials. Four different material models were used for the masonry bricks: a linear-elastic model, a no-tension model, an elasto-plastic model and an isotropic damage model. The plastic hinges were specified by the tests and simulated by the brittle cut-off (no-tension) model in the numerical analyses. The linear-elastic model was able to simulate the behaviour of wall at very low field stress. The second model was not able to predict compressive failure. The elasto-plastic model was able to describe the behaviour in compression, but was not successful in reproducing the tensile response of the bricks. By applying the damage model to the bricks, the response of the reinforced masonry arch could be simulated satisfactorily.

Gambarotta and Lagomarsino [5, 6] proposed a model that took into account both mortar damage and brick-mortar debonding. The authors used this model in two different approaches, first [5], interfaces located in the bed joints and head joints were described by the damage model. Compressive failure was considered by assuming an elastic limit condition in the bricks based on Von Mises criterion that the parameter selecting the limit state surface is obtained with reference to the failure under simple compression. In the second approach [6], a continuum model based on an equivalent stratified medium made up of two typical layers was developed: one layer represented the mortar bed joint and another layer represented the brick units and head joints. The constitutive equations for masonry were obtained through a homogenization procedure involving the abovementioned damage model for the bed joints and simple damage constitutive equations for brick layers neglecting the head joints. In the latter approach only the vertical compressive strain in bricks was taken into account because the inelastic vertical extension in the masonry is localized in the bed joint due to their low strength in comparison with the tensile strength of the bricks. These simple assumptions for the brick constitutive model may be supported due to the fact that the collapse mechanisms of shear masonry walls are first characterized by the failure in mortar bed joints and successively, after a wide inelastic phase, by the brick failure [6]. Of the two approaches, the second one requires much less computations while having similar results relative to the first approach and to the experiments.

Despite valuable results, the above numerical models are generally either oversimplified, thereby ignoring some aspects of the complex nature of masonry, or too complex to be used as a general tool. In the present study, a numerical model is introduced that uses the general multi purpose finite element (FE) code, ANSYS [7], and takes into account the non-linear behaviour and complex nature of masonry walls such as cracking, sliding, and crushing. The numerical model is verified by two series of independent tests and its results will be compared to the predictions by the theoretical results. The model is then used to evaluate the effects of aspect ratio (ratio

of height to length), vertical and horizontal post-tensioning and head joints on the in-plane behaviour of masonry walls.

2. Failure mechanisms and material models for plain masonry

Masonry wall is a composite structure that consists of brick and mortar. The geometry and layout of joints play an essential role in the response of the wall and in the mechanism of failure. Figure 1 shows different in-plane failure modes for masonry walls.

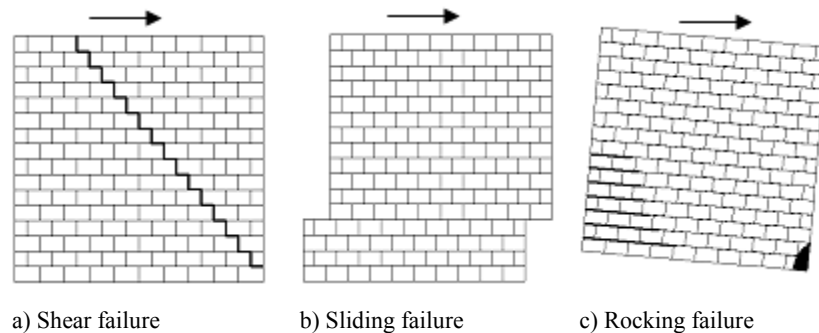


Fig. 1. In-plane failure mechanisms of masonry walls

Several researchers have proposed failure criteria for masonry material [e.g. 8–14]. Malyszko [8] proposed three simple forms of the in-plane shear failure of masonry specimens. Accordingly several tests have been carried out in order to determine the strength parameters and failure surfaces. Ali and Page [9] suggested a micro finite element model for masonry considering elastic elements for bricks and link elements for horizontal mortar joints. An envelope of the shear and compressive strength was defined for bond failure of the joints based on experimental data. Although this model could present global nonlinear behaviour of masonry walls and crack distribution, but it could not predict the failure in bricks and mortar and the effect of multi axial stresses on the response. Assuming isotropic behaviour, Wawrzynek and Cincio [10] applied a brittle isotropic model to analyze masonry subjected to cyclic or dynamic loading. In the study, a biaxial envelope of the load capacity as a function of the principal stresses was used to define masonry failure. The model was fairly successful; however, the authors suggested that it should be modified for material with orthotropic properties like masonry. Ganz [11] also presented failure criteria for masonry under biaxial compressive stresses, neglecting the tensile strength (Figure 2). The failure criteria could be described by five mechanisms: tensile, compressive and shear failure of the bricks and tensile failure and sliding of the mortar joints. The failure criteria has been derived based on the tests and neglects the tensile strength of masonry [11].

In another study, Kumar and Bhandari [12] developed a two-dimensional, non-linear finite element model for the analysis of masonry arches. The model took into

account non-linearity in stress-strain relationship and cracking of masonry. The model was not able to replicate accurately the experimental behaviour, but could capture the crushing and cracking zones in the arches. Litewka and Szojda [13] supplied new experimental data for brittle material subjected to triaxial state of stress as well as presentation of the theoretical model capable to describe deformability and failure of initially isotropic brittle rock-like solids. In their study, the stress-strain curves and stress at failure were determined experimentally for cylindrical specimens of mortar under tri-axial state of stress. These experimental results showed a good agreement with the theoretical predictions obtained from the own theoretical model based on the methods of the damage mechanics.

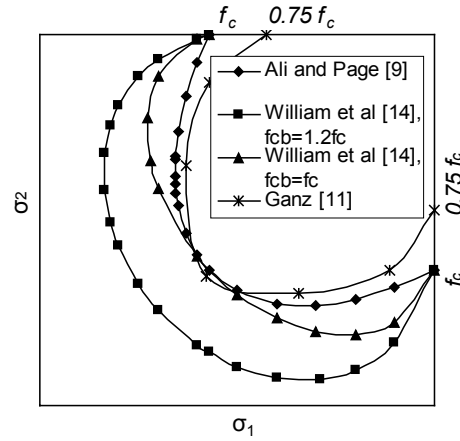


Fig. 2. Masonry failure surfaces for compression proposed by various authors

Willam and Warnke [14] developed a constitutive model for tri-axial behaviour of concrete, which can be used to simulate the nonlinear response of brittle materials such as masonry. This theory has been used in the present work and is discussed in some details. The model considers multi axial stresses of brittle material and takes into account cracking, crushing and sliding phenomena by reflecting their effects on the stiffness matrix [7–14]. The failure criterion is expressed in the following form:

$$\frac{F}{f_c} - S > 0, \quad (1)$$

where:

- F – a function of the principal stresses,
- f_c – uni-axial compressive strength,
- S – expresses the failure surface.

The failure surface S is a function of principal stresses in addition to the tensile, uni-axial and biaxial compressive strengths (f_t , f_c and f_{cb}). The failure surface defined by

Equation (1) is formulated for each condition of principal stresses [7, 14]. The element considers a smeared crack analogy for cracking in tension zones and a plasticity algorithm to account for possibility of crushing in compression zones. Formation of a crack is achieved by modification of the stress-strain relationships of the element to introduce a plane of weakness perpendicular to stress direction. An amount between full shear transfer and no shear transfer may be used as the ability of a crack to transfer the shear stress across its plane. When crushing occurs in a section, any further application of load develops increasing strains at constant stress. The Willam and Warnke's failure surface developed for in-plane behaviour, that is, two-dimensional loading, is shown in Figure 2. A three dimensional eight noded solid isotropic element, Solid 65, has been provided in ANSYS [7] to model nonlinear behaviour of the brittle materials based on Willam and Warnke's theory.

3. Experimental studies

Two series of independent tests [15–16] which have been carried out on the masonry walls subjected to in-plane lateral load and their experimental data have been available in details, are used to validate the numerical model described in the next section.

Material specifications, geometry and loading details of the wall specimens are summarized in Table 1. In this table, thickness, height and length of the specimens are represented by b_w , h_w and l_w .

All specimens were cantilever and the vertical load has been applied uniformly on their upper edge using a concrete slab. In the experiments by Ganz and Thurlimann [15], the vertical load was first applied and kept constant, and then the lateral load was applied incrementally until the failure of the wall. Two of their specimens, W1 and W4, are used in the current study. The specimens tested by ElGawady [16], were subjected to dynamic excitations (i.e. shaking table tests) and axial (vertical) loading was applied to an upper concrete distributing beam using two external bars. Due to lateral deformations, the initial force in the vertical bars increased during the tests (shown by $P1$ (initial force) and $P2$ (force at end of test) in Table 1). Results from ElGawady's three unreinforced masonry specimens, consisting of two specimens with the aspect ratio (ratio of height to length) of 1.0 (L1 and L2) and one specimen with the aspect ratio of 0.4 (S2), will be used below.

4. Numerical modelling of plain masonry walls

A numerical micro model is created using the general purpose finite element code ANSYS [7]. All brick units and joints are considered in this model. Vertical joints (head joints) are represented by Solid 65 element with smeared cracks pattern of failure. Bed joints are modelled by Contact 52 element to simulate discrete cracking at failure. This may be justified by considering the low tensile strength of the bed joints and due to the fact that the shear strength of the masonry is defined as a combination of

low initial shear strength under zero compressive stress and increment in the strength induced by the compressive stress perpendicular to shear.

Table 1. Specifications of masonry wall specimen

Ref.	Wall specimen	Dimensions of sample ($l_w \times h_w \times b_w$) (m)	Axial load (kN)		Eccentricity (mm)	$E_{X-masonry}$ (MPa)	Thickness of joints (mm)	Size of bricks (mm)	Compressive strength (MPa)			Tensile strength (MPa)			Type of lateral loading
			P1	P2					Brick	Mortar	Masonry	Brick	Mortar	Masonry	
Ganz (1984)[15]	W1	3.6×2.0×0.15 (Thickness of flanges is 0.6) Aspect ratio 0.56	415	415	-	2460	10	300×190×150 Concrete blocks	37.4	23.9	7.61	9.1	5.5 to 6.3	.05	Monotonic
Ganz (1984)[15]	W4	3.6×2.0×0.15 (Thickness of flanges is 0.9) Aspect ratio 0.56	423	423	840	2460	10	300×190×150 Concrete blocks	37.4	23.9	7.61	9.1	5.5 to 6.3	.05	Monotonic
ElGawady (2004) [16]	L1	1.6×1.6×0.075 Aspect ratio 1.0	30	90	-	1044	10	160×100×75 Clay blocks	14.8	8.9	7.7	-	-	-	Dynamic (Time -history)
ElGawady (2004) [16]	L2	1.6×1.6×0.075 Aspect ratio 1.0	31	44	-	855	10	160×100×75 Clay blocks	14.8	3.3	5.7	-	-	-	Dynamic (Time -history)
ElGawady (2004) [16]	S2	1.6×0.7×0.075 Aspect ratio 0.44	30	38	-	855	10	160×100×75 Clay blocks	14.8	3.3	5.7	-	-	-	Dynamic (Time -history)

Contact 52 is defined by axial and sliding stiffness and supports tangential sliding based on Coulomb theory of friction, where sliding is eliminated when the element surface is under tensile axial force greater than the tensile strength of the mortar bed joints. Due to relatively low stress level, the brick units are simulated by an elastic solid element (the same procedure has been used by other authors [17]), Solid 45, and failure of brick units is examined manually based on Willam and Warnke's theory. Details of the meshing used in the model are illustrated in Figure 3.

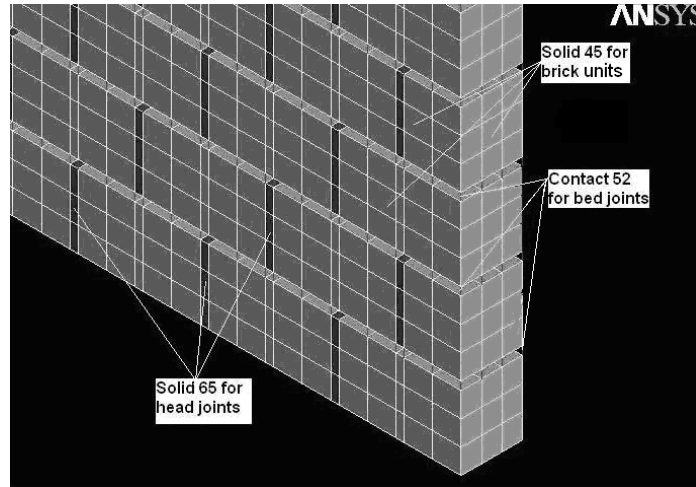


Fig. 3. Details of meshing used in the numerical model

Material properties used in the model are driven from the test results and are given in Table 2. The compressive strength of the masonry constituents (f_{cb} and f_{cm}) were selected based on existing experimental measurements for all specimens (see Table 1). For Specimens L1, L2 and S2, due to lack of experimental measurements, the tensile strength (f_{tb} and f_{tm}) were assumed to be approximately 10 to 15 % of the compressive strength based on recommendations given in the literature [e.g. 18]. The sliding stiffness (KS) of the contact elements used in the bed joints can be calculated from the lateral drift observed in the tests. E modulus of mortar used in the head joints is then determined based on KS . Evaluating the E modulus of the masonry from the test results and considering the same stress in all components, the E modulus of the bricks is determined [16]:

$$E_m = E_{\text{masonry}} E_b / ((th_b / th_m)(E_b - E_{\text{masonry}}) + E_b), \quad (2)$$

where:

E_{masonry} , E_b and E_m are the elastic modulus of the masonry, brick and mortar,
 th_{brick} and th_{mortar} are the thickness of the bricks and mortar joints, respectively.

The axial stiffness can be evaluated based on vertical deformation observed in the tests. The coefficient of friction (μ) was estimated based on Coulomb theory through division of the base shear force of the yield point of the force-deformation curve by the corresponding axial (vertical) force, both recorded during the tests [15–16].

Table 2. FE model specifications

Specimen	Bricks			Head joints			Bed joints		
	f_{cb} (MPa)	f_{tb} (MPa)	E_b (MPa)	f_{cm} (MPa)	f_{tm} (MPa)	E_m (MPa)	KN (N/m)	KS (N/m)	μ
W1&W4	37.4	9.1	3600	23.9	2.5	400	400E6	120.E6	0.7
L1	14.8	2	2000	8.9	0.8	197	56E6	18E6	0.4
L2	14.8	2	2000	3.3	0.45	70	19E6	5.5E6	0.4
S2	14.8	2	2000	3.3	0.45	70	19E6	5.5E6	0.7

Nonlinear analyses are carried out using Newton Raphson approach. The simulation involves application of incremental and monotonic horizontal deformation to the top of the walls. Axial load is applied to different specimens in accordance to the tests. For Specimen W1, axial load is kept constant with uniform distribution. For Specimen W4, which has been subjected to an eccentric axial point load in the test (see Table 1), the upper concrete beam is also considered in the model. It is reiterated that in Specimens L1, L2 and S2, due to flexural cracking, the height of the walls increases and this causes significant fluctuations in the post-tensioning force [16] (compare $P1$ with $P2$ in Table 1). For recent specimens, axial load at each load step is adjusted based on experimental records [16]. Loading and boundary conditions used in the model are illustrated in Figure 4.

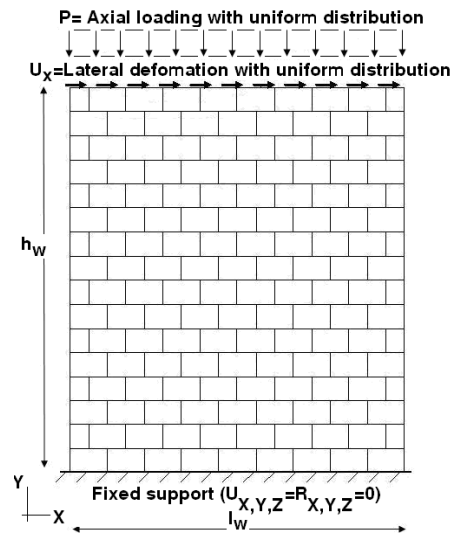


Fig. 4. Loading scheme and boundary conditions used in the numerical model

Figures 5 to 7 illustrate the responses of different walls in terms of top lateral load versus top lateral deformation. All curves involve two main branches: before yield and post yield. A relatively sharp slope and almost linear shape of initial part indicate a relatively stiff and almost elastic response of the walls before yield. The yield point corresponds to the beginning of sliding deformation in the bed joints. After yield, the walls experience relatively sharp decline in stiffness but relatively stable and consistent behaviour up to the last load step. The last load step is that of the tests, which for Specimens W1 and W4, corresponds to the onset of crushing at the toes of walls. It should be stated that the deformation seen for the ElGawady's unreinforced specimens corresponds to a predefined degree of damage and not to wall failure. This was done in order to apply retrofitting measures for further testing. As can be observed, the initial and post-yield stiffnesses, the shear strength corresponding to the last load step, and the value of ductility are in close agreement with test results for all specimens. As given in Table 1, the specimens are different in such specifications as mechanical properties of the bricks and mortar, type and eccentricity of axial load (in Specimen W4, axial load is a point load with an eccentricity of 850 mm while in the other four specimens, axial load is uniformly distribution), sectional geometry (the section of specimens tested by ElGawady and by Ganz are I shape and rectangular, respectively) and aspect ratio. Despite various characteristics, Figures 5 to 7 demonstrate that the model has been successful in simulating the test results. For instance, Specimens L1 and L2 are similar in geometry, but, due to higher axial load and stiffer mortar, the post-yield stiffness and the shear strength are greater in Specimen L1. As another example, Specimen S2 has smaller aspect ratio (0.4) compared to Specimen L2 (1.00). This causes higher stiffness, and therefore, larger shear force in S2 relative to L2 under identical lateral deformation, as is seen in the figures.

In addition to behaviour, the numerical model has predicted the nature of damage at different load levels. A comparison between tests and numerical results is presented in Table 3. It is seen that the nature of cracks and pattern of damage are in agreement with the numerical simulation. For all specimens, the simulation indicates that flexural cracks form initially at the most bottom bed joint, and, as lateral load increases, the cracks propagate upwards (see Table 3). In parallel to flexural cracks, damage is accompanied by sliding deformation over a large length of the bed joints when lateral deformation reaches the yield point. Beyond this point, step pattern shear cracks are observed in the model, which start at the bottom corner of all walls and proceed upwards as lateral load increases. It can be seen that in Specimen W4, due to eccentric point axial load, flexural cracks are more extensive and the damage of the head joints is shifted to those located in the wall end close to the axial load, relative to W1. In the specimens with larger axial load (e.g. L1), flexural and shear cracks are not as extensive as L2. For Specimen S2, due to smaller aspect ratio, and therefore, smaller flexural moment, there are considerably fewer flexural and shear cracks relative to Specimen L2.

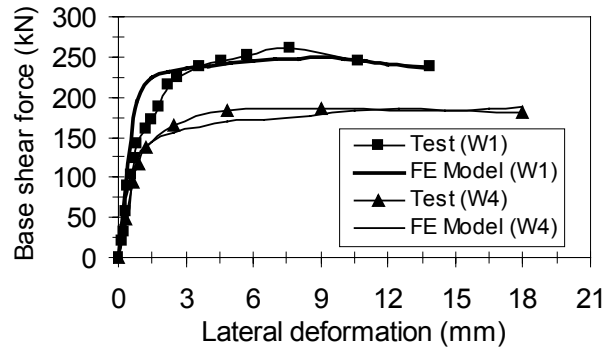


Fig. 5. Numerical and test results of Specimens W1 and W4

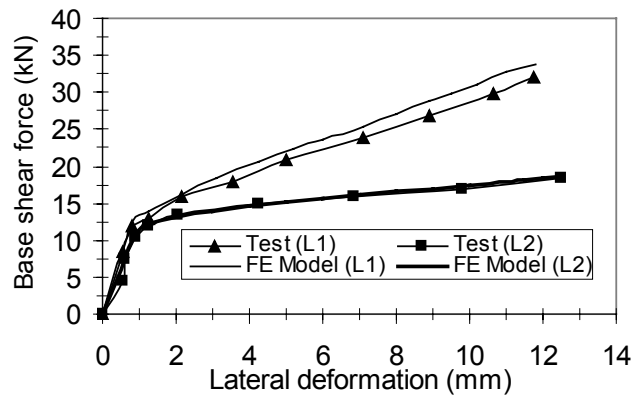


Fig. 6. Numerical and test results of Specimens L1 and L2

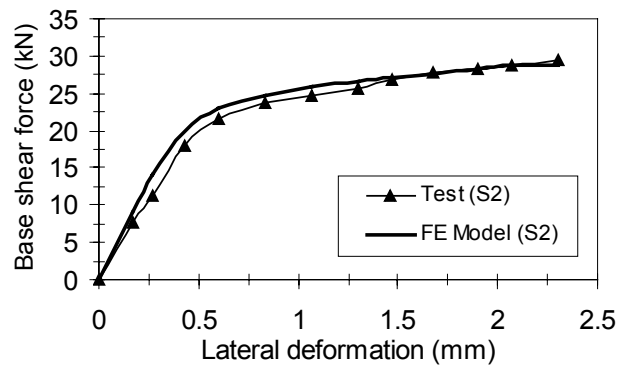
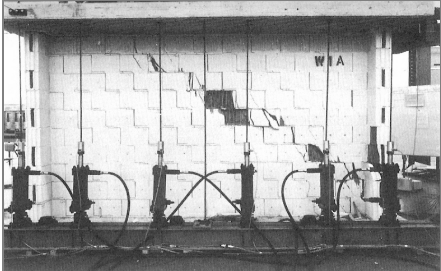
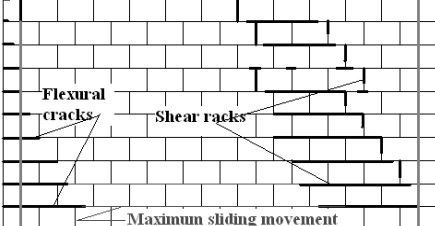

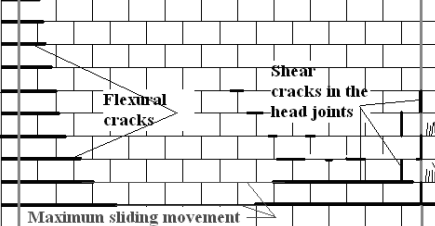
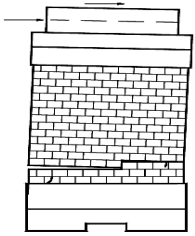
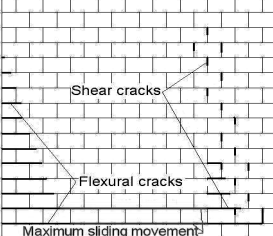
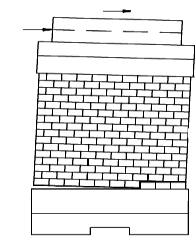
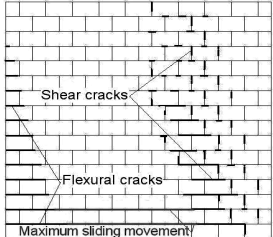
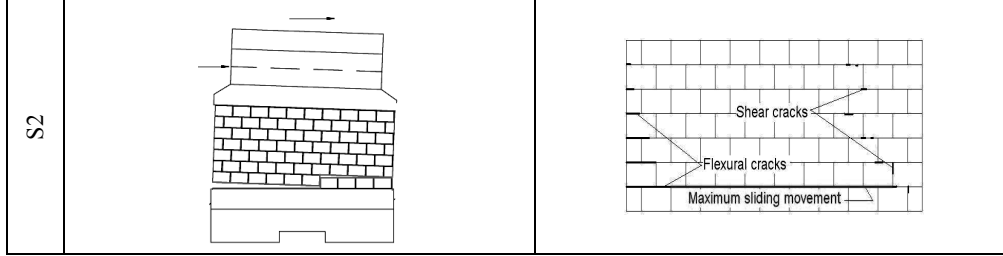


Fig. 7. Numerical and test results of Specimen S2

Manual control indicates that the brick units have remained undamaged throughout numerical simulation for Specimens L1, L2 and S2, while crushing occurs at the toes of W1 and W4 at the last load step. This can be confirmed by the test results.

Table 3. Pattern of damage in different specimens

Specimen	Test results	Numerical model results
W1		
W4		
L1		
L2		



5. Comparison with theoretical relationships

In this section, the numerical results obtained by the above finite element model has been compared to theoretical relationships. The analytical relations proposed in [19] have been used which are summarized in Table 4. Sliding shear strength (V_{sliding}) may be defined by Coulomb friction law and depends on the amount of axial load, aggregate interlock and the quality of the interface between the brick units and mortar in the horizontal bed joints. The shear strength corresponding to the first cracking (V_{cr}^c) may be evaluated simply when the tensile stress surpasses the tensile strength at a wall end (see Table 4). As this table shows, for shear strength corresponding to the nominal flexural strength of the wall (V_n), the ultimate limit state method is used by assuming a length of a for the equivalent rectangular stress block with a stress of $0.85f'_m$ (f'_m is the compressive strength of masonry) and an extreme fibre strain of $\epsilon u = 0.003$ for unconfined masonry. In Table 4, tensile strength, Poisson ratio, moment of inertia, area, and initial moment of the specimens are represented by f_t , ν , κ , I_w , A_w and M_1 . As recommended in [19], a reduction factor of 0.5 is used to estimate the effective moment of inertia and area ($I_{w,eff}$ and $A_{w,eff}$). The other parameters have been defined in the previous sections.

Table 4. Analytical relations for masonry walls [19]

Shear sliding strength	$\tau = \tau_i + \mu \cdot \sigma_v$; $V = \tau \cdot A_w$; $0 < \tau_0 < 1.5MPa$; $0.3 < \mu < 1.2$; $\sigma_v = P / A_w$
Cracking flexural strength	$M_{cr} = [f_t + P/(A_w) - M_1(0.5 \cdot l_w) / I_w] \cdot I_w / (0.5 \cdot l_w)$; $V_{cr} = M_{cr} / h_w$
Nominal flexural strength	$P = \alpha \cdot f'_m \cdot b_w \cdot a$; ($\alpha = 0.85$); $M_n = P \cdot (l_w / 2 - a / 2)$; $V_n = M_n / h_w$
Corresponding deformation to cracking strength	$d_{cr} = V_{cr} \cdot [h_w^3 / (3E_{\text{masonry}} \cdot I_w) + 2(1 + \nu) \cdot \kappa \cdot h_w / (E_{\text{masonry}} \cdot A_w)] +$ $M_1 \cdot h_w^2 / (2 \cdot E_{\text{masonry}} \cdot I_w)$
Corresponding deformation to nominal strength	$d_n = V_n \cdot [h_w^3 / (3E_{\text{masonry}} \cdot I_{w,eff}) + 2(1 + \nu) \cdot \kappa \cdot h_w / (E_{\text{masonry}} \cdot A_{w,eff})] +$ $M_1 \cdot h_w^2 / (2 \cdot E_{\text{masonry}} \cdot I_{w,eff})$

Table 5 presents a comparison among numerical, test and theoretical predictions for strength and deformation corresponding to the cracking and ultimate states. Neglecting the tensile strength of masonry, geometry and other mechanical properties of the specimens needed for the analytical relationships are chosen based on the information given in Table 1. As mentioned in the previous sections, during the tests of Specimens L1, L2 and S2, axial load has increased by increasing in the lateral loading. In order to calculate the shear strength and deformation corresponding to the first cracking state, represented by V_{cr}^c and d_{cr}^c in Table 5, a constant axial load corresponding to the first cracking state (P_{cr}) was chosen from the experimental records [16] and used in the model and theoretical relations.

Table 5. Comparison among numerical and test results and predictions by analytical relations

Specimen	Model predictions							Test results				Theoretical Predictions								
	P_{cr}	V_{cr} (kN)	V_{cr}^c (kN)	V_{max} (kN)	d_{cr} (mm)	d_{cr}^c (mm)	d_{max} (mm)	V_{cr} (kN)	V_{max} (kN)	d_{cr} (mm)	d_{max} (mm)	$V_{sliding}$ (kN)	V_{cr}^c (kN)	V_n (kN)	d_{cr}^c (mm)	D_n (mm)	$[V_{cr}^c]_{theory} - V_{cr}^c]_{model} / V_{cr}^c]_{theory}$ (%)	$[V_{max}^c]_{theory} - V_n]_{model} / V_{max}^c]_{theory}$ (%)	$[d_{cr}^c]_{theory} - d_{cr}^c]_{model} / d_{cr}^c]_{theory}$ (%)	
S2	40	415	19.89	14.215	28.8	0.433	0.27	2.3	20	29	0.4	2.3	33.6	15.24	40.6	0.38	2.50	6.73	14.29	28.9
	40	423	19.5	14.215	18.67	0.81	0.53	12.5	11	17.3	0.9	125	20.8	6.7	20.86	.70	5.1	-10.94	10.24	24.28
L2	42	147.8	12.4	8.123	33.8	0.7	0.4	11.8	10	31.5	0.8	11.8	39.2	7.0	39.3	0.60	7.55	-16.04	13.78	33.3
	42	147.8	19.5	8.123	33.8	0.7	0.4	11.8	10	31.5	0.8	11.8	39.2	7.0	39.3	0.60	7.55	-16.04	13.78	33.3
L1	42	147.8	12.4	8.123	33.8	0.7	0.4	11.8	10	31.5	0.8	11.8	39.2	7.0	39.3	0.60	7.55	-16.04	13.78	33.3
	42	147.8	12.4	8.123	33.8	0.7	0.4	11.8	10	31.5	0.8	11.8	39.2	7.0	39.3	0.60	7.55	-16.04	13.78	33.3
W4	415	234	19.5	19.5	187	0.2	0.2	2.5-18	No data	180	No data	18	296	14.85	194.5	0.29	3.38	23.8	3.86	31.03
	415	234	19.5	19.5	187	0.2	0.2	2.5-18	No data	180	No data	18	296	14.85	194.5	0.29	3.38	23.8	3.86	31.03
W1	415	234	19.5	19.5	187	0.2	0.2	2.5-18	No data	180	No data	18	296	14.85	194.5	0.29	3.38	23.8	3.86	31.03
	415	234	19.5	19.5	187	0.2	0.2	2.5-18	No data	180	No data	18	296	14.85	194.5	0.29	3.38	23.8	3.86	31.03

The minimum amount of sliding and flexural strength predicted by the analytical formula is the lateral shear strength of the wall that has been specified by the bold style in Table 5. The propensity for sliding is highly dependent on the wall aspect ratio. As it can be seen for Specimens L1 and L2 with an aspect ratio equal to 1.0, the sliding and flexural strength are almost the same where for Specimens W1 and S2, the sliding strength is the dominant strength. For Specimen W4, due to large eccentricity

(840 mm) of the axial load, the flexural strength is smaller than the sliding strength and therefore is predominant. This eccentricity causes the first cracking strength to be very small in Specimen W4. The table emphasizes a good agreement between the test and numerical results for all presented items (i.e. V_{cr} , V_{max} , d_{cr} and d_{max}). Furthermore, it can be seen that for all specimens the numerical results obtained for the cracking and maximum shear strength (V_{cr}^c , V_{max} , given in the column of numerical predictions) are in relatively good agreement with the predictions by the analytical relations (V_{cr}^c , V_n , given in the column of theoretical predictions). The maximum deviation occurs for Specimen W1 and is limited to 23.8% (see Table 5). A comparison between the numerical results and also predictions by the analytical relations for the deformation corresponding to the first cracking (d_{cr}^c) is presented in Table 5. It should be added that the shear force and deformation at first crack have not been measured during the experiments of W1 and W4.

Since the masonry specimens experience a significant sliding deformation beyond the yield point of their force-deformation relationship (see Figures 5–7) as well as the flexural and shear deformations, therefore the maximum deformation observed in the model and tests (d_{max}) is larger than values predicted by the analytical relations (d_n). This is more significant for Specimens W1 and W4 which are subjected to a constant axial load whereas for Specimens L1, L2 and S2, the axial load and therefore the sliding strength are increasing by increasing in the lateral deformation. Indeed, the nominal flexural deformation predicted by the analytical relations is only based on the shear and flexural behaviour of the masonry walls and therefore give an underestimation of final deformation. Therefore a logical comparison between d_{max} and d_n is not possible.

6. Parametric study

Using the model, the influence of the aspect ratio, vertical and horizontal post-tensioning and head joints on the in-plane behaviour of masonry walls were investigated. Geometric and material characteristics of specimen L2 (see Table 1) were used for the reference wall. Table 6 presents a summery of characteristics of the specimens used for the parametric study. Each specimen is designated by a name that reflects its characteristics. For instance, L2-AR1.5 means specimen L2 with an aspect ratio of 1.5 or L2-AR1.5-PT0.2 refers to a specimen L2 with an aspect ratio of 1.5 post-tensioned by an axial force equal to 20 percent of its compressive strength.

Table 6. Wall specimens used for parametric study

Specimen	Description
L2	Reference specimen, see Tables 1 and 5
L2-AR0.44	Specimen L2 with aspect ratio of 0.44 (1600×700), other properties are the same as specimen L2.

L2-AR1.5	Specimen L2 with aspect ratio of 1.5 (1600×2400), other properties are the same as specimen L2.
L2-AR0.44-VPT0.2	Specimen L2 with aspect ratio of 0.44 (1600×700) and axial loading equal to 20% of its compressive strength (128.7 kN), other properties are the same as specimen L2.
L2-VPT0.2	Specimen L2 with aspect ratio of 1.0 (1600×1600) and axial loading equal to 20% of its compressive strength (128.7 kN), other properties are the same as specimen L2.
L2-AR1.5-VPT0.2	Specimen L2 with aspect ratio of 1.5 (1600×2400) and axial loading equal to 20% of its compressive strength (128.7 kN), other properties are the same as specimen L2.
L2-HPT0.2	Specimen L2 with horizontal post-tensioning equal to 20% of its compressive strength (128.7 kN), other properties are the same as specimen L2.
L2-VPT0.2-HPT0.2	Specimen L2 with vertical and horizontal post-tensioning both equal to 20% of its compressive strength (128.7 kN), other properties are the same as specimen L2.
L2-VPT0.2-HPT0.05	Specimen L2 post-tensioned in the vertical and horizontal directions by a force of 20% of its compressive strength (128.7 kN) and 5% of its compressive strength (32 kN) respectively. Other properties are the same as specimen L2.
L2-E-HJ	Specimen L2 with elastic behaviour for the head joints
L2-W-HJ	Specimen L2 without considering the head joints

6.1. Aspect ratio

Masonry walls with different aspect ratios exhibit different behaviour when subjected to lateral loading. In this section, the effects of the aspect ratio on the lateral behaviour of masonry walls and the ability of the model to predict this behaviour will be discussed. To do this, the aspect ratio of a reference specimen—wall L2 (see Tables 1 and 2) – was varied and the changes in behaviour due to this variation compared. Three aspect ratios were examined: 0.44 (1600 × 700 mm, specimen L2-AR0.44), 1.0 (1600 × 1600 mm, the actual size of wall L2), and 1.5 (1600 × 2400 mm, specimen L2-AR1.5). The effects of the aspect ratio on the global behaviour of wall L2 obtained from numerical simulations are shown in Figure 8 as a relationship between base shear force and drift. For all specimens, the maximum drift was selected based on the onset of predominant failure predicted by the model (i.e. sliding for L2-AR0.44 and crushing at the toe for L2 and L2-AR1.5).

Figure 8 emphasizes the higher stiffness and larger lateral strength of the masonry wall with a lower aspect ratio. That is, as can be expected, for walls with the same material properties, length and loading conditions, the shorter walls will possess larger lateral strength.

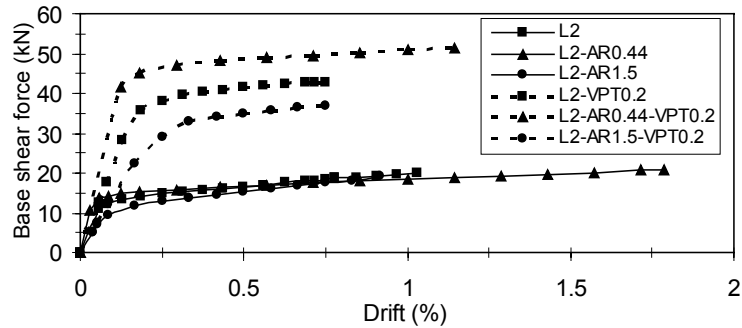
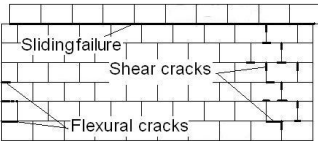
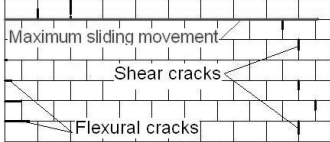
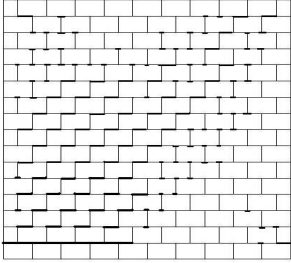
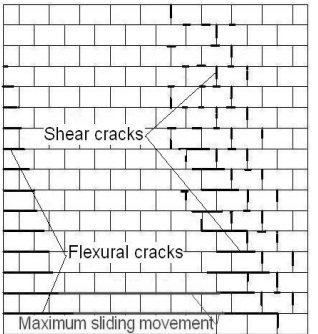
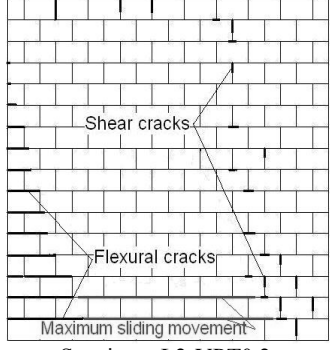
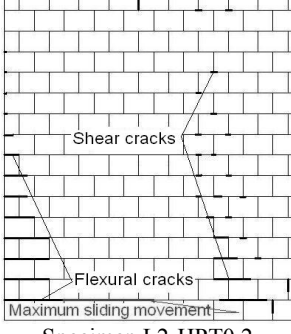


Fig. 8. Effects of the aspect ratio and vertical post-tensioning on the global behaviour of masonry walls predicted by the FE model

Table 7. Effects of the aspect ratio, vertical and horizontal post-tensioning on the crack pattern of masonry walls predicted by the FE model

Aspect ratio	Vertical post-tensioning	Horizontal post-tensioning
 <p>Specimen L2-AR0.44 (last load step)</p>	 <p>Specimen L2-AR0.44-VPT0.2 (last load step)</p>	 <p>Specimen L2-HPT0.2 (first load step)</p>
 <p>Specimen L2 (last load step)</p>	 <p>Specimen L2-VPT0.2. (last load step)</p>	 <p>Specimen L2-HPT0.2 (last load step)</p>

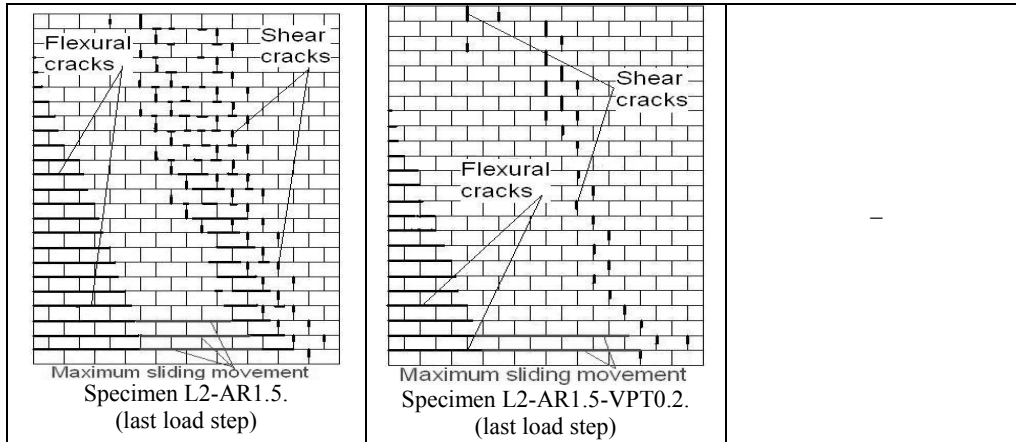


Table 7 shows the crack distribution at the last load step predicted by the model for specimens L2-AR0.44 and L2-AR1.5, respectively. In Table 7 it can be seen that flexural cracks are less prevalent in the squat wall (L2-AR0.44) and, sliding failure is the predominant failure mechanism. This behaviour is expected due to the low height and therefore large lateral stiffness of the wall and can be verified by the theoretical calculations using relations given Table 4. This is in comparison to the reference wall (Specimen L2) where failure was predicted by the model as a combination of shear and flexural cracking. In contrast to this, Table 7 shows that a more slender wall, L2-AR1.5, exhibits predominantly flexural and shear cracking in the bed and head joints. Furthermore, sliding movement, with maximum sliding in the first bed joints, occur in Specimens L2 and L2-AR1.5. In general, for walls with higher aspect ratios (e.g. greater than one), failure can occur due to a combination of shear and flexural cracking. As will be explained in the following section, if the axial load is high enough, flexural failure rather than shear failure can be expected to be the prominent failure mechanism.

6.2. Axial loading

The lateral load carrying capacity of a masonry wall may be increased by post-tensioning, that is, through the application of additional axial (vertical) load to the wall. In order to investigate the effect of this axial load, the model was used again to simulate the behaviour of wall L2 with an additional post-tensioning force of 128.7 kN applied uniformly to the upper edge of the wall. This axial force is approximately 20% of the compressive strength of wall L2 and has been recommended for post-tensioning in “VSL Technical Reports, Series 2” [20]. It should be reiterated that ElGawady tested his un-reinforced specimens (e.g. Specimen L2) to a predefined degree of damage and not to failure in order to apply retrofitting measures for further testing. Therefore, the final deformation and ductility of Specimen L2 given in this section,

has been predicted by the model (are not taken from test results). Analyses were performed for the post-tensioned specimen L2 with varying aspect ratios of 0.44, 1.0 and 1.5. The characteristics of the post-tensioned specimens (referred to as L2-AR0.44-VPT0.2, L2-VPT0.2, and L2-AR1.5-VPT0.2) are given in Table 6.

The effects of post-tensioning on the lateral capacity and strength (global behaviour) of these specimens are also shown in Figure 8. The maximum drift has been selected based on the onset of predominant failure predicted by the model (i.e. crushing in the toe for all post-tensioned specimens). For all specimens, it can be seen that the post-tensioning causes the lateral strength to increase almost twofold in terms of applied base shear, while their ductility decreases about 25 to 30%. The increase is more than double for squat specimen (L2-AR0.44-VPT0.2). It can be said that despite the increase in lateral strength, failure occurs as crushing at the toes at the lower deformations and therefore the ductility is undermined in the post-tensioned walls.

The crack pattern under monotonically increasing lateral load at the last load step is shown in Table 7 for all specimens. When compared with Specimen L2-AR0.44, it is seen that the post-tensioning has caused the failure mechanism to shift from sliding to shear failure. For Specimens L2-AR1.5 and L2-AR1.5-VPT0.2, considerably fewer shear and flexural cracks were seen than were predicted for their reference walls, L2 and L2-AR1.5. Through the decrease in shear cracks, it can be said that the rocking mechanism (see Figure 1c) becomes a more likely failure mode in post-tensioned walls with large aspect ratio. Due to high axial loading, sliding movement decreases for all post-tensioned specimens.

In general, the study on the effect of increased axial load for walls subjected to lateral loads has shown this method can improve the behaviour of the masonry wall and preserve wall integrity. However, in order to augment ductility as well as lateral strength, the toes of post-tensioned specimens should be strengthened appropriately. To do this, the application of fibre reinforcement polymer (FRP) sheets has been suggested by other authors [16, 21].

6.3. Horizontal post-tensioning

Post-tensioning in the horizontal direction is thought to help with wall integrity under lateral loading [22]. In order to examine the effects of horizontal post-tensioning on the in-plane behaviour of the wall, a horizontal load of 128.7 KN, uniformly distributed along the sides of the wall, was applied to wall L2 (specimen L2-HPT0.2), without changing any other model parameters. The boundary conditions of specimen L2-HPT0.2 are given in Figure 9.

The effects of horizontal post-tensioning on the global behaviour are demonstrated in Figure 10. It can be seen that the initial stiffness of L2-HPT0.2 decreases relative to the reference specimen L2. This is due to the fact that the horizontal post tensioning causes vertical deformation (swelling) in the wall and therefore some initial cracks in the bed joints (see Table 7). Furthermore, according to Coulomb's friction law, the

initial swelling negates the effects of the normal compressive stress and therefore the yielding shear strength of L2-HPT0.2 decreases relative to L2. With increasing in the lateral loading, the initial cracks disappear and the flexural cracks and sliding in the bed joints remain as the predominant wall damage (Table 7). For this reason, at the last step of loading, both Specimens L2-HPT0.2 and L2 exhibit the same global behaviour. Furthermore, the shear cracks in the head joints do not occur for L2-HPT0.2 and the shear failure is therefore not as predominant a failure mechanism for this wall (see Table 7). Also, the model shows the maximum sliding movement is remarkably small compared to Specimen L2 and therefore is not significant for L2-HPT0.2. By inhibiting sliding as well as the shear failure mechanisms, it is found that horizontal post-tensioning can increase wall integrity.

The in-plane behaviour of specimen L2 subjected to combined vertical (axial) and horizontal post-tensioning was also investigated and is summarized briefly here. To do this, Specimen L2-VPT0.2 was assumed to be also post-tensioned in horizontal direction in two different cases: horizontal post-tensioning force is equal to 128.7 kN (Specimen L2-VPT0.2-HPT0.2) and 32 kN (Specimen L2-VPT0.2-HPT0.05). The same trend was observed for the global and local behaviour of these specimens. However, as Figure 10 shows due to smaller horizontal post-tensioning force, reduction in the initial stiffness and shear strength of L2-VPT0.2-HPT0.05 is not significant. Therefore it can be said that in order to avoid the above-mentioned deficiencies, the horizontal post-tensioning force should not be chosen very high. Application of larger axial post-tensioning may be used for this. It should be emphasized that the local and global behaviour predicted by the model for the above horizontal post-tensioned specimen are in good agreement with the results reported in [22].

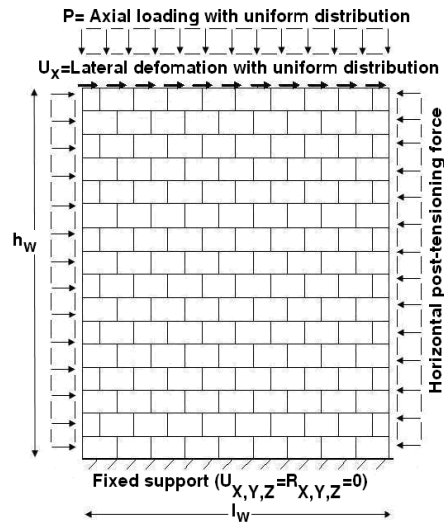


Fig. 9. Loading and boundary conditions used for horizontal post-tensioned specimens

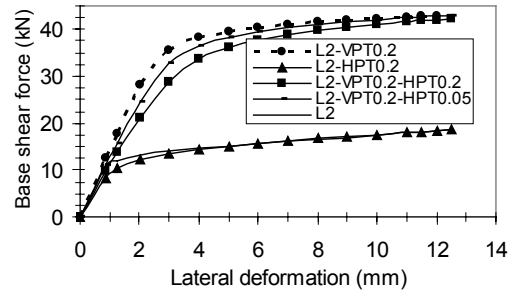


Fig. 10. Effects of horizontal post-tensioning on the global behaviour of Specimen L2 predicted by the FE model

6.4. Head joints

As was discussed above, the head joints in masonry walls play a crucial role in their local in-plane behaviour, in particular, in the case of shear failure. Based on results given in Gambarotta and Lagomarsino [6], the effects of the head joints on the global behaviour of masonry walls are negligible in most standard cases. To investigate this in more detail, specimen L2 was reanalyzed applying the following two conditions: assuming elastic behaviour for the head joints (L2-E-HJ in Table 6) and omitting the head joints (L2-W-HJ in Table 6). For the second case, the head joints were replaced by the brick material. Other specifications of the model were identical to specimen L2.

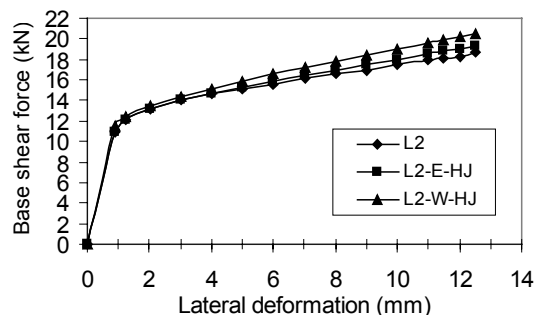


Fig. 11. Effect of the head joints on the global behaviour of Specimens L2 predicted by the FE model

Results obtained by the model are shown in Figure 11. Generally speaking, when compared to results of Specimen L2, the difference for both cases is negligible (less than 10%), but is larger for the case where the head joints are neglected (L2-W-HJ). As can be expected, before the onset of cracking in the head joints, the base shear force-deformation curve obtained by model of L2-E-HJ is identical to that of specimen L2. According to the results of this section, it may be concluded that the head joints do not have a remarkable influence on the global behaviour of the in-plane walls though

the results should be verified for the walls with different aspect ratios or thickness of the joints. That is, the head joints may be omitted or considered elastic without a noticeable reduction in accuracy, when only an overall idea of the wall behaviour is required, for example, for cyclic analyses or practical applications.

7. Conclusions

In this study, a micro model for in-plane behaviour of plain masonry walls has been introduced using the general purpose finite element code, ANSYS. The model accounts for such characteristics as cracking, crushing, and sliding, and incorporates the bed joints, head joints and brick units. The model was used to simulate the results from existing masonry wall tests. In addition, a parametric study was carried out investigating the effects of the aspect ratio, post-tensioning and the head joints. It was shown that the model was successful in reflecting the global in-plane behaviour of masonry walls. Although the crack pattern predicted by the model was not in exact agreement with the test results, its results were consistent with the expected nature of masonry walls subjected to in-plane loading and their known failure modes. Also a good agreement was found for the shear strength observed in the model and tests and predicted by the analytical relations. In a parametric study using the model, it was shown that post-tensioning, a type of retrofitting method, can improve the in-plane behaviour of masonry walls remarkably irrespective of their aspect ratios. However, wall corners should be strengthened in order to preserve wall ductility. It was also showed that horizontal post-tensioning decreases the initial stiffness and yielding shear strength of the masonry walls. Nevertheless, it does not have noticeable effect on the ultimate shear strength of the wall and increases the wall integrity by preventing it from the sliding and shear failure. Higher vertical (axial) post-tensioning may be used to avoid the above reduction in the initial stiffness and yielding shear strength of a horizontally post-tensioned masonry wall. Although the head joints play a crucial role in the local wall behaviour, the parametric study showed that they do not influence remarkably the global behaviour of the wall.

Acknowledgment

The authors would like to thank the Swiss Federal Laboratories for Material research, EMPA as well as the University of Tehran for support of this study. The authors are also grateful to Dr. ElGawady for giving details of his tests.

References

- [1] Mele E., Gatto D., De Luca A.: *Structural analysis of basilica churches: A case study*, Historical Constructions, 2001, pp. 729.

- [2] Valcarcel J.P., Dominguez E., Martin E., Escrig F.: *Structural behaviour of gothic vaults*, International conference on structural studies, repairs and maintenance of heritage architecture, Halkidiki, Greece, 2003.
- [3] Palacio A.G., Hernandez J.D., Aldasoro J.: *Monitoring and structural analysis of the church "Santa Maria de Elexondo (Zeanuri)"*, Historical Constructions, 2001, pp. 463–468.
- [4] Luciano R., Marfia S., Sacco E.: *Reinforcement of masonry arches by FRP materials, experimental tests and numerical investigations*, Proceedings of international conference on composites in infrastructures, San Francisco, California, USA, 10–13 June, 2002.
- [5] Gambarotta L., Lagomarsino S.: *Damage models for the seismic response of brick masonry shear walls. Part I: The mortar joint model and its applications*, J. Earthquake Engineering and Structural Dynamic, 1997, Vol. 26, pp. 423–439.
- [6] Gambarotta L., Lagomarsino S.: *Damage models for the seismic response of brick masonry shear walls. Part II: The continuum model and its applications*, J. Earthquake Engineering and Structural Dynamic, 1997, Vol. 26, pp. 441–462.
- [7] ANSYS. Release 5.4: *ANSYS Manual Set.*, ANSYS Inc., Canonsburg, USA, 1996.
- [8] Malyszko L.: *Failure criteria for masonry as anisotropic material*, Proceedings of IV international conference on analytical models and new concepts in concrete and masonry structures, Cracow, Poland, 5–8 June, 2002, pp. 111–115.
- [9] Ali S., Page A.: *Finite element model for masonry subjected to concentrated loads*, Journal Structural Engineering, ACSE, 1988, 114 (8), pp. 1761–1784.
- [10] Wawrzynek A., Cincio A.: *Adaptation of a plastic-damage concrete model for masonry material subjected to cyclic load*, Proceedings of VIII international conference on computational plasticity, CIMNE, Barcelona, 2005.
- [11] Ganz H. R.: *Mauerwerksscheiben unter normalkraft und schab.*, Bericht Nr. 148, Birkhauser Verlag Basel, Institut für baustatik und konstruktion, ETH Zurich, 1985.
- [12] Kumar P., Bhandari N. M.: *Non-linear finite element analysis of masonry arches for prediction of collapse load*, Structural Engineering International, Vol. 3, 2005, pp. 166–174.
- [13] Litewka A., Szojda L.: *Damage and failure of brittle solids*, Proceedings of XXI international congress of theoretical and applied mechanics, Warsaw, Poland, 2004.
- [14] William K.J., Warkne E.P.: *Constitutive model for the tri-axial behaviour of concrete*, Proceeding of the international association for bridge and structural engineering, 19, ISMES, Bergamo, Italy, 1995.
- [15] Ganz H.R., Thürlimann B.: *Versuche an mauerwerksscheiben mit normalkraft und querkraft (Test of masonry walls under axial and shear forces)*, IBK Bericht Nr. 7502-4, Institut für Baustatik und Konstruktion, ETH Zürich, 1984.
- [16] ElGawady M.: *Seismic in-plane behaviour of URM walls upgraded with composites*, A thesis for the degree of PHD, EPFL, Lausanne, Switzerland, 2004.
- [17] Gabor A., Ferrier E., Jacquelin E., Hamelin P.: *Analysis and modelling of the in-plane shear behaviour of hollow brick masonry panels*, ELSEVEIR, Construction and Building Materials, Vol. 20, 2006, pp. 308–320.
- [18] Tomazevic M.: *Earthquake resistant design of masonry buildings*, Imperial College Press, London, 1999.
- [19] Paulay T., Priestley M.J.N.: *Seismic design of reinforced concrete and masonry buildings*, Wiley, New Jersey, 1992.
- [20] Ganz H.R.: *Post-tensioned masonry structures*, VSL Technical Reports, Series 2, Published by VSL International LTD, Bern, Switzerland, 1990.

-
- [21] Schwegler G.: *Masonry construction strengthened with fibre composites in seismically endangered zones*, Proceedings of 10th European conference on earthquake engineering, Vienna, Austria, 1994, pp. 2299–2303.
- [22] Page A. W., Huizer A.: *Racking tests on reinforced and prestressed hollow clay masonry walls*, Proceedings of 8th International Brick/Block Masonry Conference, Dublin, 1988, pp. 538.

Numeryczne modelowanie płaskiego zagadnienia pracy ścian URM oraz analiza ich nośności z uwzględnieniem wpływu pionowych i poziomych stężeń oraz kotew czołowych

Mur jest złożonym materiałem kompozytowym o nieliniowych właściwościach, które powodują to, że ich analiza numeryczna jest złożonym i trudnym zadaniem. W artykule przedstawiono nieliniowy mikro-model stworzony przy użyciu uniwersalnego kodu elementów skończonych służący symulacji zachowania się niewzmocnionego muru w jego płaszczyźnie. Zbadano zdolność modelu do przewidywania występowania takich zjawisk jak pęknięcie, kruszenie, poślizg, tak jak we wcześniejszych badaniach ortotropowego zachowania się murów. Następnie model użyty został do badań parametrycznych wpływu pionowego i poziomego sprężania oraz wpływu kotew czołowych na nośność murów.



Methodology of estimation of accident situation in building industry

BOŻENA HOŁA

Wrocław University of Technology, Wybrzeże Wyspiańskiego 27, 50-370 Wrocław, Poland

The paper presents the methodology of analyses and estimation of the accident situation in the building industry. The indices, elaborated by the author, which enable to analyse the accident situation in the building industry as a static, homogeneous phenomenon, as a static non-homogeneous phenomenon and as a dynamic phenomenon, are the base for the above methodology. The analysis and estimation of the accident situation in the building industry were done on the grounds of the statistical database, published by the GUS (The Central Statistical Office). The indices values of the accident situation, suggested for the estimation of the accident situation, were calculated and next the mathematical model of the development tendency of the accident situation was elaborated. The model consists of two parts: i.e. the model of the development tendency (which is m -degree polynomial) and the model of the general downward or upward tendency of the analysed phenomena described by the linear function.

Keywords: *building industry, accident situation, methodology of analysis, estimation indices of accident situation*

1. Topicality and importance of a subject matter

The building industry (against a background of the other sections of the national economy) is characterised by the high level of the hazards for workers' life and health and the high level of the accident situation [5, 8 and 12]. The above statement concerns lots of countries in the world. In Poland in the year 2005 every fifth person, who died as a result of an accident at work, was a worker of the building industry [20]. In the Great Britain, the workers employed in the building industry meet with the fatal accidents fifth times often and with the serious accidents twice often than the ordinary persons employed in the other sections of the national economy [5].

According to the data of the Statistical Office of the European Community (EUROSTAT), the building industry is the most dangerous activity from all of the human activities (the agriculture is the next one) [2]. It was noted down 6.502 persons injured in the accidents at work per each 100.000 working persons in the building industry in the European Community countries in the year 2003, whereas in the agriculture it was noted down 5.043 persons injured in the accidents at work per each 100.000 working persons. In the United States, the workers employed in the building industry meet with the fatal accidents over three times often than the persons employed in the other sections of the national economy. Furthermore, in each year every sixth person employed in the building industry is injured as a result of an accident at work. In China in the year 2000, 35.52 million persons were employed in

the building industry. 3.000 persons died as a result of the accidents at work [13]. The above data confirm the thesis that the building industry belongs to these sections of the national economy, which are characterised by the very high level of the occupational risk.

2. Identification of reason-effect relations in numerical description of accident situation

The number of accidents and the number of occupational diseases are the most important indices among the various indices, which have an effect on the work safety estimation. In order to enable the comparison of the level of various phenomena, which occur among the different works of the same line of business or among the different lines of business some proper indices are elaborated [3, 6 and 19]. They enable to estimate the level of the occupational risk in the given line of business as well as to compare the changes of this level in the particular time intervals. The higher values of the indices are the signal of deterioration, so the reasons of the above situation should be sought. Moreover, the increasing values of the indices show that the work safety prevention must be changed, corrected or improved.

In the paper, the accident situation in the building industry was considered at various levels, i.e. as a static, homogeneous phenomenon, as a static non-homogeneous phenomenon and as a dynamic phenomenon. The various accident rate indices and the accident seriousness index were applied for the estimation of the accident situation as a static, homogeneous phenomenon. The standardised accident rate indices were applied for the estimation of the accident situation as a static, non-homogeneous phenomenon. The chain indices of dynamics, the single-base indices of dynamics and the indices of dynamics changes were applied for the estimation of the accident situation as a dynamic phenomenon.

2.1. Accident situation as a homogeneous phenomenon

The homogeneous phenomena are characterised by their quality features, which do not change in the time period [4]. The accident rate index, defined as the number of persons injured in the accidents at work recorded in the investigated time period with reference to the different values characterising the building production, is a base for the estimation of the accident situation as a homogeneous phenomenon.

The accidents can be divided, considering a person's (injured in an accident at work) health loss, into: minor, serious and fatal. The number of persons injured in the particular kind of accidents is a variable quantity in the particular analysed time periods [20]. Also the pace of work contributes significantly to such phenomenon as the accidents at work. In order to obtain the complete picture of changes of the work safety state in the building industry (in the investigated time interval) it was made the following assumption. In the estimation of the accident situation it should be taken

into account (apart from the number of persons injured in the accidents at work and the number of employed persons) also some parameters, which describe the building production value.

Therefore, the analysis of the accident situation was done from the following points of view:

- the values changes of the accident rate index (total, minor, serious and fatal) with reference to the number of persons employed in the building industry,
- the values changes of the accident rate index (total, minor, serious and fatal) with reference to both the number of persons employed in the building industry and to the building production value.

Figure 1 shows the reason-effect assumptions, applied to calculate the analytic form of the total accident rate index (including minor, serious and fatal accidents) with reference to the persons employed in the building industry. Whereas, Figure 2 shows the reason-effect assumptions, applied to calculate the total accident rate indices (including minor, serious, and fatal) with reference to the persons employed in the building industry and the building production value.

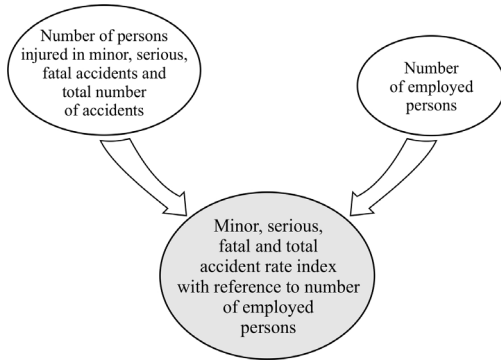


Fig. 1. The reason-effect relations within the accident rate index with reference to the number of employed persons

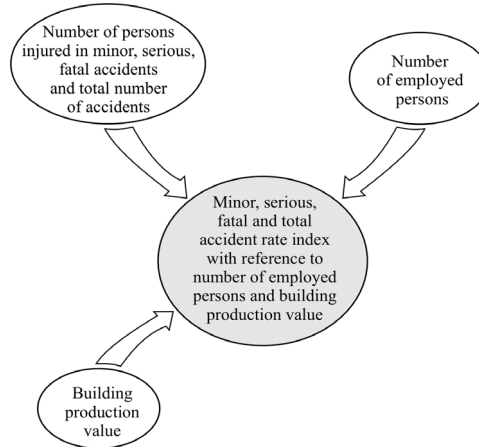


Fig. 2. The reason-effect relations within the accident rate index with reference to the number of employed persons and the building production value

The accident rate index defines the number of persons injured in the accidents at work in the investigated year t_i per each 1000 employed persons. The accident rate index is expressed from the following formula:

$$w_{i,k,1000} = \frac{lp_{i,k}}{lz_i} 1000, \quad \text{with } I = 1, \dots, N, \quad k = 1, \dots, 4, \quad (1)$$

where:

$lp_{i,k}$ – number of persons injured in accidents at work in building industry in year t_i , at:

$k = 1$ – minor accidents,

$k = 2$ – serious accidents,

$k = 3$ – fatal accidents,

$k = 4$ – accidents in total,

lz_i – number of persons employed in building industry in year t_i .

The accident rate index value shows the level of the occupational risk connected with the construction work realisation.

It is well known fact that the pace of work contributes significantly to such phenomena as the accidents at work [16]. Whereas, the production process in the building industry is characterised by the variable values of the obtained national economy indices. Therefore, in the paper, it was applied the index for the estimation of the accident situation, which connects such information as: the number of persons injured in the accidents at work, the number of persons employed as well as the obtained building production value.

The accident rate index with reference to the building production value unit was expressed by the following formula [11]:

$$w_{i,k,1000,p} = \frac{w_{i,k,1000}}{p_i} = \frac{lp_{i,k}}{lz_i p_i}, \quad \text{with } i = 1, \dots, N, \quad k = 1, \dots, 4, \quad (2)$$

where:

p_i – building production value in year t_i .

The above index is a measure of the production biological cost. In order to obtain the comparable values of this index achieved in the particular years of the investigated time period, it was taken into account the prices increase indices in assuming the building production value [1]. The building production value in the year t_i , reduced to the value in the year t_1 , was expressed by the following formula:

$$p_i^r = \frac{P_i}{w_1^{wc} w_2^{wc} \dots w_{i-1}^{wc} w_i^{wc}}, \quad (3)$$

where w_i^{wc} is price increase indices in year i compared with year $i - 1$.

2.2. Accident situation as a non-homogeneous phenomenon

The accident rate indices concern homogeneous phenomena. They inform about the increase or decrease of an individual phenomenon. It concerns for example only the fatal accidents rate, the serious accidents rate or the minor accidents rate or the total number of accidents. However, the accident situation is not a homogeneous phenomenon, because the rate of the particular kinds of accidents and their structure

change in the succeeding years. In this situation, the standardized accident rate, which takes into account all the kinds of accidents and their structure at the same time, is proposed for the estimation of the accident situation.

The following indices are proposed for the estimation of the accident situation as a non-homogeneous phenomenon [9, 10]:

- the standardized accident rate index with reference to the number of employed persons,
- the standardized accident rate index with reference to the number of employed persons and the building production value.

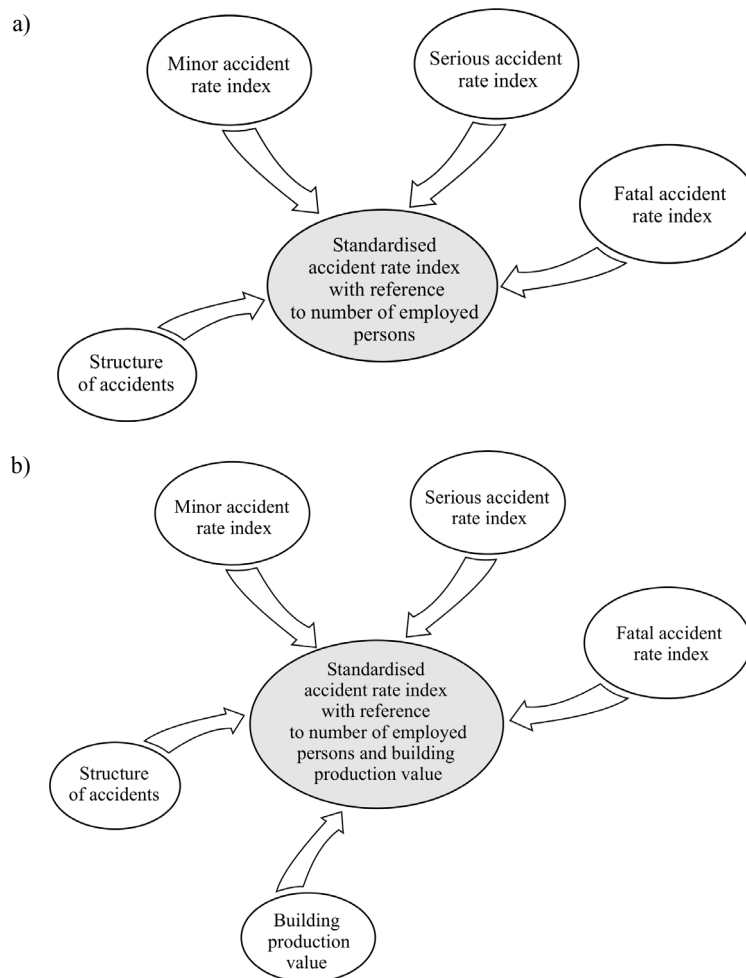


Fig. 3. Reason-effect relations included in elaboration of: a) the standardised accident rate index with reference to the number of employed persons, b) the standardised accident rate index with reference to the number of employed persons and the building production value

Figure 3 shows the reason-effect assumptions applied to calculate the standardised accident rate indices.

The standardised accident rate index with reference to 1,000 persons employed in the building industry was calculated from the following formula:

$$wS_{i,1000} = \frac{\sum_{k=1}^3 \gamma_{i,k} wZ_{i,k,1000}}{\sum_{k=1}^3 \gamma_{i,k}}, \quad \text{with } i = 1, \dots, N, \quad k = 1, 2, 3, \quad (4)$$

where:

$\gamma_{i,k}$ – weight of accident of given group in relation to weight of base accident, which is equal 1,

$wZ_{i,k,1000}$ – rate index of balanced group k .

The standardised accident rate index with reference to 1000 persons employed in the building industry and 1000 million PLN of the building production value was calculated from the following formula:

$$wS_{i,1000,p} = \frac{wS_{i,1000}}{p_i}. \quad (5)$$

The calculation algorithm of the above index value is presented in the papers [9, 10].

2.3. Accident situation as a dynamic phenomenon

The indices, which have been applied to estimate the accident situation till now, have dynamic character. It is very important in the estimation of the accident situation to have a possibility to compare the changes, which occurred in the particular time periods. The effects of the undertaken activities, which aim at the work safety improving, can be seen not before the next time periods. The presented accident rate indices inform, in the static way, about the level of the phenomenon in the particular investigated time periods [9, 15]. However, they do not inform about the pace and intensity of changes, which occur in time [14, 17]. The indices of dynamics are helpful in the investigation of the pace and intensity of these changes. They present the changes, which occur in the investigated phenomenon, in the analysed time period in relation to their level in the previous time period.

The dynamic changes were estimated according to the following indices:

- the chain indices of dynamics of the total, minor, serious and fatal accident rate with reference to the employed persons,
- the chain indices of dynamics of the accident seriousness,

- the single-base indices of dynamics of the total, minor, serious and fatal accident rate with reference to the employed persons,
- the single-base indices of the accident seriousness.

In calculation of the chain indices of dynamics, the values achieved in the previous year were assumed as a base for the comparison. The value of the chain index of dynamics $I > 1$ means that an increase of the analysed phenomenon occurred in the investigated time period in comparison with the value achieved in the previous time period. The value of the chain index of dynamics $I_i \leq 1$ means that a decrease of the analysed phenomenon occurred in the investigated time period in comparison with its level in the previous year or that the phenomenon is still at the same level [14]. The previously calculated values of the particular accident situation indices were used for the estimation of the chain indices of dynamics of the accident rate and the accident seriousness indices. Figure 4 shows the reason-effect assumptions applied for the calculation of the above indices.

The chain indices of dynamics of the accident rate $Iw_{i/i-1,k}$ were calculated from the relation:

$$Iw_{i/i-1,k} = \frac{W_{i,k,1000}}{W_{i-1,k,1000}}, \quad \text{with } i = 1, \dots, N, \quad k = 1, \dots, 4. \quad (6)$$

In calculation of the single-base indices of dynamics, the values achieved in the year 1992 were assumed as a base for the comparison. Figure 5 shows the reason-effect assumptions applied for the calculation of the single-base indices of dynamics of the accident rate and the accidents seriousness indices.

The single-base indices of dynamics of the accidents rate $Iw_{i/bk}$ were calculated from the relation:

$$Iw_{i/bk} = \frac{W_{i,k,1000}}{W_{1,k,1000}}, \quad \text{with } i = 1, \dots, N, \quad k = 1, \dots, 4. \quad (7)$$

In order to examine the changes rate, which occur in the accident rate at work in the building industry in relation to the changes rate, which occur in the building production values, the indices of dynamics changes were created. The following indices of dynamics were applied in the paper:

- the index of dynamics changes of the chain index of dynamics of the total accidents rate (including minor, serious and fatal accidents) in relation to the chain index of dynamics of the building production value.
- the index of dynamics changes of the single-base index of dynamics of the total accidents rate (including minor, serious and fatal accidents) in relation to the single-base index of dynamics of the building production value.

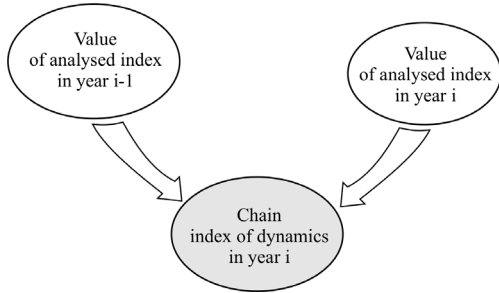


Fig. 4. Numerical relations included in calculation of chain indices of dynamics of accidents rate

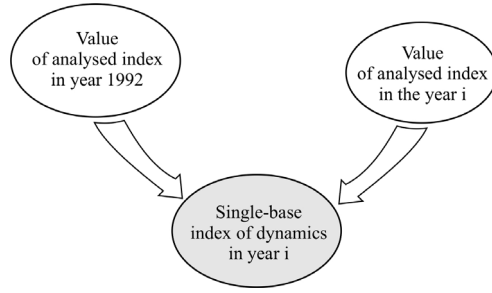


Fig. 5. Numerical relations included in calculation of single-base indices of dynamics of accidents rate

The above indices are calculated according to the following formulas:

$$wz_{i/i-1,k,p} = \frac{Iw_{i/i-1,k}}{Ip_{i/i-1}}, \quad \text{with } i = 1, \dots, N; \quad k = 1, \dots, 4, \quad (8)$$

$$wz_{i/b,k,p} = \frac{Iw_{i/b,k}}{Ip_{i/b}}, \quad \text{with } i = 1, \dots, N; \quad k = 1, \dots, 4, \quad (9)$$

where:

$wz_{i/i-1,k,p}$ – index of changes for chain indices of dynamics,

$wz_{i/b,k,p}$ – index of changes for single-base indices of dynamics.

The chain index of dynamics of the building production value $Ip_{i/i-1}$ is calculated according to the following formula:

$$Ip_{i/i-1} = \frac{p_i}{p_{i-1}}, \quad \text{with } i = 1, \dots, N. \quad (10)$$

The single-base index of dynamics of the building production value $Ip_{i/i-1}$ is calculated according to the following formula:

$$Ip_{i/b} = \frac{p_i}{p_b}, \quad \text{with } i = 1, \dots, N, \quad (11)$$

b – base year (the year 1992 was assumed as the base year).

3. Methodology of research of accident situation

The research covered (in the scope of analysis and estimation of the accident situation) the sets of data, which consist of the data about the accidents recorded in Poland in the particular years. The statistical data were obtained according to the complete examination, i.e. in the research it was taken into account the all recorded accidents at work.

It was elaborated the following own methodology of the research of the accident development tendency in the building industry:

- The research covered the time interval from the year 1992 to the year 2005. The time interval covered 14 yearly time periods $i = 1, \dots, 14$. The investigated time interval was left side bounded to the year 1992. It is because in this year the standard directions concerning the principles of collecting and sending data (about the accident at work) to the Statistical Offices started to be in force. The investigated time interval can be right side unlimited, which means that the research results can be updated as the new data inflow.

- The data concerning the accidents at work (in the scope to do the analysis) and the data concerning the finance results in the building industry were selected form the database for the particular yearly time periods,

- according to the originally elaborated rules and algorithms (enclosed in chapter 5 of the paper) the values of the accidents rate indices, the accident seriousness indices and the indices of dynamics $w_{i,r}$ in the investigated time period t_i for $i = 1992, \dots, 2005$ and $r = 1, \dots, 29$ were calculated,

- the set W of the obtained results was divided into R -subsets, which include the values of single-named indices w_r ($R = 29$),

- for particular single-named indices the time series $(t_i, w_{i,r})$ were created, where $r = 1, \dots, R$,

- on the grounds of the value w_i in time period t_i it was established that the relation course $w_{i,r}(t_i)$ transforms the function:

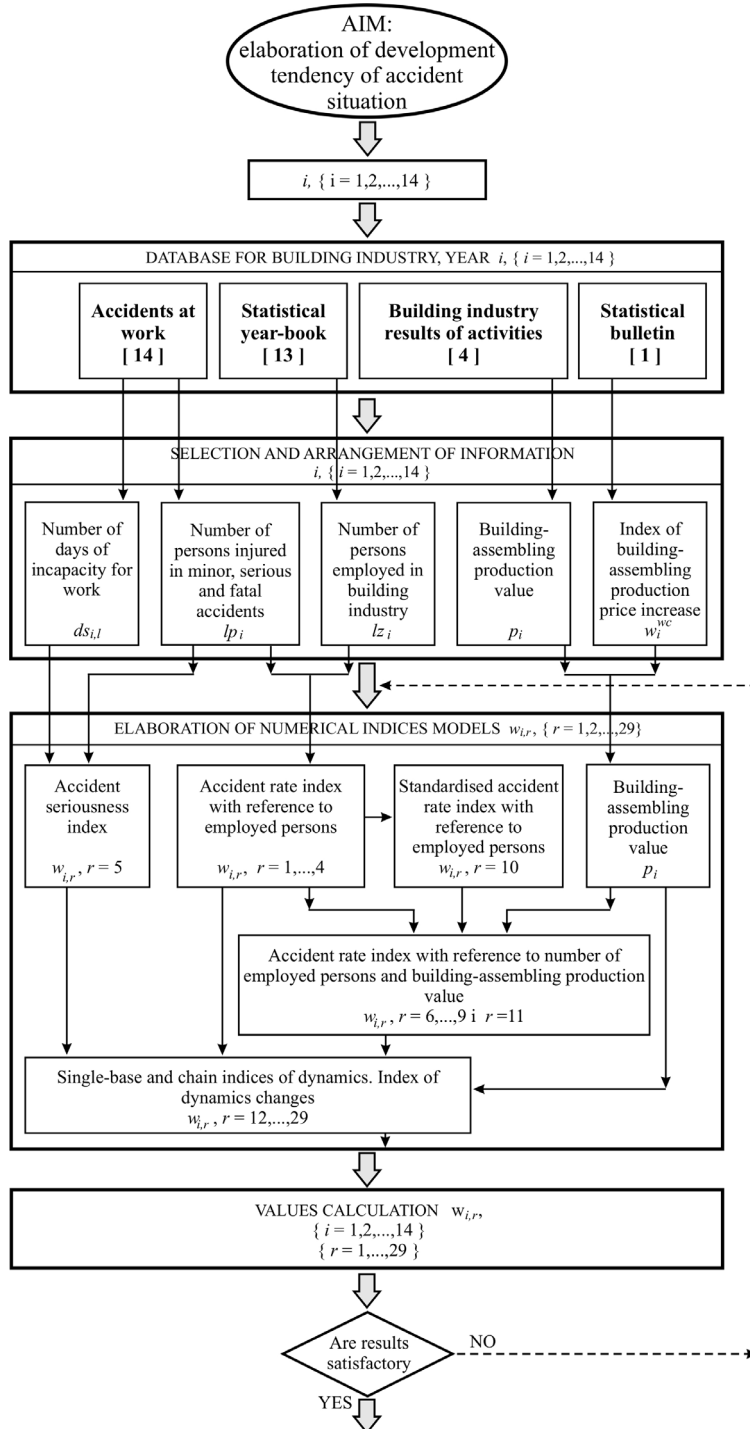
$$f_r(t) = \alpha_{r,0} + \alpha_{r,1}t^1 + \dots + \alpha_{r,m}t^m \quad \alpha_{r,m} \neq 0 \quad (12)$$

- the values $w_{i,r}^*$ were educed according to t_i in the form of the developing function $f_r(t_i)$ about the general meaning for the index w_r ,

- the correlation coefficient and the determination coefficient were applied as an adjustment measure of the applied trend functions to the real values. The polynomial degree were established according to comparison of the remainder variances using the F -Snedecora test of significance,

- for the particular indices the analysis of their values changes and the analysis of the trend function course were done.

The block diagram on Figure 6 presents the elaborated methodology of the development tendency research of the accident situation in the building industry.



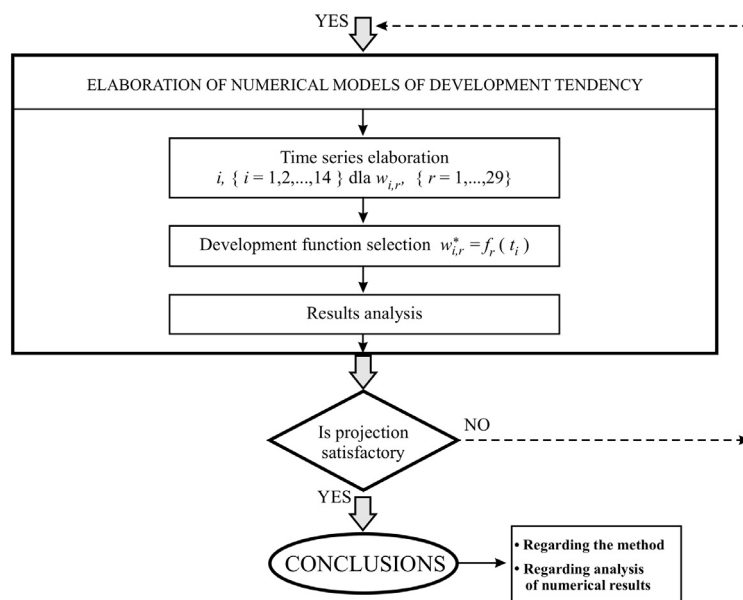


Fig. 6. Methodology of research of accident situation development tendency

The accident situation in the building industry was estimated according to 29 indices in each examined time period t_i , $i = 1, \dots, N$ including the one calendar year. The analysed time interval including the years 1992–2005 is characterised by the data matrix W :

$$W = \begin{bmatrix} w_{1,1} & w_{1,r} & \dots & w_{1,R} \\ w_{2,1} & w_{2,r} & \dots & w_{2,R} \\ \dots & \dots & \dots & \dots \\ w_{i,1} & w_{i,r} & \dots & w_{i,R} \\ w_{N,1} & w_{N,r} & \dots & w_{N,R} \end{bmatrix}. \quad (13)$$

The set W of the accident situation indices were divided into the subsets created by the column vectors W_r , their elements are the values of the single-named indices.

$$W_r = \{w_{i,r} : i = 1, \dots, N\}, \quad r = 1, \dots, 29;$$

$$W = W_1 \cup W_2 \cup \dots \cup W_r \cup \dots \cup W_{29}. \quad (14)$$

The subsets of homogeneous data (obtained in this calculation) were the base for elaboration of the development tendency models of the analysed phenomena.

4. Results of research and analyses

4.1. Analysis of accident situation as a homogeneous phenomenon

It is important in the estimation of the accident situation how often the accidents (classified as: minor, serious and most of all fatal) happen. The fatal accidents, considering their irreversible effects, cause the huge emotional implications in the society. Therefore, it is very important to follow the changes, which occur in the number and level of the fatal accidents. The paper presents the research results and the models of the development tendencies of the selected indices (which present the changes occurring in the number of the fatal accidents).

Figure 7 shows the formation of the number of persons injured in the fatal accidents at work in the building industry. The maximum number of persons (i.e. 177 persons) injured in the fatal accidents was noted down in the year 1997. Whereas, the minimum value (88 persons) was noted down in the year 2003. The increase of the number of persons injured in the fatal accidents during the last two years of the investigated period of time is an alarming phenomenon. In the year 2005, 106 persons suffered death in the accidents on the building sites. It means that for each five person, who suffered death as a result of an accident at work, one was a worker of the building industry section.

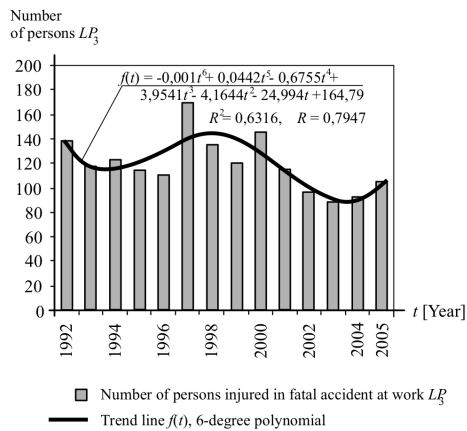


Fig. 7. The variation course in time of the number of persons injured in the fatal accidents at work in the building industry

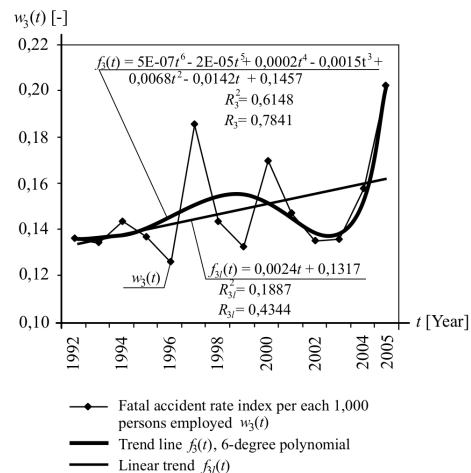


Fig. 8. The variation course in time of the fatal accident rate index with reference to 1000 persons employed in the building industry

Figure 8 shows the variation course of the accident rate index values of the fatal accidents per each 1000 persons employed in the building industry. The above index shows a very large variation in the investigated time interval. The considerable

increase of this index value during the last two years of the investigated time period is a very alarming fact. In the year 2005, the index reached the value 0.203 person injured per each 1000 persons employed in the building industry. The index minimum value 0.1266 person injured in the fatal accident at work in the building industry for each 1000 persons employed was noted down in the year 1996. The trend line, described by the linear function $f_3(t)$, indicates a very unfavourable upward tendency.

Figure 9 shows how the building-assembling production value p^* in the years 1992–2005 were formed. Figure 10 shows the variation course of the accident rate index of the fatal accidents per each 1000 persons employed as well as 1000 million PLN of the building production value. The index shows the upward-downward-upward tendency. The index maximum value 0.0080 was noted down in the year 1997. The index minimum value 0.0048 was noted down in the year 1999. The trend line, described by the linear function $f_8(t)$, indicates a favourable downward tendency. However, the increase of this index value (during the last three investigated years) is very alarming.

4.2. Analysis of accident situation as a non-homogeneous phenomenon

Figure 11 shows the variation course of the standardised accident rate index values in the building industry in the years 1992–2005. The above index is characterised by the rather high changeability of the obtained results. However, the trend function has a favourable downward tendency in the all examined period. The index minimum value 1.7642 was noted down in the year 2004.

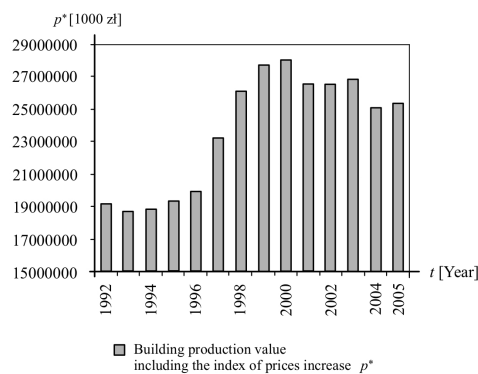


Fig. 9. The variation course in time of the building production value including the index of prices increase

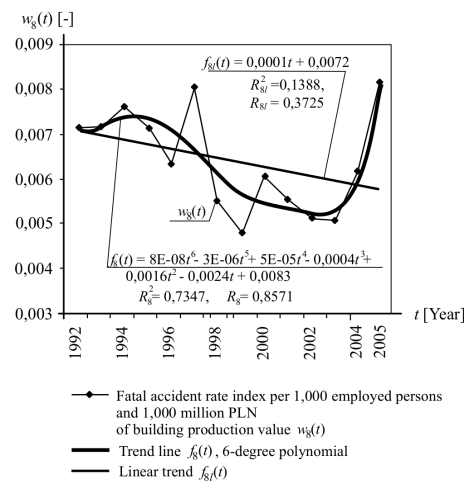


Fig. 10. The variation course in time of the fatal accident rate index values with reference to 1000 employed persons and per 1000 million PLN of the building production value

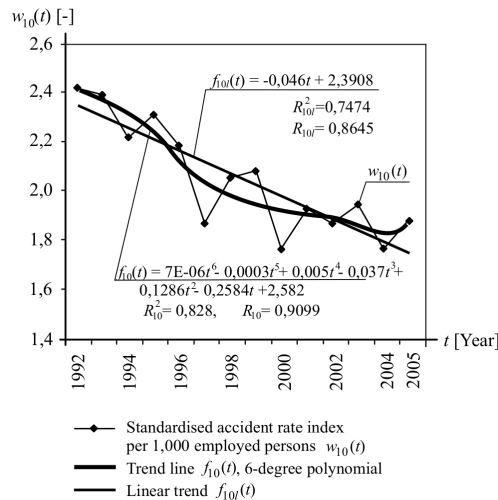


Fig. 11. The variation course in time of the standardised accident rate index values with reference to 1000 employed persons in the building industry

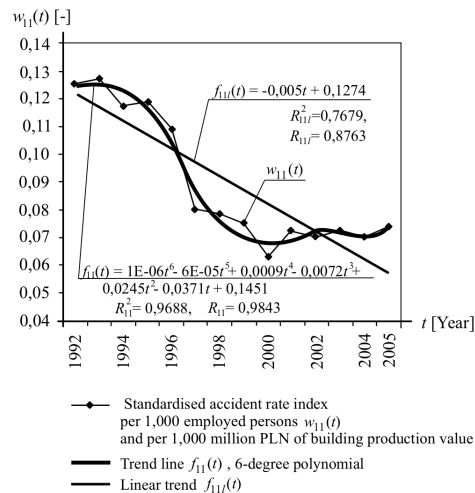


Fig. 12. The variation course in time of the standardised accident rate index values per each 1000 persons employed as well as 1000 million PLN of the building production value

Figure 12 shows the variation course of the standardised accident rate index values per each 1000 persons employed as well as 1000 million PLN of the building production value in the years 1992–2005. From 1992 to 2000 the index decidedly shows the downward tendency and next a very slight upward tendency. The index minimum value 0.0192 was noted down in the year 2000.

4.3. Analysis of accident situation as a dynamic phenomenon

The graphs of the function presented on the Figure 13 show the development dynamics of the chain index of the fatal accidents rate. The phenomenon is characterised by the very high changes in the years 1996–2001. In these years the decreases and increases dynamics of the fatal accident rate was the highest one. Since 2001 it can be noticed the permanent increase of the chain indices of dynamics of the fatal accident rate. The trend, described by the linear function $f_{14}(t)$, shows that the phenomenon has an unfavourable upward tendency. In the analysed time period, the chain index of dynamics of the fatal accident rate reached the maximum value 1.4752 in the year 1997. It means that in the examined year the fatal accident rate dynamics increased by 47.9% relative to the preceding year. However in 1998 the index reached 0.7699, which means that in that year the fatal accident rate decreased by 23.01% relative to the preceding year.

The graphs of the function presented on the Figure 14 show the index of dynamics changes of the fatal accident rate in relation to the building production value expressed by the chain indices. The increasing trend line means that the increase pace of the accidents rate is higher than the increase pace of the building production value.

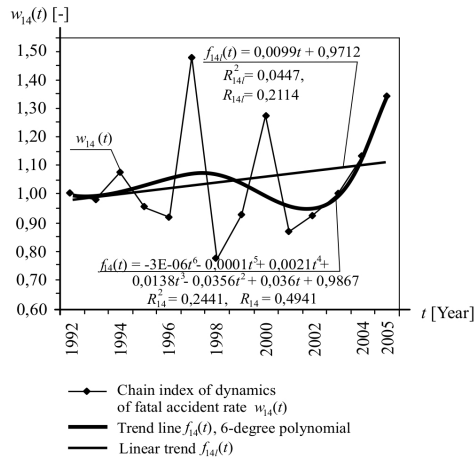


Fig. 13. The variation course in time of the chain index of dynamics of the fatal accidents at work in the building industry

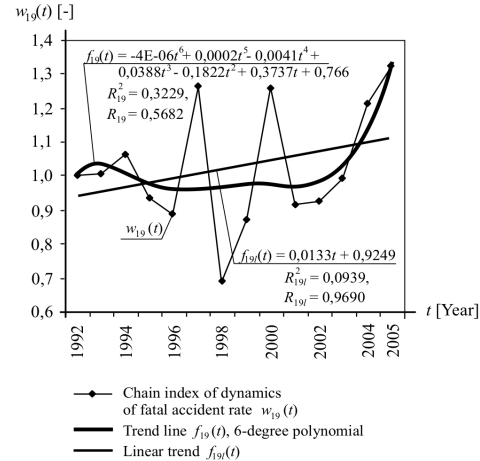


Fig. 14. The variation course in time of the chain index of dynamics of the fatal accidents rate in relation to the chain index of dynamics of the building production value in the building industry

5. Conclusions

The accident situation is a phenomenon, which changes in time period. It means that the indices values, calculated according to the statistical data (including the specified time period), change in relation to the other examined time period. In order to enable the level and direction comparison of the accident situation changes in the building industry the author elaborated the own methodology of its research. The accident situation indices, elaborated by the author, which enable to analyse a phenomenon as a static, homogeneous phenomenon, as a static non-homogeneous phenomenon and as a dynamic phenomenon, are the base for the above methodology.

The accident rate of the particular kinds of accidents belongs to the group of homogeneous phenomena. The following conclusion can be drawn from the analysis of the accident situation as a static homogeneous phenomenon. The accident rate index of the fatal accidents with reference to the number of employed persons and the fatal accident rate index with reference to the number of employed persons as well as the building production value show a decidedly upward tendency in the investigated time interval and a very sharp increase in the last three years of the investigated interval.

The accident situation, in the general meaning, is not a homogeneous phenomenon. In the investigated time intervals, there are three kinds of accidents at the same time, i.e. minor, serious and fatal accidents. Furthermore, the structure of particular kinds of accidents changes in the succeeding time intervals. In order to correctly estimate the changes in the level of the accident situation and the directions

of these changes, it is necessary to use (for their estimation) the index, which combines three kinds of accidents and the index of their structure. The standardised index, presented in the paper, can be applied as such index. It presents, in the form of one number, the accident situation (non-homogeneous in its structure and kinds) as a homogeneous phenomenon.

The standardised accident rate index with reference to the number of employed persons in the building industry shows the decidedly downward tendency in the investigated time interval. Because the minor accidents have a considerable share in the total number of accidents. The standardised accident rate index with reference to the number of employed persons as well as the building production value shows the decidedly downward tendency in the time interval 1992–2000. However, the index stabilises itself in the time interval 2000–2005.

The model of development dynamics of the analysed phenomena (which takes into account the chain and the single-base indices of dynamics) can be useful for the estimation of the dynamics of changes, which occur in the accident situation in the building industry. The above indices show how much the value of the indices describing the phenomenon increased with relation to the previous period, i.e. the base year.

The analysis of the chain indices of dynamics enables to notice the sudden both the positive and the negative changes in the accident situation developing in building industry, which occurred in investigated period of time comparing to the previous period.

In case of the chain indices of dynamics of the fatal accident rate, the trend lines described by the linear function show a very unfavourable general upward tendency. The sudden transitions of the index value are the signal that it should be done the comparative analysis of the obtained indices values and the reasons, which were stated during the accidents.

The index of changes of the chain index of dynamics of the fatal accidents rate in relation to the chain index of dynamics of the building production value enable to state if the dynamics of the combined phenomena in the one-year time periods have a downward character or an upward character. In the analysed time interval they are characterised by the very high changeability. The linear function shows an unfavourable upward tendency. In the whole investigated time period, the average increase of the fatal accident rate at work in the building industry recorded in the one calendar year period is higher than the average year increase of the building production value. The observation of the changes of these indices values should be one of the elements of the work safety management in the building firm.

References

- [1] *Statistical Bulletin, The Central Statistical Office (GUS)* (in Polish), Warsaw, 1993–2006.
- [2] Bojanowski R.: *New Statistical Card of Accident at Work* (in Polish), *Bezpieczeństwo Pracy*, Vol. 7–8, 2005.

- [3] Borys T.: *Indices of Eco-Development* (in Polish), Wydawnictwo Ekonomia i Środowisko, Białystok, 1999.
- [4] Borys T.: *Elements of Quality Theory* (in Polish), Państwowe Wydawnictwa Naukowe, Warsaw, 1980.
- [5] Carter G., Smith S. D.: *Safety Hazard Identification on Construction Projects*, Journal of Construction Engineering and Management. ASCE, February, 2006, pp. 197–205.
- [6] Dohn K.: *Study of Estimation of Production Process in Industrial Firm* (in Polish), Wydawnictwo Politechniki Śląskiej, Gliwice, 2006.
- [7] *Activity of Non-Financial Firms in Year 2003. The Central Statistical Office (GUS)* (in Polish), Information and Statistical Elaboration, Warsaw, 2003–2004.
- [8] Hinze J., Huang X., Terry L.: *The Nature of Struck-by Accidents*, Journal of Construction Engineering and Management. ASCE, February, 2005, pp. 262–268.
- [9] Hoła B.: *Development Tendency for Accident Situation in Building Construction*, Archives of Civil and Mechanical Engineering, Vol. VI, 2006, No. 3, pp. 81–92.
- [10] Hoła B.: *Model of Development Tendency of Accident Situation in Construction Industry*, Archives of Civil Engineering LII, 1, 2006, pp. 177–188.
- [11] Hoła B.: *General Model of Accident Rate Growth in the Construction Industry*, Journal of Civil Engineering and Management, Vol. 13, 2007, No. 4, pp. 255–263.
- [12] Kapliński O.: *Accident Situation in Building Industry in Hong Kong* (in Polish), Przegląd Budowlany, Vol. 2, 2003, pp. 47–49.
- [13] Hunag X., Hinze J.: *Analysis of Construction Worker Fall Accidents*, Journal of Construction Engineering and Management, ASCE, May/June, 2003, pp. 262–271.
- [14] Kassyk-Rokicka H.: *Statistics is not Difficult* (in Polish), Państwowe Wydawnictwo Ekonomiczne, Warsaw, 1986.
- [15] Koradecka D.: *Work Safety and Ergonomics* (in Polish), joint publication, CIOP, Warsaw, 1999.
- [16] Kowalski J.: *Analysis of Trends in Accidents at Work, Occupational Diseases and Hazards in Work Environment during Economic Transformations* (in Polish), Bezpieczeństwo i Higiena Pracy, 12, 2001.
- [17] Ostasiewicz S., Rusnak Z., Siedlecka U.: *Statistics. Elements of Theory and Objective* (in Polish), Academy of Economics Publishers, Wrocław, 2001.
- [18] *Statistical Year Books, The Central Statistical Office (GUS)* (in Polish), Warsaw, 1993–2006.
- [19] Twaróg J.: *Logistic Measures and Indices* (in Polish), Instytut Logistyki i Magazynowania, Poznań, 2003.
- [20] *Accidents at Work in years 1992–2005. The Central Statistical Office (GUS)* (in Polish), Warsaw, 1993–2005.

Metodyka oceny wypadkowości w budownictwie

W pracy przedstawiono metodykę analizy i oceny wypadkowości w budownictwie. Podstawą przyjętej metodyki są opracowane wskaźniki własne pozwalające analizować wypadkowość w budownictwie jako zjawisko statyczne jednorodne, statyczne niejednorodne oraz jako zjawisko dynamiczne. Na bazie danych statystycznych publikowanych przez Główny Urząd Statystyczny przeprowadzono analizę i dokonano oceny wypadkowości w budownictwie. Obliczono wartości

zaproponowanych do oceny wypadkowości wskaźników wypadkowości, a następnie skonstruowano model matematyczny tendencji rozwojowej wypadkowości. Składa się on z dwóch części, a mianowicie: z modelu tendencji rozwojowej, którym jest wielomian m -tego stopnia oraz z modelu ogólnej tendencji wzrostowej lub spadkowej analizowanych zjawisk przedstawionego za pomocą funkcji liniowej.



Research on usability of sulphur polymer composite for corrosion protection of reinforcing steel in concrete

J. HOŁA, M. KSIĄŻEK

Wrocław University of Technology, pl. Grunwaldzki 11, 50-377 Wrocław, Poland

This paper presents the results of the experimental research and analyses indicating the usefulness of polymer sulphur composites to the protection against corrosion of reinforcement. Presented in paper materials, being also the domain of the personal investigations and the methodology are definite. After analyze of the initial results the optimum compositions have been chosen for the experimental research.

Keywords: *corrosion, reinforcing steel, tensile stress, polymeric sulphuric coating, polarization*

1. Introduction

The degradation of reinforced concrete may be caused by the corrosion of the reinforcing steel or the concrete or by the simultaneous corrosion of the reinforcing steel and the concrete [2–5]. The considerable porosity of concrete and cracks in or damage to the concrete cover contribute to the diffusion, absorption and adsorption of gases and to the diffusion of the substances dissolved in the pore liquid deep into the concrete. All kinds of aggressive substances from the surrounding environment diffuse into the concrete and directly or indirectly cause the corrosion of the reinforcing steel, which usually ends in the loss of adhesion of the concrete to the steel, manifesting itself in the fracturing, loosening and spalling of the concrete cover [1, 5, 7–9, 13, 17, 23].

Surface protection of the reinforcing steel, in the form of a hermetic protective coating, considerably reduces or prevents the access of the surrounding gas or water environment to the reinforcing steel [18]. Various materials, e.g. polymer epoxy resins [2, 3–5, 7, 19], inhibiting agents (inhibitors) [5, 13, 17, 21, 22], noble metal admixtures [5, 17], or cathodic protection [5, 10–12, 17, 23–25] are used for this purpose.

It seems that such protection can be provided by coating rebars with a polymer sulphur composite composed of a sulphuric binder, fillers and proper additives. Even though sulphur binders show: resistance to many aggressive water solutions, low absorbability, surface hydrophobicity and quite high (tangent and normal) adhesion to the surface of many materials (including metallic surfaces), they have not been used for this purpose before [6, 13–16, 20].

In order to demonstrate the suitability of sulphur polymer composites for the surface protection of concrete steel experimental research was carried out in the

Institute of Building Engineering at Wrocław University of Technology. The research included: the experimental determination of sulphur polymer composite composition and manufacturing conditions, tests of the composite's selected physical, chemical and mechanical properties, tests of its tangent and normal adhesion to plain and ribbed reinforcing bars and to standard cement mortar and concrete, the determination of the mass decrement resulting from storage in aqueous solutions of acids, hydroxides and salts and in water and the polarization investigation of rebars subjected to tension in a solution modelling the pore liquid in carbonated concrete contaminated with chlorine ions [14].

2. Description of investigations

Sulphur polymer composites were investigated in two stages. In the first stage, compositions were fixed and thirty tests sulphur polymer composites were prepared and pretested. When fixing the compositions, the binder (S_8) content was changed in a range of 55–65%. Mineral powder, silica dust from a drying plant, high-silica sand and plain sand and cement were used as the filler. Carbon black and anthracene oil were used as the additive. The pretesting included preparing composites and determining their basic physical and mechanical properties, such as: bulk density, absorbability by wt., bending strength and splitting tensile strength. The experimental results are reported in detail in [14].

The results of the preliminary tests were analyzed and the sulphur polymer composite having the best properties among the tested composites was selected for further studies. The composition of the composite is given in Table 1 and its experimentally determined properties are shown in Table 2.

Table 1. Composition of selected sulphur polymer composite [14]

Content in [%] of total composite mass		
Binder	Filler	Additive
Sulphur S_8	Mineral quartz dust	Carbon black
[%]	[%]	[%]
63	33	4

Table 2. Experimentally determined properties of sulphur polymer composites [14]

Average bulk density ρ_{pm} [g/cm ³]	Average absorbability by wt. n_{wm} [%]	Average bending strength f_{dm} [MPa]	Average splitting tensile strength $f_{ct,sp}$ [MPa]	Average compressive strength f_{cmc} [MPa]	Coefficient of fragility k [-]	Coefficient of direct elasticity under bending E_{dm} [MPa]	Coefficient of direct elasticity under compression E_{cm} [MPa]
2.10	0.05	$\frac{11.9}{4.9\%}$	$\frac{3.4}{6.1\%}$	$\frac{51.2}{6.2\%}$	0.93	64840	66969

Note: the percentages under the line are coefficients of variation.

The adhesion of a 0.2–4.0 mm thick sulphur polymer composite layer to plain St3S reinforcing steel samples and ribbed 34GS steel samples, 10 mm in diameter and 160 mm long, was tested.

The adjacent adhesion of a 1.5 mm thick sulphur polymer composite layer to rebars under tension and bending and to rebars being pushed out of this composite was tested on plain steel St3S samples and ribbed steel 34GS samples, 10 mm and 20 mm in diameter and 160 mm long.

Also the adjacent adhesion of concrete to reinforcing bars coated with a 1.5 mm thick layer of the sulphur polymer composite was tested on plain reinforcing steel St3S and ribbed steel 34GS samples, 10 mm and 20 mm in diameter and 160 mm long.

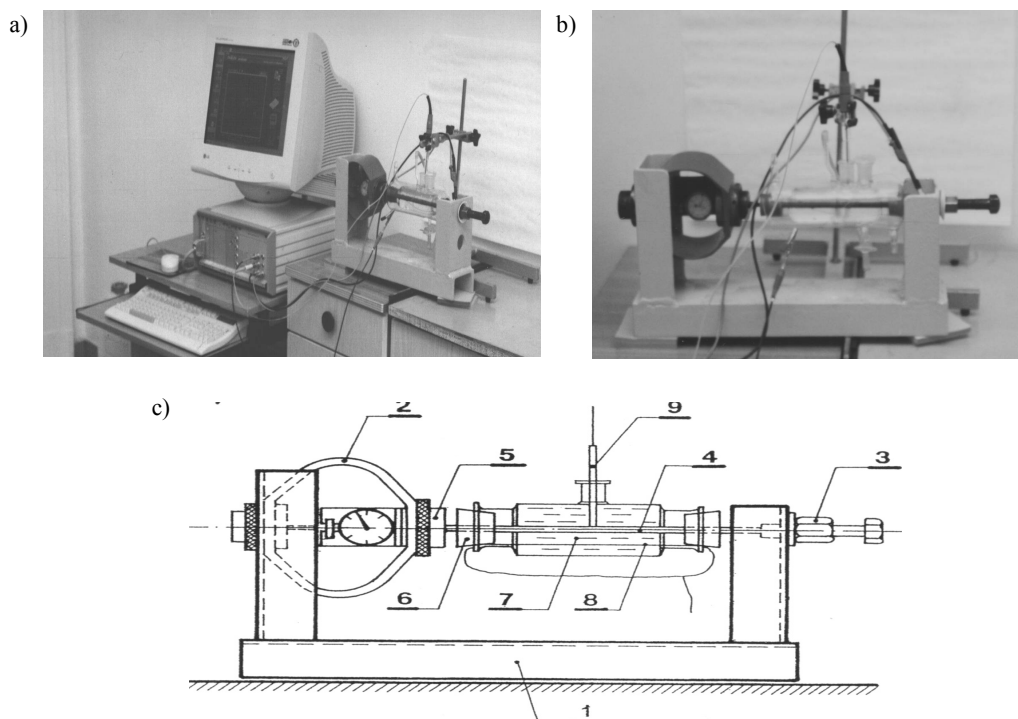


Fig. 1. Device for polarization testing of tensioned rebars: a), b) view of rig, c) schematic of rig (side view), 1 – metal frame, 2 – mechanical dynamometer, 3 – clamping screw, 4 – sample of rebar coated with composite, 5 – dynamometer connector, 6 – rubber stopper, 7 – glass container filled with model pore liquid solution, 8 – platinum wire, 9 – calomel electrode

The decrement in the mass of rebars coated with the composite and stored in aqueous solutions of acids and salts and in water for 1 year was determined using plain St3S steel samples, 10 mm and 20 mm in diameter and 160 mm long.

Polarization investigations of tensioned rebars coated with the sulphur polymer composite were carried out on plain St3S reinforcing steel samples immersed in

a solution modelling the porous liquid in carbonated concrete contaminated with chloride ions. The samples were 10 mm in diameter and 290 mm long. A general view of the polarization test device is shown in Figure 1: a, b, c [10–11, 13–15, 23–25].

3. Test results and their analysis

3.1. Adhesion of sulphur polymer composite layer to rebars under tension and bending

Figure 2 shows at what average values of stress σ_{pm} tensioning plain and ribbed rebars 10 mm in diameter a 0.2–4.0 mm thick layer of the tested sulphur polymer composite gets unstuck from the surface of the rebars. According to this figure, regardless of the polymer layer thickness, this stress is higher for the ribbed reinforcing bars. In this case, the maximum stress σ_{pm} (amounting to 560 MPa) occurs when the thickness of the polymer layer is in a range of 1.3–1.6 mm. Whereas in the case of the plain rebars stress σ_{pm} is less dependent on the polymer composite layer, although at a thickness of 0.5–0.6 mm this stress is higher, amounting to 320 MPa.

Figure 3 shows at what average bending stress σ_{dm} in plain and ribbed rebars 10 mm in diameter a 0.2–3.0 mm thick layer of the tested sulphur polymer composite separates from the surface of the rebars. Also here this stress is higher in the ribbed rebars. According to Figure 3, stress σ_{dm} is the highest when the polymer composite layer is 0.2 mm thick. Also as the thickness of the layer increases, the bending moment at which the layer gets unstuck generally decreases. But at the layer thickness of about 1.4–1.6 mm the downward trend of stress σ_{dm} clearly slows down, reaching a distinct local minimum. For example, in the ribbed rebars coated with the composite this stress amounts to 48.4 MPa.

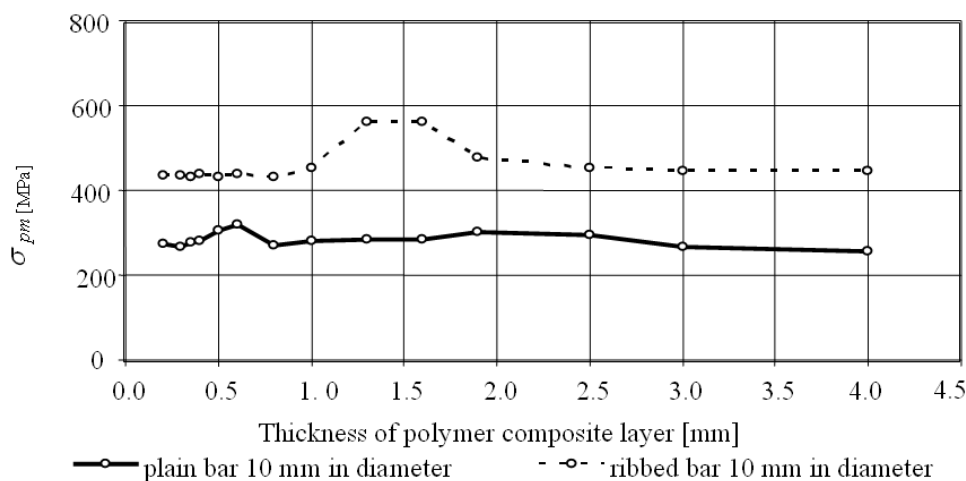


Fig. 2. Average values of stress tensioning rebars 10 mm in diameter, at which sulphur polymer composite layer of different thickness gets unstuck

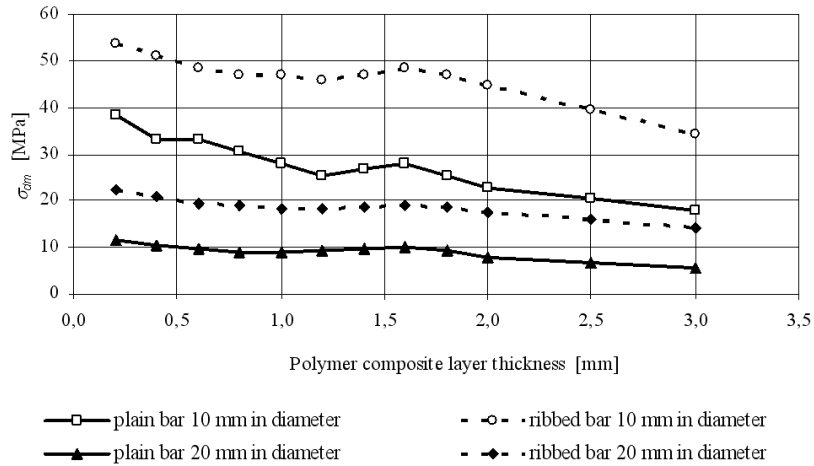


Fig. 3. Average values of stress bending rebars 10 mm and 20 mm in diameter, at which sulphur polymer composite layer of different thickness gets unstuck

The tests have shown that the separation of a 0.2–4.0 mm thick layer of the sulphur polymer composite from the surface of tensioned and bent ribbed rebars always occurs at higher values of stress than in the case of plain rebars of the same diameters. The optimum thickness of the layer for ribbed reinforcing bars is 1.5 mm. In the case of bent plane and ribbed reinforcing bars, the optimum thickness of the layer is 0.2 mm, though it seems that it can be as well 1.5 mm.

3.2. Adjacent adhesion of sulphur polymer composite layer to reinforcing bars

The averages values of tangent adhesion τ_{vm} of a 1.5 mm thick sulphur polymer composite layer to plain and ribbed rebars 10 mm and 20 mm in diameter are shown in respectively Figure 4.

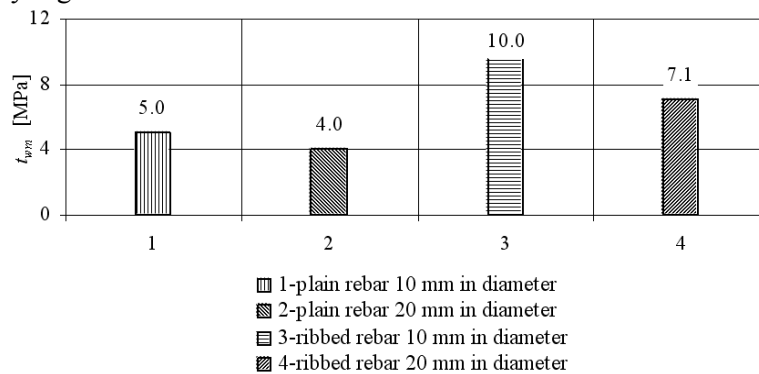


Fig. 4. Average values of adjacent adhesion of 1.5 mm thick sulphur polymer composite to plain and ribbed rebars 10 mm in diameter and 20 mm in diameter

According to the test results, the adjacent adhesion of a 1.5 mm thick sulphur polymer composite layer to the ribbed rebars is twice higher than that to the plain rebars of the same diameter. It is also higher than in the case of the smaller diameter rebars, regardless of whether they are plain or ribbed.

3.3. Adjacent adhesion of sulphur polymer composite to rebars in pushed-out test

The average values of adjacent adhesion τ_{vm} of the sulphur polymer composite to plain and ribbed rebars 10 mm in diameter in the push-out test and the same results for rebars 20 mm in diameter are shown in respectively Figure 5.

According to the test results, the average values of adjacent adhesion of the composite to the ribbed rebars are much higher than those for the plain rebars. They are also higher for the smaller diameter (10 mm) rebars as compared to the 20 mm diameter rebars, regardless of whether they are plain or ribbed.

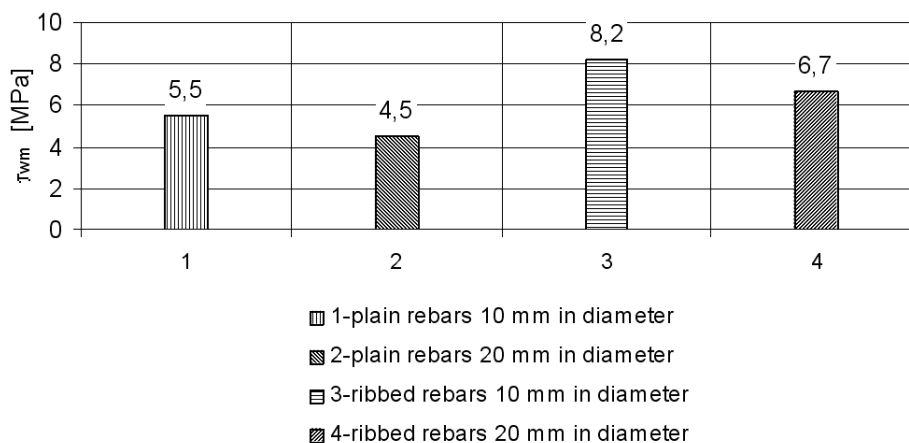


Fig. 5. Average values of tangent adhesion of sulphur polymer composite to plain and ribbed rebars 10 mm in diameter and 20 mm in diameter, being pushed out of composite

3.4. Adjacent adhesion of concrete to rebars coated with sulphur polymer composite

The test results for adjacent adhesion τ_{vm} of ordinary concrete to plain rebars 10 mm in diameter, coated with a 1.5 mm thick layer and to plain rebars 20 mm in diameter are shown in respectively Figure 6. The results denoted by the digits 1–3 are for ordinary concrete made using respectively rounded aggregate, crushed basalt aggregate and crushed granite aggregate. The average values of this adjacent adhesion to rebars 10 mm in diameter and 20 mm in diameter, coated with a 1.5 mm thick layer of the sulphur polymer composite are shown in Figure 7.

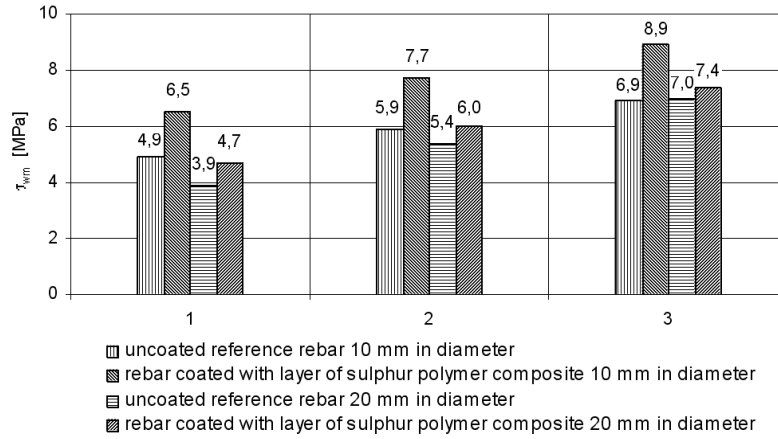


Fig. 6. Average values of adjacent adhesion of ordinary concrete to plain rebars 10 mm in diameter and 20 mm in diameter, coated with 1.5 mm thick layer of sulphur polymer composite, 1 – concrete made using rounded aggregate, 2 – concrete made using crushed basalt aggregate and 3 – concrete made using crushed granite aggregate

For the comparison purposes, Figures 6 and 7 show the adjacent adhesion (τ_{wm}) of ordinary concrete, made using respectively rounded aggregate, crushed basalt aggregate and crushed granite aggregate, to uncoated rebars.

It follows from the results shown in Figures 6 and 7 that in comparison with the uncoated reference rebars, higher values of adjacent adhesion to both plain and ribbed rebars 10 mm and 20 mm in diameter are obtained when the rebars are coated with a layer of the sulphur polymer composite. Then the adhesion values are in a range of 4.7–15.6 MPa depending on the kind of aggregate used, the rebar diameter and the grade of the rebar steel.

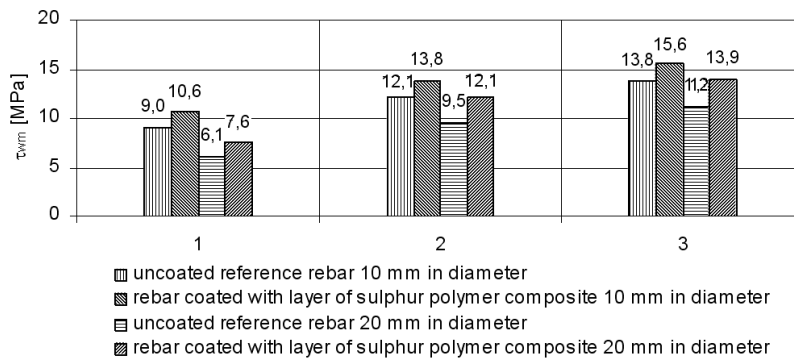


Fig. 7. Average values of adjacent adhesion of ordinary concrete to ribbed rebars 10 mm in diameter and 20 mm in diameter, coated with 1.5 mm thick layer of sulphur composite, 1 – concrete made using rounded aggregate, 2 – concrete made using crushed basalt aggregate, 3 – concrete made using crushed granite aggregate

Therefore it can be concluded that a 1.5 mm thick layer of sulphur polymer composite applied to plain and ribbed rebars of different diameters does not reduce their adjacent adhesion to concrete.

3.5. Mass loss of plain rebars in aqueous solutions of acids, hydroxides and salts and in water

Figure 8 shows the average mass loss (in %) for plain rebars 10 mm in diameter, coated with a 0.6 mm and 1.5 mm thick layer of sulphur polymer composite, immersed in acid aqueous solutions for 1 year. According to the figure, the average mass loss for plain rebars coated with the composite and stored in 5% solutions of H_2SO_4 and HCl and in a 10% solution of CH_3COOH is small – below 0.9%. Whereas in a 5% solution of HNO_3 the average mass loss for the rebars is larger, amounting to respectively 3.5 and 3.9%, depending on the protective layer thickness.

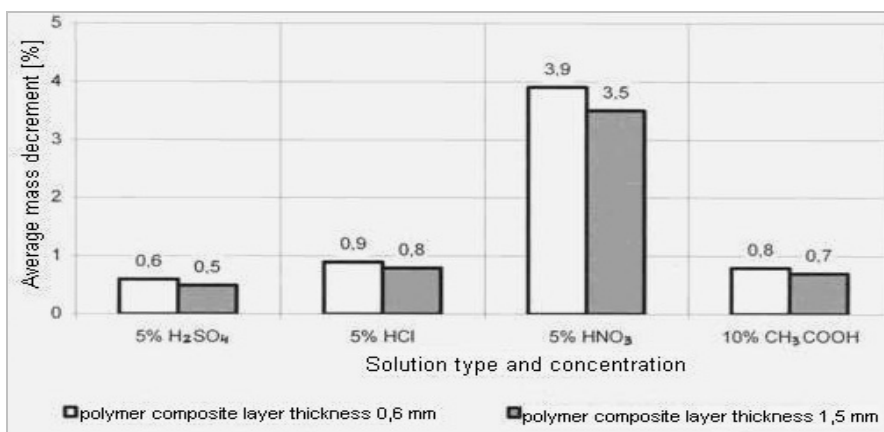


Fig. 8. Average mass loss (in %) for plain rebars 10 mm in diameter, coated with layer of sulphur polymer composite, stored in aqueous solutions of acids for 1 year

One should note that the loss in the mass of the rebars coated with the tested composite only to a small degree depend on the thickness of the coating.

Figure 9 shows the mass loss for rebars 10 mm in diameter, stored in aqueous solutions of hydroxides and in water. According to the figure, the average mass loss for the rebars, coated with a 0.6 mm and 1.5 mm thick layer of the sulphur polymer composite, stored in a saturated solution of $\text{Ca}(\text{OH})_2$ and in H_2O , is negligible, being in a range of 0.1–0.4%. Whereas in both a 5% solution of NaOH and a 5% solution of KOH this loss is very large, amounting to respectively 47.8% and 30.0%.

The average mass loss for rebars 10 mm in diameter, coated with the composite and stored in aqueous solutions of salts are shown in Figure 10. According to the figure, the average mass loss for the rebars stored in: a 10% solution of NaCl , a 10%

solution of $(\text{NH}_4)_2\text{SO}_4$, a 10% solution of CaCl_2 , a 10% solution of K_2CO_3 and a 10% solution of CaCO_3 is slight, being in a range of 0.1–0.7%.

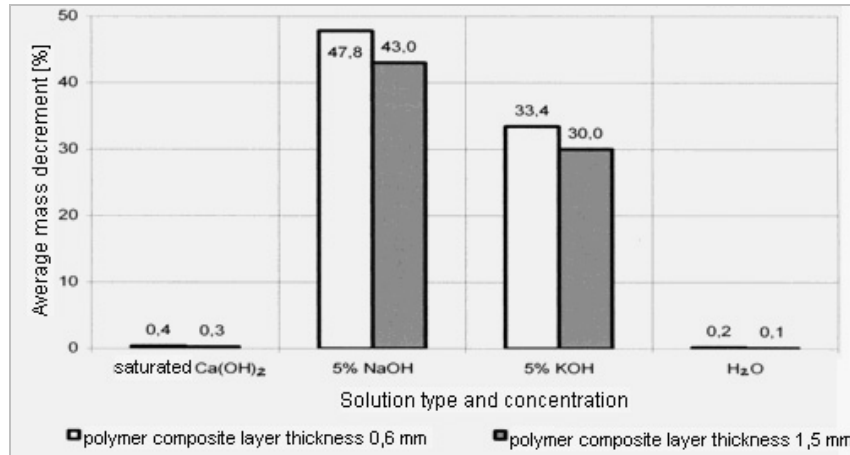


Fig. 9. Average mass loss [%] for plain rebars 10 mm in diameter, coated with layer of sulphur polymer composite, stored in aqueous solutions of hydroxides and in water for 1 year

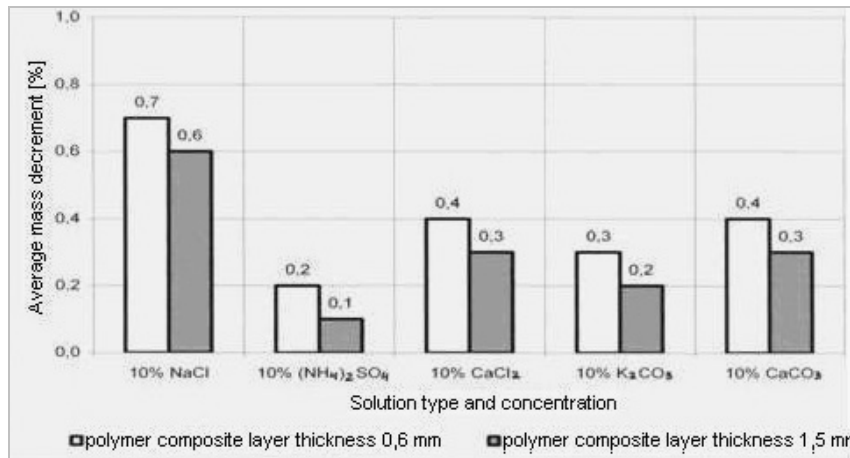


Fig. 10. Average mass loss for plain rebars 10 mm in diameter, coated with layer of sulphur polymer composite, stored in aqueous solutions of salts for 1 year

The investigations have shown that after storage in aqueous solutions of acids, hydroxides and salts and in water the loss in the mass of plain reinforcing bars coated with a layer of the sulphur polymer composite depends mainly on the type of the environment and to a lesser degree on the thickness of the coating. For example, for the 1.5 mm thick sulphur polymer composite layer the largest loss in the mass of the

rebars was recorded in a 5% solution of HNO_3 – 3.9% and in 5% solutions of hydroxides KOH and NaOH – 30% and 43%, respectively. The smallest loss in the mass of the rebars, i.e. 0.1%, was recorded in water.

Similar results as for the 10 mm diameter rebars were obtained for the 20 mm diameter rebars [14].

3.6. Polarization investigations of tensioned rebars coated with sulphur polymer composite

Figure 11 shows corrosion rate H_t versus time (in a time interval of 3–168 hours) at a constant rebar tensile stress σ_a of 194.5 MPa. The rebars are plain rebars 10 mm in diameter, coated with a 0.5 mm and 1.5 mm thick layer of the sulphur polymer composite, immersed in a solution modelling the pore liquid in carbonated concrete contaminated with chloride ions.

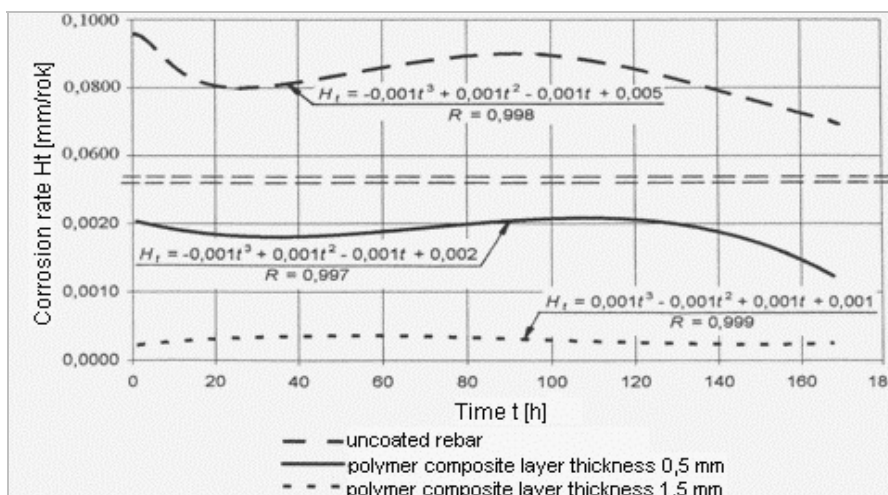


Fig. 11. Corrosion rate versus time at constant tensile stress $\sigma_a = 194.5$ MPa for plain rebars 10 mm in diameter, coated with sulphur polymer composite and for uncoated rebars

According to the figure, after a tensile stress (σ_a) of 194.5 MPa is reached, the corrosion rate (H_t) changes in a time interval of 3–168 hours as follows: it increases initially and after 90 hours from the beginning of the test it starts decreasing, amounting to about 0.0010 mm/year after 168 hours. It is lower in the case of the rebars coated with a 1.5 mm thick layer of the sulphur polymer composite. At this layer thickness, the corrosion rate is only very slightly dependent on time and on the increasing tensile stress in the rebars. Within the test time interval it remained at an almost constant level of 0.000186–0.000242 mm/year. As the figure shows, the corrosion rate for the uncoated rebars is by three orders of magnitude higher. The corrosion rate over time is described by the equations given in Figure 11.

The very low, nearly constant corrosion rate in the case of the rebars coated with a 1.5 mm thick layer of the sulphur polymer composite is beneficial. Therefore such a layer can be considered as contributing to the protection of the reinforcing steel against corrosion in the solution modelling the porous liquid in carbonated concrete contaminated with chloride ions.

Figure 12 shows the dependence between stationary potential E_o , time and tensile strength for the tested rebars coated with a 0.5 mm and 1.5 mm thick layer of the sulphur polymer composite. For comparison purposes, stationary potential E_o in similar uncoated rebars is shown. The dependencies are described by the included equations.

According to the test results, once tensile strength σ_a of 194.5 MPa is reached in the rebars, a slight increase in stationary potential over time is observed. In the case of a 1.5 mm layer, potential E_o remains constant (close to 0 mV) in the whole test period. It also remains constant for the uncoated reference rebars, but at a level much different from 0 mV.

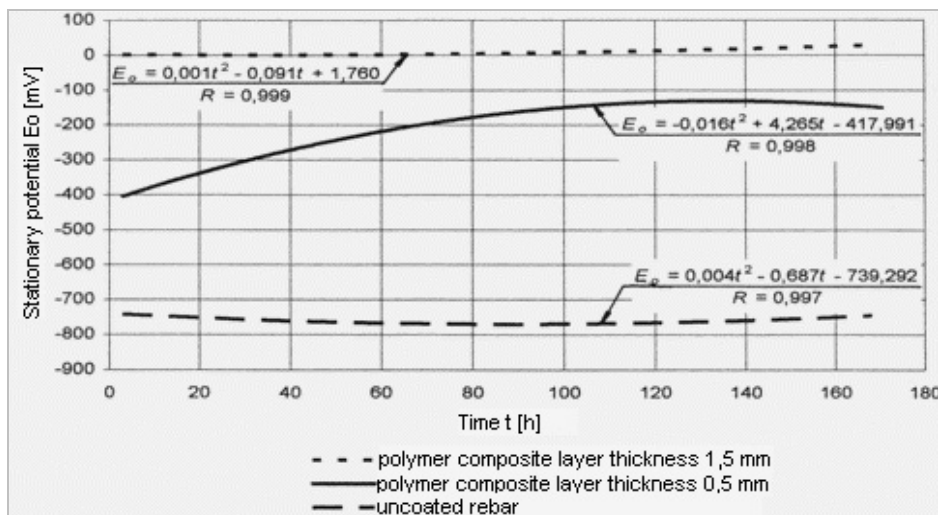


Fig. 12. Stationary potential versus time and constant tensile stress $\sigma_a = 194.5$ MPa for plain rebars 10 mm in diameter, coated with sulphur polymer composite and for uncoated rebars

4. Conclusions

It can be concluded from the test results that the tested sulphur polymer composite can provide surface corrosion protection to the reinforcing steel in concrete. Sulphur composites have not been applied for this purpose before.

The tests have shown that a proper thickness of the sulphur polymer composite and the type of surrounding corrosion environment are important factors here. One can conclude that the optimum thickness of the sulphur polymer composite layer should be

1.5 mm and the reinforcing steel protected with this composite should not be used in aqueous solutions of HNO_3 and KOH and NaOH .

The authors are aware that although the range of the tests carried out so far is quite wide, still further tests are needed to ultimately determine the suitability of the sulphur polymer composite for the surface protection of the reinforcing steel in concrete against corrosion. Also a simple and practical technology of applying this material to the surface of reinforcing steel needs to be developed.

References

- [1] Brandt A.M.: *Problem of durability of high performance concrete*, RILEM-3C-Workshop "Durability of HPC", Vienna, 1994.
- [2] Cairns J., Ramli B.A.: *Influence of rib geometry on strength of epoxy-coated reinforcement*, ACI Structural Journal, I–II, 1995.
- [3] Czarnecki L., Garbacz A.: *Evaluation of polymer coating-crack-bridging ability*, International Colloquium "Industrial Floors", Vol. 95, Esslingen, 1995.
- [4] Czarnecki L., Garbacz A., Łukowski P., Clifton J.: *Polymer composites for repairing of portland cement concrete*, Compatibility Project, NIST Report. United States Department of Commerce, National Institute of Standards and Technology, Gaithersburg MD, 1999.
- [5] Czarnecki L., Emmons P.H.: *Naprawa i ochrona konstrukcji betonowych*, Wyd. Polski Cement, Kraków, 2002.
- [6] Gillot Z.E., et al.: "Sulphur 82", London, 1982, pp. 1–45.
- [7] Hadje-Ghafari H., et al.: *Bond of epoxy-coated reinforcement: cover, casting position, slump, and consolidation*, ACI Structural Journal, I–II, 1994.
- [8] Hoła J.: *Experimentally determined effects of technological and service factors on stress-induced destruction of concrete under compression*, Engineering Transactions, Vol. 50, 2002, pp. 251–265.
- [9] Jankowski L., Pędziwiatr J., Styś D.: *Some research problems due to the bond phenomenon between steel and concrete*, 18th Symposium on Experimental Mechanics of Solids Jachranka, 1998.
- [10] Jaśniok M., Jaśniok T., Zybura A.: *Assessment the corrosion risk of reinforcing concrete using the DC and AC methods*, Gliwice, 2003.
- [11] Jaśniok T., Zybura A.: *Modelling of polarization range of steel bars in corrosion test of reinforced concrete*, 14th Conference "KONTRA 2004" Durability of buildings and protection against corrosion, Zakopane, 2004.
- [12] Jaśniok M., Zybura A.: *Zabezpieczenie i regeneracja zagrożonych korozją konstrukcji z betonu. O przeciwkorozyjnym działaniu otuliny betonowej na zbrojenie*, Przegląd Budowlany, No. 1, 2007, pp. 20–25.
- [13] Klakočar-Ciepacz M., Książek M.: *Investigation of the intensity of corrosion processes influence by tensile stress for reinforcing steel covered with sulphuric coating. Chemicals in sustainable agriculture*, Jesenik, 2003, pp. 761–765.
- [14] Książek M.: *Usefulness of polymer sulphur composites to the protection against corrosion of reinforcement and concrete*, Doctoral dissertation, Series PRE report, No. 3, Wrocław, 2004.

- [15] Książek M.: *Polarisation for reinforcing steel covered with polymeric sulphuric coating under the tensile stress*, 15th Conference "KONTRA 2006" Durability of Buildings and Protection Against Corrosion, Zakopane, 2006.
- [16] Nicles G.: *Inorganic sulphur chemistry*, Amsterdam–London–New York, 1968.
- [17] Ścisławski Z.: *Ochrona konstrukcji żelbetowych*, Arkady, Warszawa, 1999.
- [18] Thelford T.: *Coating protection for reinforcement. Comite Euro-International Du Beton. State of the art report*, 1995, pp. 51.
- [19] Treece R.A., Jirsa J.O.: *Bond Strength of Epoxy-Coated Reinforcing Bars*, ACI Materials Journal, III–IV, 1989.
- [20] Tuller W.N.: *The Nature of Sulphur*, Data Book, New York, 1954.
- [21] Wieczorek G.: *Pore solution properties in concrete with chlorides*, Kurdowski Symposium "Science of cement and concrete", Kraków, 2001.
- [22] Wieczorek G.: *Korozja zbrojenia inicjowana przez chlorki lub karbonatyzację otuliny*, Dolnośląskie Wydawnictwo Edukacyjne, Wrocław, 2002.
- [23] Zybura A.: *Modelling of the reinforcement corrosion of the scratching concrete cover*, Corrosion of Cement Paste, Kraków, 1994.
- [24] Zybura A.: *Zabezpieczenie konstrukcji żelbetowych metodami elektrochemicznymi*, Wydawnictwo Politechniki Śląskiej, Gliwice, 2003.
- [25] Zybura A.: *Electrochemical corrosion protection of concrete structure reinforcements*, Ochrona przed Korozją, No. 1/2007.

Badania przydatności polimerowego kompozytu siarkowego do ochrony przed korozją stali zbrojeniowej w żelbecie

W pracy przedstawiono rezultaty badań doświadczalnych i analiz wykazujących przydatność polimerowych kompozytów siarkowych do ochrony przed korozją stali zbrojeniowej.

Dokonano przeglądu literatury, między innymi w zakresie wybranych zastosowań polimerowych kompozytów siarkowych w budownictwie, metod i sposobów powierzchniowej ochrony przed korozją stali zbrojeniowej i betonu, a także metod i sposobów oceny szczelności warstw zabezpieczających te materiały przed korozją.

Sprecyzowano także zakres badań własnych i stosowanej metodyki. Przeprowadzono badania wstępne obejmujące ustalenie składów i warunków wytwarzania oraz zbadano podstawowe własności fizyczne i mechaniczne wytworzonych próbnich polimerowych kompozytów siarkowych. Dokonano analizy uzyskanych rezultatów badań wstępnych i wytypowano polimerowy kompozyt siarkowy, spośród próbnich, do dalszych badań zasadniczych.

Przeprowadzono badania zasadnicze dla wybranego, spośród próbnich, polimerowego kompozytu siarkowego, w tym: zbadano przyczepność do prętów zbrojeniowych gładkich i żebranych, określono ubytki masy zarówno kompozytów, jak i prętów zbrojeniowych, pokrytych warstwą kompozytów i przechowywanych w roztworach wodnych kwasów, wodorotlenków i soli oraz w wodzie, wykonano badania polaryzacyjne dla prętów zbrojeniowych pokrytych i nie pokrytych taką warstwą. Wykazano przydatność polimerowych kompozytów siarkowych do powierzchniowej ochrony przed korozją stali zbrojeniowej.



Investigations on the applicability of chemically deposited Ni-shell tools for deep-drawing processes

W. HUFENBACH, J. JASCHINSKI, R. GOTTWALD
Institut für Leichtbau und Kunststofftechnik, TU Dresden, Germany

B.-A. BEHRENS, M. DEMIR
Institut für Umformtechnik und Umformmaschinen, Leibniz Universität Hannover, Germany

The paper introduces the results of an EFB (European Research Association for Sheet Metal Working) research project concerning the applicability of tools made of chemically deposited nickel shells with polymer supports for small and medium scale deep drawing production. Several investigations of the material behaviour and tribological response of the chemically deposited nickel shells were performed together with numerical analyses of the deep-drawing process in order to optimize the tools under the consideration of the specific characteristics of the nickel shell and the polymer support structure. Finally, an optimized tool prototype has been manufactured and tested in order to verify the design solutions under service conditions.

Keywords: *NVD-process, electroforming, nickel, deep drawing process, plastic*

1. Introduction

Conventional tools for deep drawing processes can be made of several material types depending on the specific applications and requirements. The most common materials used in deep drawing tools for mass production are steel and cast iron due to their high strength and good durability.

On the other hand, due to the increasing diversity of product variants, especially in the automotive industry, smaller production scales are becoming more important and deep drawing tools made of steel and cast iron become economically disadvantageous for the production scales applied. The use of plastic tooling as a cheaper alternative for such small scale production has however the disadvantage of limited durability [1–3].

A known possible alternative is the use of electroformed metallic shells as wear resistant surface with a polymer support structure which achieves a considerably higher tool life span.

Basic findings were already discovered in a previous research project [4]. It has been shown that electroformed metallic shells can replace steel and cast iron tools in the range of the middle series in the future. Previous studies also showed that a potential cost savings of up to 40% are possible by the use of electroformed metallic shells instead of conventional tools. The savings primarily arise by shortening the process chain of the production and reducing the use of machining tools. One

disadvantage of this tool system is the long time required to deposit the metallic shell (1 mm per week). Furthermore, the connection between the shell made of nickel and the polymer support offer a large potential for cost savings and the improvement of operational strength.

The paper introduces the results of an EFB (European Research Association for Sheet Metal Working) research project concerning the applicability of tools made of chemically deposited nickel shells with polymer supports for small and medium scale deep drawing production. The specific advantages compared to electroformed metallic shells are summarized in Table [5].

Table. Comparison of electroformed and chemical deposited shell tools (according to [2])

Electroformed nickel shell tool	NVD shell tool
+ fast fabrication of polymer negative + unlimited tool size – long process time: 1 mm / week – non uniform layer thickness	+ short process time: 0.25 mm/hour + uniform layer thickness – temperature-resistant negative form required – thermal shape distortion possible – restricted tool size (tool dimensions: 1.900 mm × 1.200 mm)

The consistent further development of nickel shell tools is the aim within the ongoing research project. At the beginning of the research project several possible tool materials have been characterised to provide appropriate mechanical parameters for the numerical simulation of the hybrid tool system. The tool development shall be supported by finite element methods (FEM) so that the entire tool design can be optimized using wide investigations on several material and geometry variations. Following to the described work the findings shall be implemented in a technology demonstrator.

2. Material characterisation

As a basis for the numerical simulations the mechanical properties of polymers and shell materials were investigated in compression tests. In cyclic load tests all analyzed polymers show as expected significant, but for the application not critical, reduction of stiffness and strength. The short-term values for stiffness and strength at compression as well as their change due to cyclical stress (100 000 and 1000 000 cycles, each with 35% of maximum force) were found. In the result “ebablock W” from Ebalta was the preferred material for the polymer support. This is characterised by a high elastic modulus and uncritical failure behaviour with high plasticity (Figure 1).

Furthermore, compressive and tensile tests have been used to determine the required mechanical properties of NVD-nickel material. For the numerical simulation the young’s modulus, yield limit and yield curve of vapour-deposited nickel material are provided (see Figure 2).

The hardness over the shell thickness is adjustable in the production by special additives. The hardness has been characterised over the thickness using micro-hardness testing.

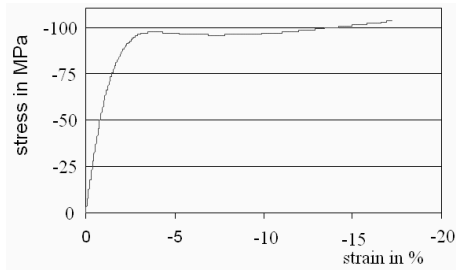


Fig. 1. Stress-strain-behaviour of "ebablock W" in quasistatic compression test

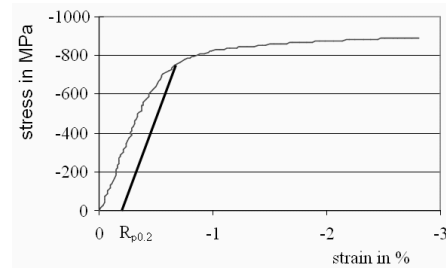


Fig. 2. Stress-strain-behaviour of the NVD-material in quasistatic compression test

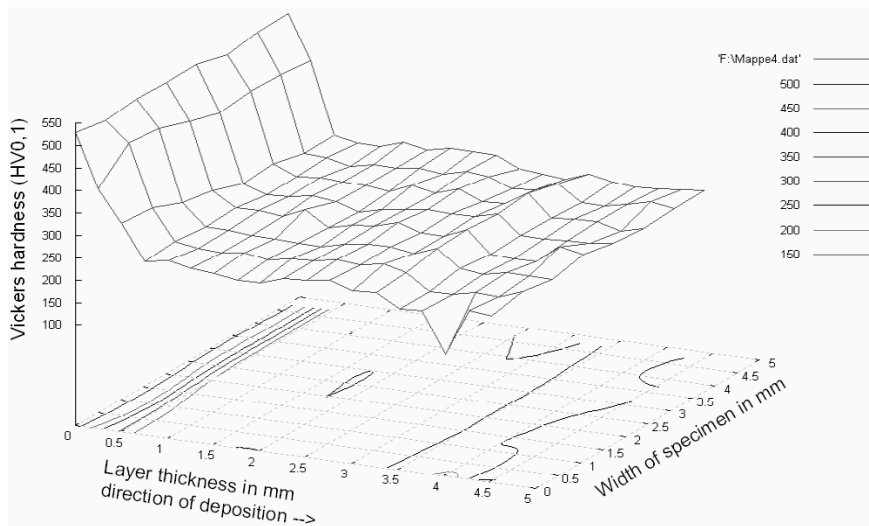
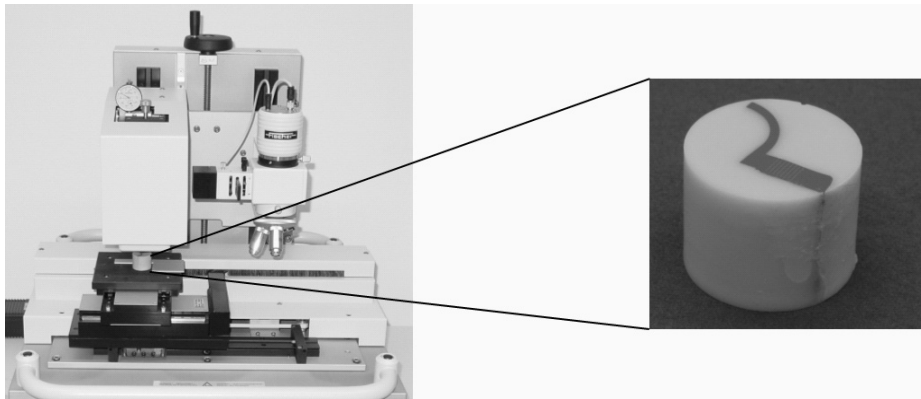


Fig. 3. Results of micro-hardness testing at nickel shell material

As shown in Figure 3, the used material has an increased hardness on the active side of the selected nickel shell, which is a benefit to the demands on the hard tool use.

In further investigations tensile strip tests (with direction change) after Wittüser have been executed to assure the frictional characteristics. In the result different frictional coefficients as a function of material and lubricants can be provided for the nickel shell material.

3. Numerical simulation

To optimize nickel shell tools in a first step, the study of different parameters and connections is done at simple principle models. This approach allows a variety of modifications with relatively low modelling and calculation efforts at a good comparability. The results are incorporated into the design and simulation of a demonstrator tool.

A simple cupping test was chosen as a principle image of a deep drawing process. Therefore, two rotationally symmetric tool models (with open and closed bottom) are the basis for investigations of different variations and boundary conditions.

At the die plate, consisting of nickel and polymer support, the influence of the parameters nickel layer thickness as well as interface to the support are investigated (Figure 4).

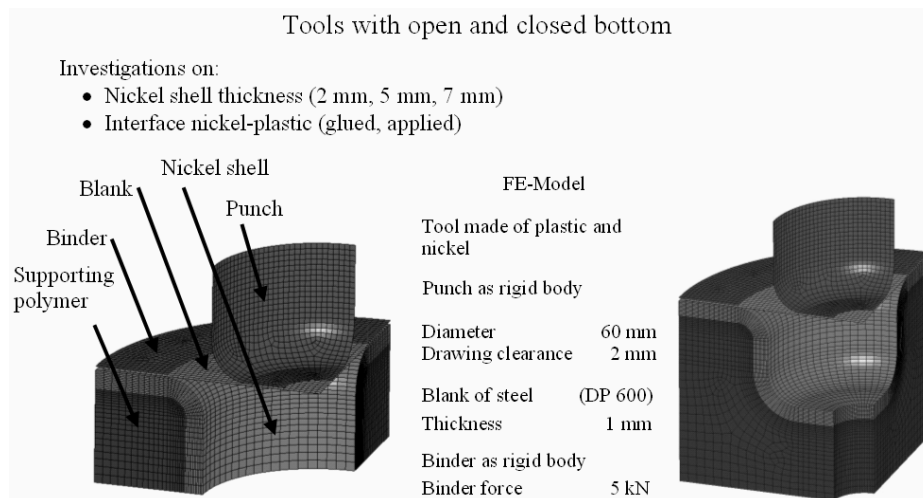


Fig. 4. Principle models for numerical investigations

The deep drawing process is simulated in LS-DYNA and consists of the three steps:

- 1) the binder (rigid body) strikes damped on the blank,
- 2) the punch (rigid) lowers with a defined speed,
- 3) the blank of steel is formed into a cup.

The moving back of the punching tool and the discharge of tools and the blank are not covered by the investigations.

It has been shown that parameters such as strength or frictional coefficient are only little sensitive in the considered range of the properties in the numerical investigation. The analyses of the different variants show that the in the forming process induced stresses at the nickel shell and the supporting polymer can strongly be influenced by the tool design. The shell thickness has as expected a high importance. The first investigation of the principle models results in a design tool with a closed bottom because the stress is additionally distributed on the areas of the bottom. For repairs or modifications of the nickel shell a severability of the supporting polymer is important. Therefore, the shell is furthermore investigated in applied condition.

A nickel layer thickness of only 2 mm leads to high stresses at the nickel shell and the polymer support, so that it is unsuitable for the practical use. A 5 mm thick nickel shell and its polymer support undergo relatively small, mainly elastic, deformations. This variant is favoured and used for the subsequent numerical investigation of a demonstrator tool.

An S-Rail structure was selected as demonstrator to evaluate a nickel shell tool which is separated from the gas phase in NVD-process. Therefore, a FE-model of the Numisheet'96 benchmark component "S-Rail" was set up for the simulation (Figure 5).

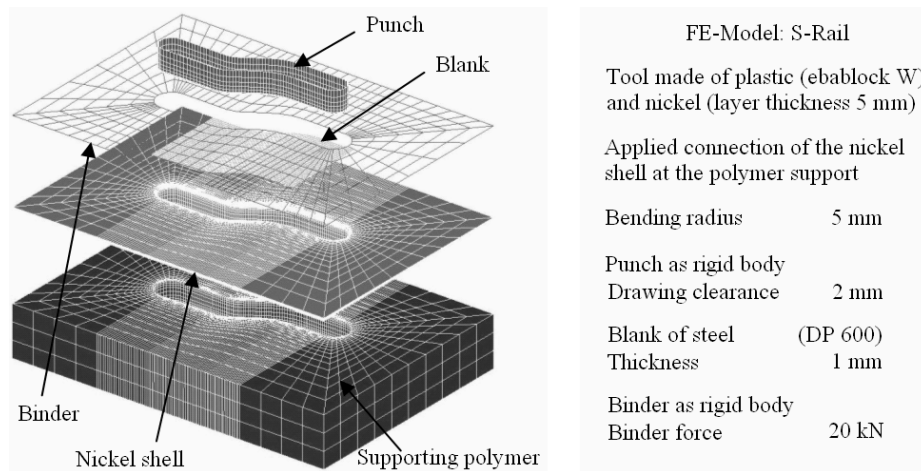


Fig. 5. FE-Model of nickel shell-demonstrator tool "S-Rail"

The stresses of the support were evaluated after the criterion of v. Mises. In the result of the simulation the stress of the polymer support can be considered as uncritical (Figure 6) as well as the stresses of the nickel shell. Eventually small local initial plastic deformations (first work in cycles) have to be expected below the $R_{p0.2}$ value during the deep drawing process (Figure 7).

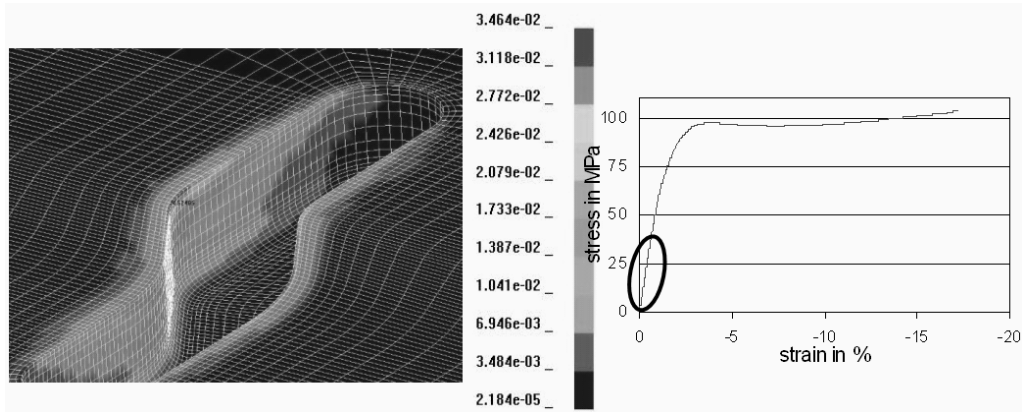


Fig. 6. Stress according to v. Mises (in GPa) in polymer support of S-Rail-model

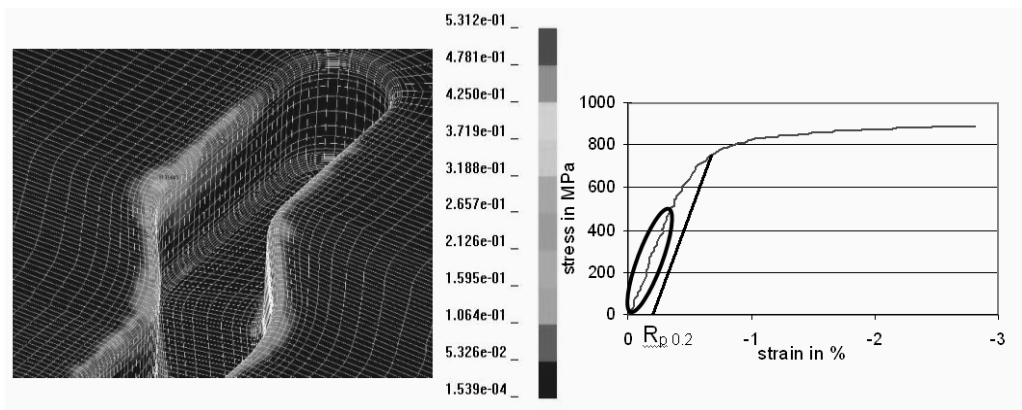


Fig. 7. Stress according to v. Mises (in GPa) in nickel shell of S-Rail-model

4. Test of the demonstrator tool “S-Rail”

An original S-Rail tool made of cast iron was provided from the company DAIMLER AG to obtain the demonstrators geometry. For the production of a chemically deposited nickel shell a negative model is created from the tool. In a special coating chamber a nickelous gas is directed on the model, so that pure nickel is chemically separated under certain process conditions. Afterwards the selected polymer is casted behind the nickel shell to build up the support. The whole tool system is fixed in a HYDRAP-press to perform a defined test program (Figure 8).

1000 test cycles are carried out with DP 600 as a model blank material with high strength. Nickel shell tools are not necessarily supposed to form DP 600, but from the results it is supposed that conclusions can be drawn for less strength blank materials at higher quantities. The results show the successful deep-drawing of DP 600 blanks by

the use of a nickel shell tool with complicate geometry produced by the NVD-process. The tests have confirmed the predicted numerical simulated deformation of the blank very well.

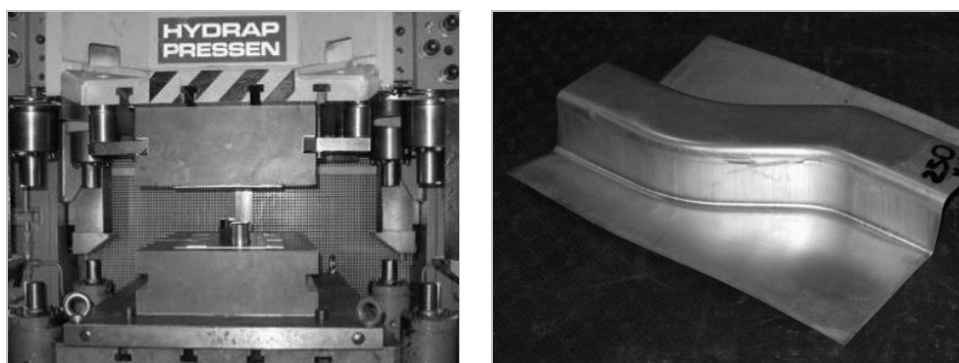


Fig. 8. Fixed nickel shell tool system in press (left), blank with S-Rail structure (right)

In addition the mechanical wear has to be evaluated in future investigations. At last the metal removal at the drawing radius shall show the ability to modify NVD-shell tools.

Acknowledgement

This project (ref. no. 14591 BG) was funded by the German Federal Ministry of Economics and Technology under the responsibility of the AiF (German Federation of Industrial Research Associations).

The authors would like to thank the European Research Association for Sheet Metal Working (EFB), the Project Accompanying Committee (PbA) and the Working Committee (AK) for the support during the realisation of the project.

References

- [1] Hochwald P., Jaschinski J., Lösch S., Mekkaoui M. A.: *Erprobung von Polymeren als Werkzeugwerkstoff für den Umformprozess*, BMBF Abschlussbericht 03N3054, 2003.
- [2] Frank C.: *Tiefziehwerkzeuge aus Kunststoff für mittlere Serien*. Diss., Uni Hannover, 1999.
- [3] Deiler G.: *Tiefziehwerkzeuge für Kleinserien*. Diss., wt Werkstattstechnik online, Springer-VDI-Verlag, Düsseldorf, 2001, Ausgabe 07, pp. 428–432.
- [4] Behrens B.-A., Mütze S.: *Galvanoschalen für die Blechumformung*, EFB/AiF Forschungsbericht 12918 N, Hannover, 2004.
- [5] Behrens B.-A., Demir M., Hufenbach W., Jaschinski J., Gottwald R.: *Optimierung von Galvanoschalenwerkzeugen*, Abschlussbericht zum Forschungsvorhaben, Band 285 – ISBN 978-3-86776-319-6, EFB Hannover, 2008, (not yet published).

Badania przydatności nanoszonych chemicznie powłok niklowych na narzędzia stosowane w procesach głębokiego tłoczenia

Artykuł przedstawia rezultaty badań EFB (European Research Association for Sheet Metal Working) projektu dotyczącego przydatności narzędzi wykonanych poprzez nanoszenie chemicznie powłok niklu na polimerowe obudowy dla małej i średniej produkcji wyrobów tłoczonych. Przeprowadzono wiele badań parametrów trybologicznych nanoszonych chemicznie powłok niklowych razem z analizą numeryczną procesu głębokiego ciągnięcia, w celu zoptymalizowania narzędzi pod kątem określonych cech powłoki niklowej i polimerowej obudowy. W rezultacie stworzono zoptymalizowany prototyp narzędzia, który został przetestowany w warunkach serwisowych, w celu sprawdzenia prawidłowości zastosowanych rozwiązań.



The evaluate of laser welded tailor and tubular blanks formability for automotive vehicle elements stamping

M. HYRCZA-MICHALSKA, F. GROSMAN

The Silesian University of Technology, Akademicka 2A, 44-100 Gliwice, Poland

The laser welded blanks and tubes take wide range in application as materials for forming of automotive vehicle elements. The heterogeneity of structure and properties in laser weld area has an effect on welded blanks behavior in the plastic forming process. For quantitative evaluation of this heterogeneity influenced on plastic strain course, necessary is to determine characteristics of laser welded blanks mechanical properties. It has a particular meaning in accomplishing selection of proper laser joined sheets and tubes sets, allowed to receive designed quality of presswork. It is difficult to find a universal method of those kinds of welded blanks drawability evaluation, more when joining elements are made of different materials. In this paper are pointed out the important issues at elaborating of those kinds welded blanks drawability evaluation, with special include laser welded tubes drawability evaluation for hydroforming process. Besides, there are presented examples of laser welded sheets and tubes, which are research program objects at Department of Process Modeling and Medical Engineering of The Silesian University of Technology. There is presented research capabilities of designed and built laboratory stand for tubes hydromechanical bulging.

Keywords: *tailored blanks, tubular blanks, drawability evaluation, hydroforming*

1. Introduction

One of the latest technologies introduced into manufacturing of car body elements is hydroforming of laser welded tailored blanks. The first laboratory and industrial experience with stamping of laser welded blanks, which was elaborate in Department of Process Modelling and Medical Engineering of the Silesian University of Technology, allowed to start research on tubes hydroforming processes. The recognition of joined sheet and weld joint mechanical properties and proper their drawability evaluation gives the parameters for lead up forming and hydroforming of welded blanks. In this paper is presented method of drawability evaluation for both processes using welded blanks and tubes. The application of this method is presented for laser welded blanks. However first results for tubes' hydroforming are described.

2. The method of drawability laser welded blanks and tubes evaluation

Research on the development of welding and forming technologies have revealed that the influence of a weld upon the process of plastic flow of the pass in the zone of joining can be examined using the same kind of test as those used for evaluating the drawability of homogeneous sheets. However, the tools for drawability test applied in

technological trials appeared not to be suitable enough for trials on tailored blanks which are of different thickness. Therefore a series of experiments allowing evaluation of drawability of laser-welded tailored blanks has been performed. In such experiments, the thickness of steel sheets is not of particular importance. A detailed analysis carried out proved that such characteristics as those obtained in tensile test of welded strips and the weld itself can only be appropriate for preparing preliminary classification of laser-welded tailored blanks. Thus it is of great importance to examine all the welds, taking into account different ways of joining steel sheets in a given tailored blank so that full assessment of drawability of laser-welded tailored blanks can be made. The examinations should include:

- technological tests, e.g. cup drawing test, cupping (Swift's method); KWI, hydraulic bulging and bending tests,
- evaluation of microstructure of the welded zone,
- measurements of microhardness distribution alongside the weld, exemplary using Vickers method.

In the case of tailored blank shown in Figure 1a, it was necessary to evaluate drawability of three tailor welded sheets, which joined blanks A-A, B-B, and A-B. In industrial trials was used blank for b-pillar showed in Figure 1b.

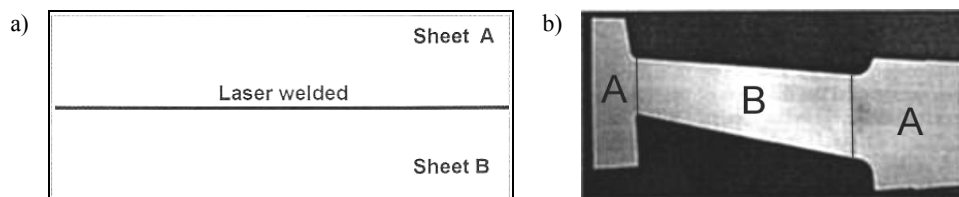


Fig. 1. Examples of joining sheet in tailor welded blank type A-B:
a) welded blank used in laboratory tests, b) welded blank used in industrial trials

Figure 2 presents the chart of the distribution of samples in strip of laser-welded tailored blank. It was difficult to fix the samples (the samples were from laser-welded tailored blanks of different thickness, with the weld positioned in accordance with the direction of stretching) inside flat jaws of a tensile testing machine, therefore a special kind of fixture with a hole for blocking out the sample was used. Figure 3 shows results of tensile test for samples where welds are oriented in different ways to the loading direction. Results presented on Figure 4 show differences between typical sheet and tailor welded blanks behaviour during different drawability tests.

All the suggested mechanical properties of the sample as well as the parameters of its work hardening curve (flow curve) which are essential for designing a material model of welded zone used for the simulation of laser-welded tailored blanks forming process, applying the finite elements method (FEM), have been determined as well [1, 2]. The results of simulation laboratory test for laser welded blanks type A-B and definition of their mechanical parameters had been presented in earlier publications [3, 4].

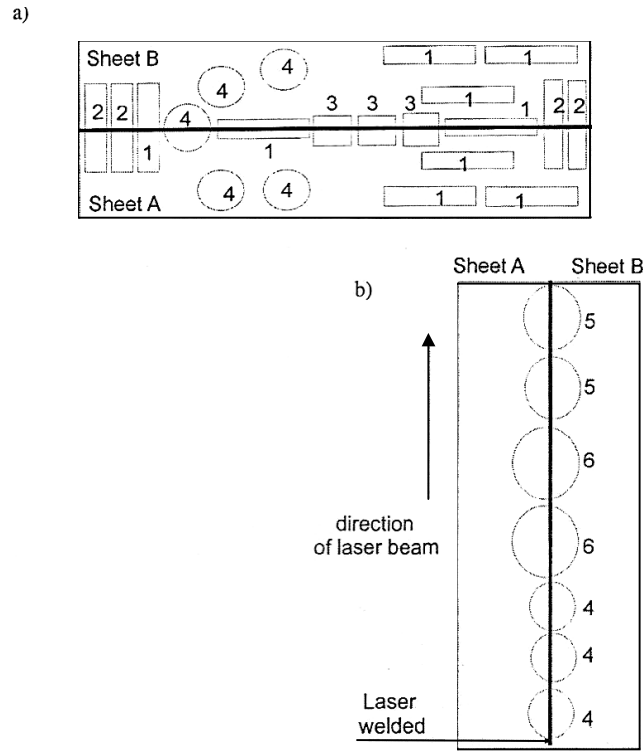


Fig. 2. The scheme of patterns of taking samples from the exemplary strip. Tests notation:
 1 – tensile test, 2 – bending test, 3 – cup drawing test, 4 – cupping (Swift’s method),
 5 – KWI test – bugle forming of the hole, 6 – hydraulic bulging

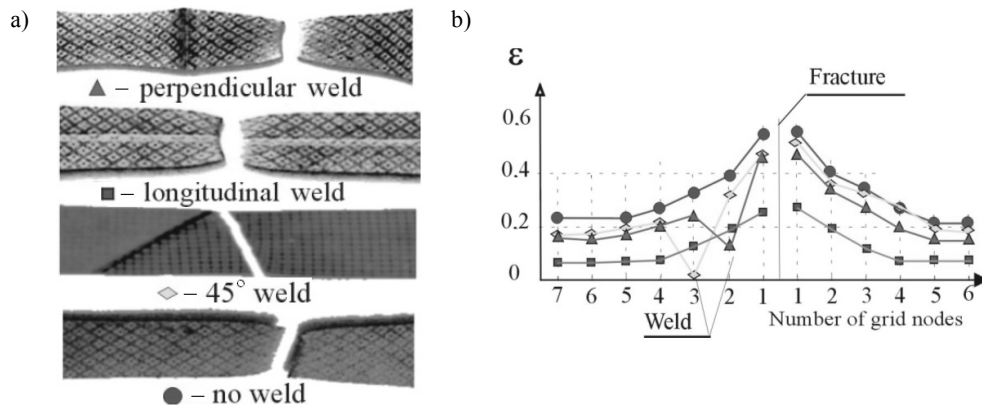


Fig. 3. Results of tensile tests: a) pictures of samples (sheet thickness 1.2 mm) fractured during tensile tests; welds are oriented in different ways to the loading direction, b) distributions of local strains along tensile load direction

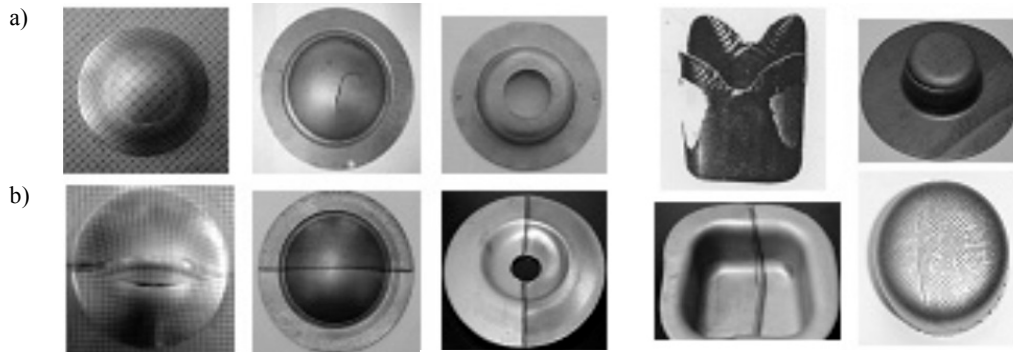


Fig. 4. Results of drawability tests: a) pictures of samples of typical sheet, b) pictures of tailor welded blanks samples

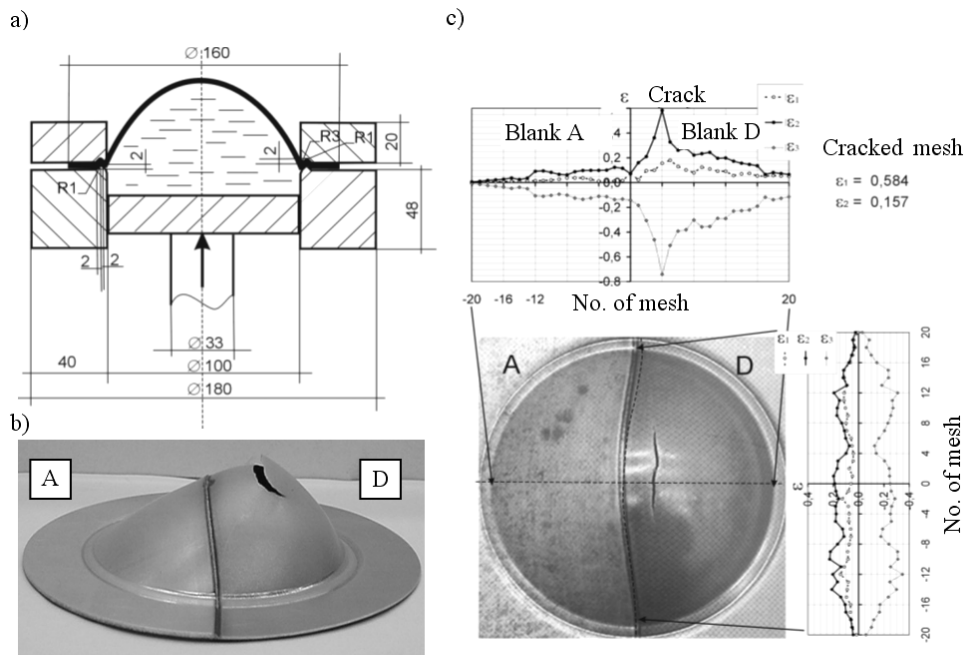


Fig. 5. a) Diagram of the tools used in the test of hydraulic bulging in matrix $\varnothing 100$ mm, b) photograph of a drawpiece made of laser welded tailored blanks of A and D, c) distribution of local strain along and perpendicular to the weld for a drawpiece bulged by liquid [12]

The forming limit diagram (FLD) determined for the criterion of cracking has been presented in Figure 6. The values of local strains presented in Figure 5c have been shown in these diagrams. The results obtained proved that the laser weld changes significantly the mechanical properties of laser welded tailored blanks in the zone of

joining. The line in Figure 6 which indicates the growth of strain demonstrates that the weld restricts the deformation of the blank along the weld line in the process of bulging by liquid. Although the process of deformation in blanks takes place when there is biaxial tension, the minor strain ε_2 along the weld is much smaller than the strain in zones more distant from the weld. The weld is deformed under plane strain conditions near the top of the bulging (Figure 5c, 6b).

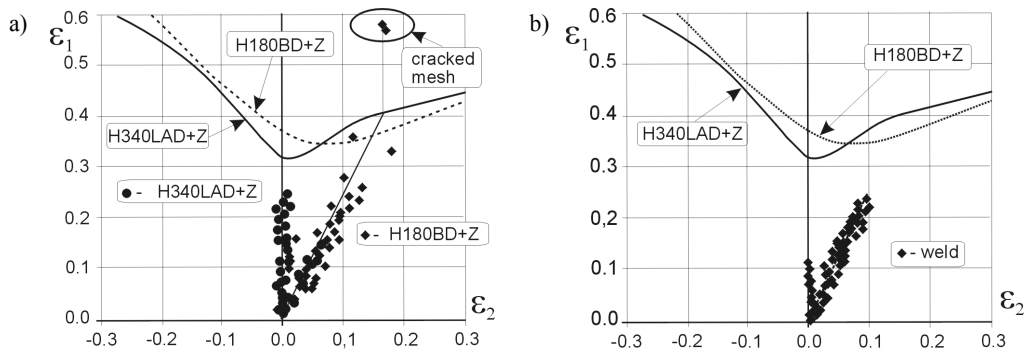


Fig. 6. a) FLD with local strains along the line perpendicular to the weld,
b) FLD with local strains along the weld for the studied blanks [12]

The process of cracking of a blank, which was bulged by liquid, takes place at constant value of strain measured alongside the groove and it is the same as ε_2 strain – the uniform strain (Figure 6a). The analysis of local strain revealed that different thickness of welded blanks and different mechanical properties have a considerable impact on the resulting changes. This is due to the fact that there has to be equilibrium of acting forces upon a unitary section. The following condition needs to be satisfied in the plastic state for blanks A and D:

$$\sigma_{pA} t_A = \sigma_{pD} t_D, \quad (1)$$

where:

σ_{pA}, σ_{pD} – yield stress,
 t_A, t_D – thickness of blank A and D.

The process of hydromechanical bulging of laser welded tailored blanks is not the same as in homogeneous blanks. These changes are caused by the difference in thickness and properties of the joined materials and lower plasticity of the weld as compared to tailored blanks. In general, formability of laser welded tailored blanks depends on the plastic properties of the weld and relationship between the strength of joined sheet components. The changes of local strain for the zone of joining are mainly related to the impact of the weld zone upon the flow of blanks in the neighbourhood of the weld [11, 12].

Method of evaluating the drawability of laser-welded tailored blanks used for analyzing an actual process of forming has been presented. It seems to be quite satisfactory and evidences that introducing laser-welded tailored blanks instead of conventional steel sheets which have been previously used is far more advantageous. The presented example of a centre pillar (b-pillar) illustrates it best because the location of the weld and the type of tailored blanks have been selected on the basis of examination results. In Figure 7a welded pass of laser welded tailored blanks for b-pillar is shown. The effects of this blank execution in stamping process are presented in Figure 7b. Appropriate washers made of steel sheet, which would level the differences in thickness of tailored blanks, had to be used in technological trials. Results of local strain measurements in areas of weld 1 and weld of b-pillar drawpiece made of tailor welded blank are shown in Figures 8 and 9. Distribution of local strain according to Forming Limit Diagram of joined sheets is presented in Figure 8b and 9b.

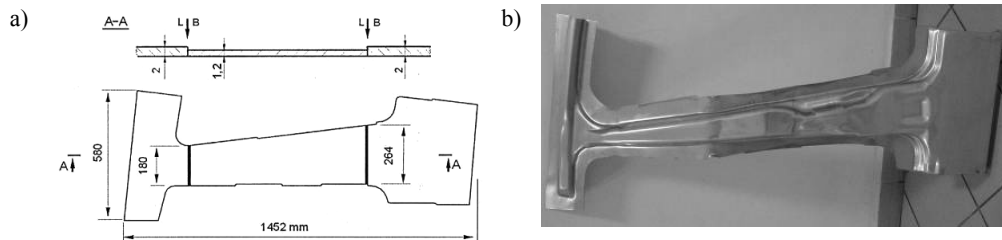


Fig. 7. Welded pass of laser-welded tailored blank (a), the tailor welded blanks type A-B execution in stamping process – first operation of b-pillar stamping (b)

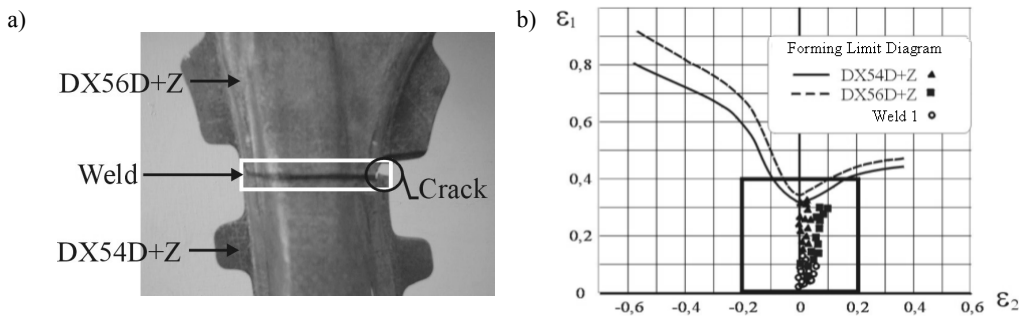


Fig. 8. Photography of weld 1 with marked area of local strain measurements (a), distribution of local strain according to Forming Limit Diagram of joined sheets of b-pillar drawpiece

In effects of comparison of measured values of local strain on weld 1 and weld 2 areas, occurs that is no technological unsafe values of local strain in area of weld 2. Some values in area of weld 1 (direction ε_1) are in close neighbours of FLD of DX54D+Z sheet blank. Because of it there was no possibility to completely reduce

cracks in b-pillar drawpiece flange area. That flange area is cutting on the end of drawing process.

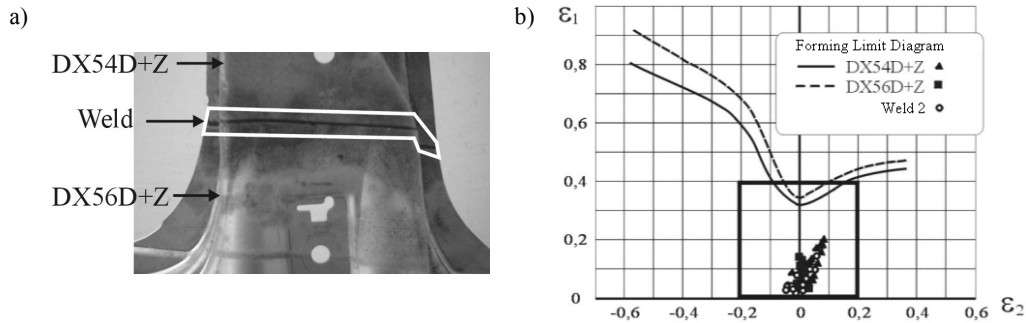


Fig. 9. Photography of weld 2 with marked area of local strain measurements (a), distribution of local strain according to Forming Limit Diagram of joined sheets of b-pillar drawpiece

Flow of tailor-welded blanks in a process of deep drawing is considerably different from the flow of homogeneous blanks. In the case of tailored-welded blanks, reduced elongation along the weld line is observed. Another effect presents in drawing of tailored-welded blanks made from the base materials of different strength or thickness is a movement of the weld line towards the material of greater strength or thickness. In order to obtain correct results, it is important to take into account different mechanical properties of the weld zone in numerical modelling of tailored-welded blanks. Therefore a physical model of the weld zone has been proposed here with mechanical properties of the weld- and heat-affected zones identified using microhardness measurements.

3. The proposal of laser welded tubes drawability evaluation for hydro forming process

The described method was used in evaluation of blanks for preparing open joint tubes for tubular blanks. Those open joint tubes were join using Nd:YAG laser and tested on laboratory stand for testing flexibility of tubes for hydroforming (shown in Figure 10a), which is built in Department of Process Modelling and Medical Engineering of the Silesian University of Technology. In the first stage of hydroforming tests, for laser welded tubes, were used tailor welded tubes shown in Figure 10b (where dimension of tube is $d_z = 45$ mm, wall thickness is $g_0 = 1.5$ mm), made of the same sheet. Basic sheet mechanical properties are shown in Table 1. The laser welded tubes were tested in process of unbounded hydroforming and the results for these tests were presented in earlier publications [5–7]. The design of the equipment and the performed hydromechanical forming examinations should combine basic principles of the technology of liquid forming of welded tubes including the laser welded method.

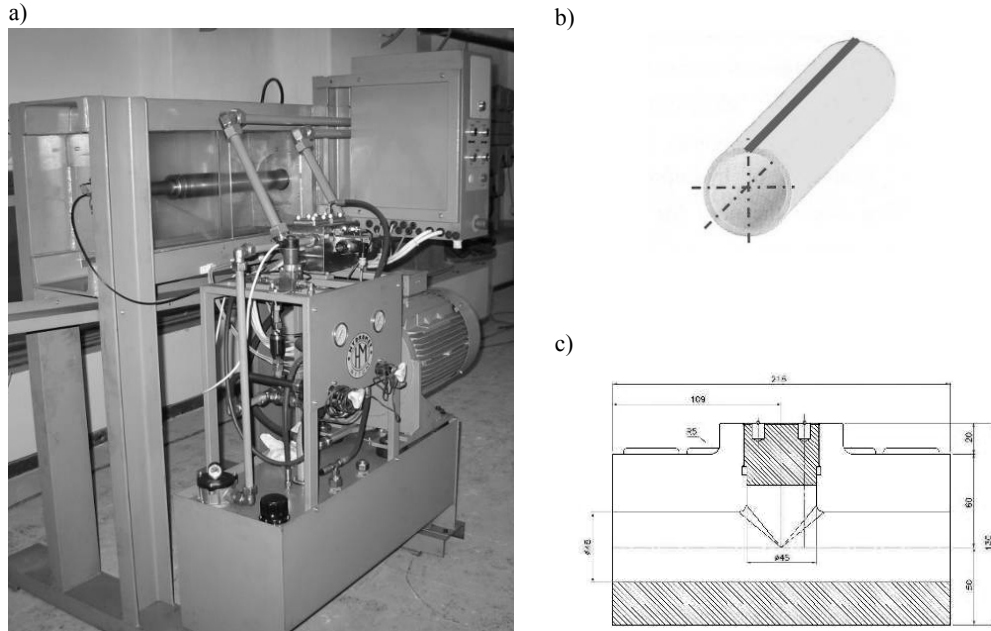


Fig. 10. The photography of laboratory stand for laser welded tubes hydroforming (a); scheme of welded tube exemplary sample (b); scheme of devices for limited hydroforming of tubes

The values of maximum tubes bulged pressure have been derived directly from the following dependence:

$$p_r = \frac{2\sigma_p g_0}{d_z - 2g_0}, \quad (2)$$

where:

p_r – pressure which is used for bulging the tube [MPa],

g_0 – thickness of the tube wall [mm],

d_z – outside diameter of the tube [mm],

σ_p – yield stress of the tube sample [MPa].

The results of hydromechanical bulging of the tube made of 1.5 mm thick blank of DX56D+Z steel grade have been compared to the results obtained in the hydrobulging process of laser welded blanks. The used blanks were of the same thickness and were made of the same steel grade in a round matrix of $\varnothing 100$ mm diameter. The results of hydrobulging of laser welded blanks in a round matrix of $\varnothing 100$ mm diameter have been presented in a more detailed way in paper [8, 9].

Table 1. The characteristic of basic sheet properties using to prepare laser welded tubes

Sheet DX56 D+Z (PN-EN 10327: 2006)										
Thickness [mm]	Rolling Direction	t_s [MPa]	Y_P/Y_S [MPa]	n [-]	C [MPa]	r [-]	Δr [-]	r_{sr} [-]	A_{80} [%]	IE [mm]
1.40	0°	302	170	0.231	76.09	2.2	0.52	2.03	48.8	11.8 SSB
	45°	311	182	0.227	78.05	1.8			47.6	
	90°	300	179	0.220	74.76	2.4			49.5	
After standard	90°	260–350	120–180	0.210 min	–	1.9 min	–	–	39 min	
Sheet H180BD+Z (PN-EN 10292: 2003)										
Thickness [mm]	Rolling Direction	t_s [MPa]	Y_P/Y_S [MPa]	n [-]	C [MPa]	r [-]	Δr [-]	r_{sr} [-]	A_{80} [%]	IE [mm]
1.50	0°	359	261	0.161	84.34	1.7	0.64	1.7	34.8	11.6 B
	45°	355	276	0.151	82.57	1.1			30.0	
	90°	375	264	0.164	88.36	1.9			39.2	
After standard	90°	300–360	180–240+35 po OC	0.160 min	–	1.5 min	–	–	34 min	
Sheet FE 450 DP F; (DP450) –FIAT standard										
Thickness [mm]	Rolling Direction	t_s [MPa]	Y_P/Y_S [MPa]	n [-]	C [MPa]	r [-]	Δr [-]	r_{sr} [-]	A_{80} [%]	IE [mm]
1.60	0°	500	332	0.144	115.48	1.0	0.39	0.98	30.4	11.8 B
	45°	516	337	0.151	120.00	0.8			27.6	
	90°	508	368	0.141	116.98	1.3			29.6	
After standard	90°	450	250–300	0.140	–	–	–	–	27 min	

4. Results of laser welded tubes stamping formability evaluation

To evaluate laser formability welded tubes for stamping, the unbounded hydroforming process were analyzing with use of designed and built laboratory stand. In those research three sheets made of different steel grades (DX56D+Z; H180BD; FE450DP) were using to prepare open joint tubes. The basic mechanical properties of tested steel grades are given in Table 1. Those tubes had been laser welded before hydroforming. To define welds properties the microhardness tests were done for three weld joints (for welded tubes from each steel grade). The results of microhardness measurements for tubes are shown in Figure 11.

The three laser welded tubes made of different steels were tested in unbounded hydroforming process. Those tests were realized on laboratory stand for tubes hydroforming, built in Department of Process Modelling and Medical Engineering. The maximal inner pressure of working liquid (oil) achieved 30 MPa level. The local strain distribution was measured on each tubes using coordination mesh, applied electrochemically on sheets before coiling of open joint tubes. The major local strain distributions ε_1 , measured for net meshes along the laser weld for three tubes hydroformed is shown in Figure 12.

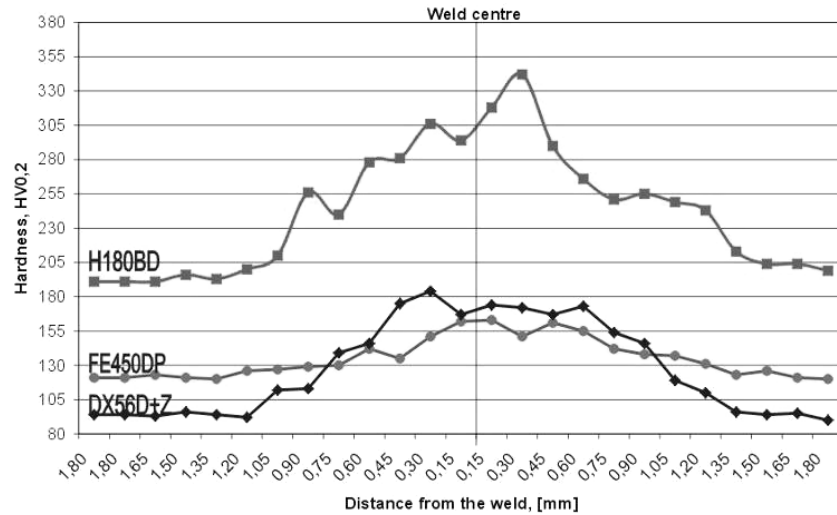


Fig. 11. The diagram of microhardness measurements took parallel to the welds for laser welded tubes [11]

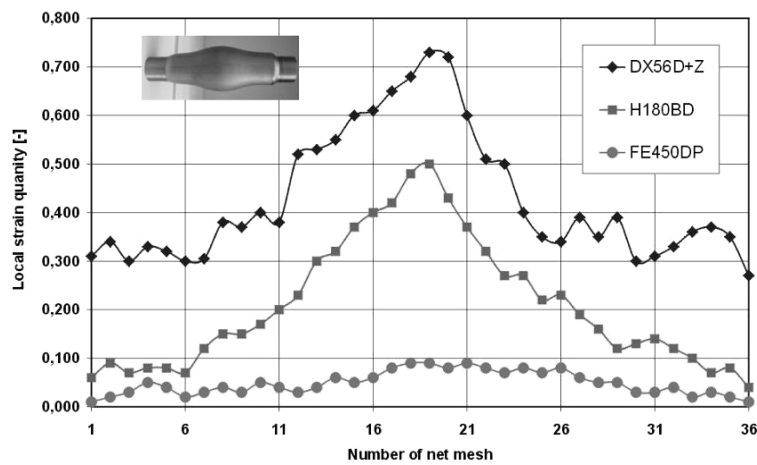


Fig. 12. The major local strain distributions ε_1 , measured for net meshes along the laser weld for three tubes hydroformed with internal pressure of the working liquid 30 MPa [11]

The bigger level of major local strain reach laser welded tube mead of DX56+Z steel grade, whereas the tube made of FE450DP steel grade strain is on very low level. Those characteristics of laser welded tubes formability depend of mechanical properties of basic sheets and their drawability. The laser welds localized along the tubes have small or none influence on formability of presented unbounded hydroforming process, see comparison on Figure 13. From here, it is important to

recognize the influence of the laser welds on tubes hydroforming process realized using devices for limited hydroforming (showed in Figure 10c).

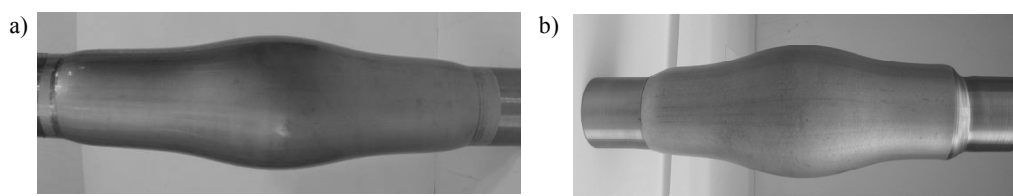


Fig. 13. Comparison of hydroforming effects for tubes: a) tube without weld, b) laser welded tube

5. Summary

Alike the drawability test on laser welded blanks (in laboratory and industrial circumstances) and also the carried out bulging tests on tubes, using specially designed equipment for that purpose, allowed to examine uniform stress up to the moment when blanks or tubes begin to crack. It is also possible to control accurately the force or pressure which are essential for tightening and squeezing of the tube. The tests revealed that tightening is a very crucial element of the process and it can be applied several times only if the head edges of the sample tube have been properly prepared. The used diameters of the samples allow to map co-ordination nets in order to measure local strain. The analysis of local strain distribution of hydromechanically bulged tube and the comparison of the obtained results to the results received in the process of bulging of laser welded blanks in a round matrix of $\varnothing 100$ mm diameter [9] allow to draw the following conclusion: favorable mechanical state in the process of hydromechanical forming (hydroforming) of tubes helps to reach higher values of ε_1 strain for the same values or the values corresponding to ε_2 strain values than those in hydrobulging tests performed in a round matrix of $\varnothing 100$ mm diameter. The results for laser welded tubes hydroforming acknowledge possibility of pressure level determining base on formula (2). The definition of maximum pressure which is used for bulging the tube (p_r) allows to design tubes hydroforming in closed dies [10]. Presented for different welded tubes local strain distributions carry through the accurate selection of steel grades for laser welded tubes of established formability for hydroforming. This conclusion will be applied to lead up tests with devices for limited hydroforming of tubes and at the end find industrial solution for hydroformed tubes production in Poland.

References

- [1] Lisok J., Piela A.: *Praktyka badań procesu tłoczenia blach metodą elementów skończonych MES*, X Konferencja AGH, Politechniki Śląskiej i Komitetu Metalurgii PAN, nt. "Informatyka w technologii metali" KomPlasTech 2003, Wisła-Jawornik 12-15.01.2003, red. F. Grosman, A. Piela, J. Kusiak, M. Pietrzyk, Wyd. „Akapit”, Kraków, pp. 193-206.

- [2] Piela A., Rojek J.: *Symulacja procesów tłoczenia wsadów spawanych laserem*, praca zbiorowa pod redakcją A. Pieli, F. Grosmana, J. Kusiaka, M. Pietrzyka, Informatyka w technologii metali, Wyd. Politechniki Śląskiej, Gliwice, 2003, pp. 353–403.
- [3] Piela A., Hycza M.: *Graniczna krzywa tłoczenia blach typu tailored blanks*, Materiały 8 Międzynarodowej Konferencji FORMING 2001 “Plasticita Materiálov”, Stara Lésna – Vysoké Tatry, Republika Słowacka, 30.08–02.09.2001, pp. 163–170.
- [4] Hycza M., Piela A.: *Przemysłowe próby tłoczenia blach łączonych typu tailored blanks*, Materiały 9 Międzynarodowej Konferencji FORMING 2002, Luhačovce Republika Czeska, pp. 133–138.
- [5] Hycza-Michalska M., Grosman F.: *Problemy doboru wsadów do kształtowania hydro-mechanicznego*, Slovenská Technická Univerzita v Bratislave, Materiały 14 Międzynarodowej Konferencji FORMING 2007 „Plasticita Materiálov”, Podbanské – Vysoké Tatry, Republika Słowacka, 12–15.09.2007, pp. 111–116.
- [6] Hycza-Michalska M.: *Hydroforming jako nowoczesna metoda kształtowania elementów karoserii samochodowej*, Wydawnictwo Czasopism i Książek Technicznych SIGMA-NOT Sp. z o. o., Czasopismo Hutnik – Wiadomości Hutnicze, rok LXXIV, 05.2007, No. 5, pp. 255–259.
- [7] Hycza-Michalska M., Grosman F.: *Badania doświadczalne hydromechanicznego rozpękania rur spawanych laserowo*, Oficyna Wydawnicza Politechniki Warszawskiej Prace Naukowe, Mechanika, zeszyt 216, Materiały Konferencji FIMM 2007 – Fizyczne i matematyczne modelowanie procesów obróbki plastycznej, Warszawa, 17–19.05. 2007, pp. 121–126.
- [8] CIM – mes Projekt Sp. z o.o., ul. Grzybowska 87, 00-844 Warszawa.
- [9] Piela A.: *Hydroforming of laser welded tailored blanks*, Faculty of Metallurgy, The Technical University In Košice, Editor Tibor Kvačkaj, Materiały 4th International Symposium THER TECH FORM’05 “Theoretical and technological problems of steels and nonferrous metal forming”, Acta Metallurgica Slovaca, Košice, special issue No. 2/2005, Vol. 11, 2005, pp. 368–374.
- [10] Hycza-Michalska M., Lisok J., Sikorski Sz.: *Modelling and numerical simulation of unbounded hydro-bulging of laser welded tubular blanks*, Wydawnictwo „AkapiT” Kraków, Department of Modelling and Information Technology AGH, Computer Methods in Materials Science, Informatyka w Technologii Materiałów, Vol. 7, 2007, No. 3, pp. 333–336.
- [11] Hycza-Michalska M., Grosman F. : *The research of laser welded blanks characteristic in basic and technological drawability tests*, Steel Research International, Vol. 79, 2008 Special Edition Metal Forming Conference 2008, Vol. 1, pp. 780–787.
- [12] Piela A.: *Hydroforming of laser welded tailored blanks*, Faculty of Metallurgy, The Technical University In Košice, Editor Tibor Kvačkaj, Materiały 4th International Symposium THER TECH FORM’05 “Theoretical and technological problems of steels and nonferrous metal forming”, Acta Metallurgica Slovaca, Košice, special issue nr 2/2005, rocznik 11, 2005, pp. 368–374.

Ocena podatności wsadów w postaci blach i rur spawanych laserowo do tłoczenia elementów pojazdów samochodowych

Spawane laserowo blachy i rury znajdują coraz szersze zastosowanie jako materiały wsadowe do kształtowania elementów pojazdów samochodowych. Niejednorodność struktury i właściwości w strefie spoiny laserowej wpływa na zachowanie się wsadów w procesie kształtowania

plastycznego. Dla dokonania ilościowej oceny wpływu tej niejednorodności na przebieg odkształcenia plastycznego, konieczne jest wyznaczenie charakterystyk właściwości mechanicznych wsadów spawanych laserowo. Ma to szczególne znaczenie dla dokonania wyboru właściwych zestawów blach lub rur łączonych techniką spawania laserowego, a pozwalających na uzyskanie projektowanych cech wyrobu tłoczonego. Trudnym jest znalezienie uniwersalnej metody oceny podatności do tłoczenia tego typu wsadów, tym bardziej, gdy łączone są elementy z różnych materiałów. W referacie wskazano na zagadnienia istotne przy opracowaniu metodyki oceny tłoczności tego typu wsadów, ze szczególnym uwzględnieniem oceny podatności do hydromechanicznego kształtowania wsadów rurowych spawanych laserowo. Ponadto przedstawiono przykłady blach i rur spawanych laserowo, będące przedmiotem badań własnych w Katedrze Modelowania Procesów i Inżynierii Medycznej Politechniki Śląskiej. Zaprezentowano możliwości badawcze zaprojektowanego i uruchomionego stanowiska do hydromechanicznego rozpęczania rur.



Glazed building wall as a solar thermal collector

T. KISILEWICZ

Cracow University of Technology, ul. Warszawska 24, 33-155 Kraków, Poland

A good chance to separate thermal and living functions of the building shell appears in indirect passive systems, where absorption and accumulation of the transmitted solar energy takes place close to the wall glazing. A wall of this kind, that transmits, absorbs and accumulates solar energy becomes for a building solar thermal collector. In the whole building scale heating demand reduction, due to this passive solar system may reach 14%. Some further reduction of heating but also cooling demand will be possible when internal air exchange between distinguished thermal zones is considered. Total amount of the useful solar gains from well designed indirect system (windows) is very close to the gains attainable from large indirect system (collecting and accumulating wall). But a major advantage of the indirect system consists in significantly reduced overheating risk in winter and summer. Unfortunately, comparison of the direct solar system and collecting wall, based on combined energy use and investment costs criterion, indicates application of rationally designed passive direct systems.

Keywords: *low energy building, passive solar use, building simulation*

1. Introduction

The requirements imposed in recent years on buildings and their elements have been changing rapidly. On one hand it was a result of an intense worldwide pressure on energy saving, on the other hand it was connected with growing user expectations regarding thermal comfort conditions within the building space. Although, various aspects of low energy building have been present in Polish research and publications for many years, it would be difficult now to find explicit and reliable designing rules useful for practitioners.

1.1. Thermal balance of a low energy building

Due to increased thermal resistance of the external building shell and significant reduction of the ventilation losses, the relations between the major factors of energy balance of the modern buildings are now completely different than they were before. The averaged energy balance structure of the of 15 International Energy Agency experimental low energy buildings is shown in Figure 1 [1]. Although technical design and details of those buildings were different and some of them were located in radically different climatic conditions, important general observations may be formulated:

- solar energy is a dominant part of the balance,
- significant contribution to the balance of internal gains and heat recovery,
- reduced importance of conventional heating.

For example, in case of a German building, that was located in climatic conditions similar to Polish, conventional heating covered 25% of the total energy demand while passively gained solar energy share was 43% [1]. In case of the very well insulated Norwegian row house, located in the most disadvantageous climate (above 60°N), heating system covered only 11% of the total demand while heat recovery 56%, internal gains 15% and sun 10%. Average structure of the energy balance and given examples show quite well an importance of the gains, that were of marginal significance before and also indicate the main directions of a further development.

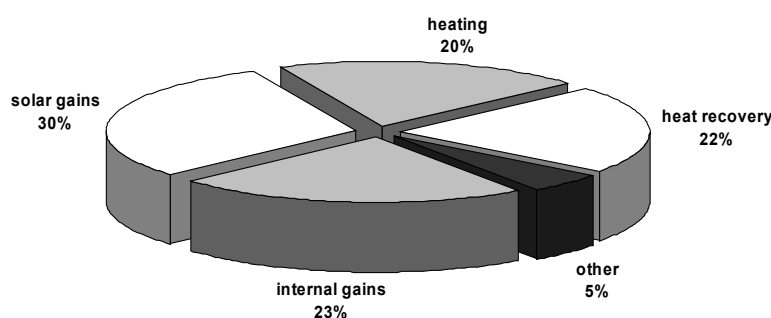


Fig. 1. Heat balance structure of the low energy IEA buildings [186]

Due to the major decrease of energy consumption, that is a result of high thermal resistance of building shell and ventilation air heat recovery, it is possible to meet considerable or even dominant portion of the heating demand with solar energy and internal gains.

1.2. Heat gains usability

Intensive solar radiation that enters highly glazed building on a sunny day or large internal gains in public use buildings does not mean that conventional heating demand will be significantly reduced. Unfortunately, a big part of these gains results in unnecessary internal temperature growth and increased heat losses [2]. Large temporary heat gains cause unacceptable space overheating and finally induce intensified ventilation or space cooling. Hence, only a fraction of the accessible thermal gains will be efficiently used to reduce heating demand.

The simplified designing tools do not consider this effect, so expected savings could be in this way overestimated and well insulated buildings would be overheated [3]. High capacity building envelope enables to store excessive internal energy gains or solar radiation for later use and reduce in this way conventional heating demand [4]. Energy storing process can be connected with temperature growth in standard massive materials, phase changing heat in PCM or reversible chemical reaction in TCM. Positive effects of heat accumulation concern not only heating energy savings

but also space protection against overheating and high temperature fluctuations. Those aspects of building use are particularly important for the users and should be thoroughly considered by the designers.

In Polish standard PN-B-02025 [5] concerning heating demand calculation, monthly average value of gain utilization factor η depends only on the ratio of thermal gains and losses (GLR):

$$\eta = 1 - e^{-\frac{1}{GLR}}. \quad (1)$$

Calculated in this way η -factor value is equal to 100% when thermal gains are negligible, for $GLR = 1.0$ it is reduced to 63% and for $GLR = 2.0$ it is only 39%. Because η -factor value does not depend on space thermal capacity, it will be identical in case of lightweight wooden structures and massive concrete or brickwork structures. It may encourage inexperienced designer to increase unlimitedly glazed areas in order to maximize solar fraction, but in fact heating and cooling demand would grow significantly in this situation.

In European standard EN ISO 13790 [6] utilization factor depends not only on GLR but also on envelope thermal capacity expressed by means of time constant τ :

$$\tau = \frac{C}{H}, \quad (2)$$

where:

C – internal heat capacity,

H – heat loss coefficient.

Although improved algorithms better describe thermal characteristic they can not substitute specialized designing procedures or tools that allow undertaking reasonable decisions and optimizing passive solar system in a simple but efficient way. According to Hastings [3] old procedures of building design, developed even twenty years ago, when insulation standards, user expectations and technical measures were completely different than nowadays, are still in use.

According to author's intention, below presented results should be a simple tool for energy aware designer of indirect passive solar system.

2. Collecting and accumulating solar wall

Greenhouse effect, based on the spectrally differentiated radiation transmittance of the glass, is the background of the building solar gains. Energy collecting aspect may clash with the basic living functions of the building space and its thermal comfort. This conclusion especially concerns the passive direct systems (large window areas), in which the users are exposed to large temperature fluctuations and over lighting

conditions [2]. Direct and diffused solar radiation, absorbed by the clothes or human skin may result even in 10 K increase of operative temperature [7].

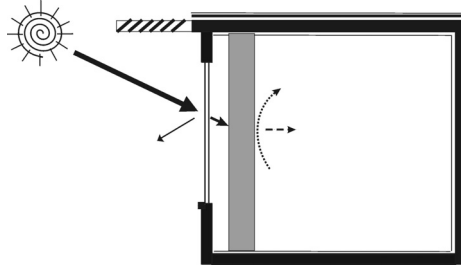


Fig. 2. Scheme of the solar energy gains in indirect passive solar system

A good chance to separate energy and living functions of the building shell appears in indirect passive systems, where absorption and accumulation of the transmitted solar energy takes place close to the wall glazing. A wall of this kind, that becomes a solar thermal collector for a building, will be further shortly called CASW (Collecting and Accumulating Solar Wall). This system is often called Trombe wall, after the first designer [2].

Thermal efficiency of the indirect system is usually lower than that of the direct system [8]. But due to the increased use inconvenience in spaces with the large glazed openings, window area must be limited, while Trombe wall area may be kept pretty large. More efficient solar energy use is achieved when heat from the indirect system is evenly distributed throughout the building space or when the more complicated hybrid systems is introduced.

2.1. Dynamic simulation model

Finite differences method and electric network analogue have been used to create a simple dynamic CASW simulation model. The derivatives used in basic differential heat transfer equation are here replaced with differences of the respective quantities in the defined time steps. Wall materials are replaced with a discrete network consisting of the nodes without thermal capacity (surface nodes) and with thermal capacity (internal nodes). Heat exchange between the nodes takes place via the material or surface resistances. Nodal temperature is a result of the balance of incoming and outgoing heat fluxes, i.e. heat exchange between the neighboring nodes, solar radiation in case of the surface nodes and accumulated heat flux in case of the node with thermal capacity.

Because the initial temperatures are not known usually, so calculations are being repeated long enough to achieve fully repeatable and independent of the initial values cycles.

Temperature of the node i that belongs to one dimensional network and at the moment $p + 1$ may be derived from general Equation [7]:

$$T_{i,p+1} = \frac{\Delta t}{C_i} \cdot \left(q_i + \sum_j \frac{T_{j,p} - T_{i,p}}{R_{i,j}} \right) + T_{i,p}, \quad (3)$$

where:

Δt – time step,

C_i – i -node thermal capacity, equal to the product of density, specific heat and volume,

q_i – heat flux density (e.g. solar radiation),

T_{jp} – j -node temperature at the moment p , node j is in thermal contact with node i ,

R_{ij} – thermal resistance between nodes i and j ,

Convergent solution in explicit computational diagram will be found when time step meets the following condition [9]:

$$\Delta t \leq \min \left[C_i \cdot \left(\sum_j \frac{1}{R_{i,j}} \right)^{-1} \right]. \quad (4)$$

Physical sense of expression in parenthesis corresponds with the time constant of capacity C_i .

2.2. Computational wall diagram

The analyzed wall has been divided into four layers: two thin layers at the edges and two thick internal layers of the same thickness. It was assumed that glazing has no thermal capacity but only thermal resistance. There is a closed air gap between glazing and accumulating wall. Internal air temperature is being kept at the same level, external environment conditions (ambient air temperature and solar radiation) are combined in equivalent solar temperature T_{eq} . Momentary equivalent solar temperature value is calculated as the sum of ambient air temperature harmonic function and positive values of solar radiation harmonic function. The values of the glazing solar transmission coefficient, insulation and airspace thermal resistances and solar radiation absorption are constant.

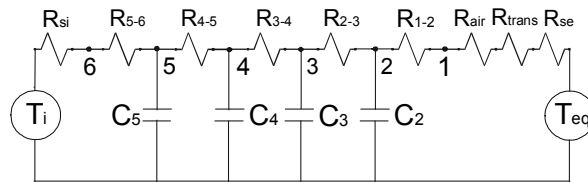


Fig. 3. The simulation diagram of the wall [7]

$$R_{e-1} = R_{se} + R_{trans} + R_{air}, \quad (5)$$

where:

- R_{se} – external surface resistance,
- R_{trans} – glazing thermal resistance,
- R_{air} – airspace thermal resistance.

$$R_{e-2} = R_{e-1} + R_{1-2},$$

$$R_{i-5} = R_{5-6} + R_{si},$$

where:

- R_{si} – internal surface resistance,
- R_{i-j} – thermal resistance between nodes i and j , equal to quotient of the material thickness between nodes i and j and its thermal conductivity.

Nodal temperatures are determined by the following Equations [7]:

$$T_{2,i+1} = \frac{\Delta t}{C_2} \left(\frac{T_{eq}(i \cdot \Delta t) - T_{2,i}}{R_{e-2}} + \frac{T_{3,i} - T_{2,i}}{R_{2-3}} \right) + T_{2,i},$$

$$T_{3,i+1} = \frac{\Delta t}{C_3} \left(\frac{T_{2,i} - T_{3,i}}{R_{2-3}} + \frac{T_{4,i} - T_{3,i}}{R_{3-4}} \right) + T_{3,i},$$

$$T_{4,i+1} = \frac{\Delta t}{C_4} \left(\frac{T_{3,i} - T_{4,i}}{R_{3-4}} + \frac{T_{5,i} - T_{4,i}}{R_{4-5}} \right) + T_{4,i},$$

$$T_{5,i+1} = \frac{\Delta t}{C_5} \left(\frac{T_{4,i} - T_{5,i}}{R_{4-5}} + \frac{T_i - T_{5,i}}{R_{i-5}} \right) + T_{5,i}, \quad (6)$$

$$T_{6,i} = T_i + R_i \left(\frac{T_{5,i} - T_i}{R_{i-5}} \right),$$

$$T_{1,i} = T_{2,i} + R_{1-2} \left(\frac{T_{eq}(i \cdot \Delta t) - T_{2,i}}{R_{e-2}} \right).$$

Simulated Trombe wall consists of:

- double standard glass with solar transmission coefficient equal to 0.710,
- concrete accumulating mass 23.5 cm thick; concrete density 2400 kg/m³, specific heat 1000 J/(kgK), thermal conductivity 2.0 W/(mK), solar absorption coefficient 0.95.

Concrete accumulating mass was divided in two surface layers, each 3 cm thick and two internal layers, each 8.75 cm thick. It was proved that simulation results are not very sensitive to wall division. Modification of the edge layer thickness within the range of 1 cm to 8 cm and constant total wall thickness did not result in any significant heat balance change.

The smallest time constant of the single layer capacity is 1746 s, while time step used in simulations is ca. 3 times shorter and equal to 600 s.

Ambient air temperature is a sinus function with mean temperature $-3\text{ }^{\circ}\text{C}$ and oscillation amplitude $6\text{ }^{\circ}\text{C}$, solar radiation intensity is also a sinus function with mean value 0 W/m^2 and amplitude 550 W/m^2 . Internal air temperature is constant and equal to $+20\text{ }^{\circ}\text{C}$.

Temperature distribution during the sunny winter day within the CAW section with standard double glazing is shown in Figure 4. Presented data were preceded by the 5 day simulation period to achieve fully repeatable results.

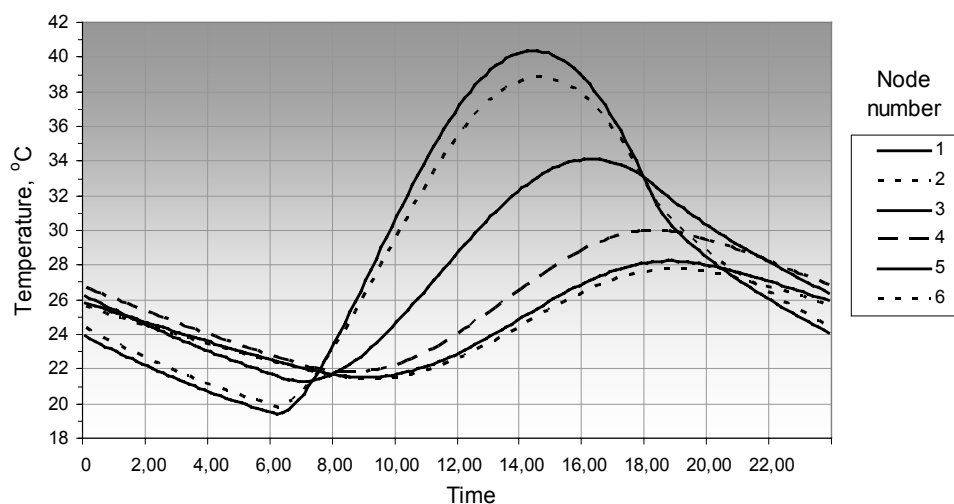


Fig. 4. Temperature distribution within the wall section during the sunny winter day, standard double glazing

External equivalent temperature wave (node 1) is gradually damped, smoothed out and shifted within the concrete wall. Internal surface temperature curve is fully sinusoidal.

2.3. Glazing with improved thermal resistance

Former research works proved that standard glass with low thermal resistance is not suitable for the low energy systems. Glazing systems with enhanced insulating features were used in further research [10]:

- “LE” – double glazing with one low emissivity coating and xenon, U value equal to $1.082 \text{ W}/(\text{m}^2\text{K})$ and total solar transmittance 0.595,
- “LE+” – double glazing with two low emissivity coatings and xenon, U value equal to $0.915 \text{ W}/(\text{m}^2\text{K})$ and solar transmittance 0.516,
- “Therm” – triple glazing with double LE coating and krypton, U value equal to $0.627 \text{ W}/(\text{m}^2\text{K})$ and solar transmittance is 0.472.

Temperature fluctuations of the internal surface of the storage wall have been shown in Figure 5 for three types of glazing and two weather cases: sunny and cloudy winter day.

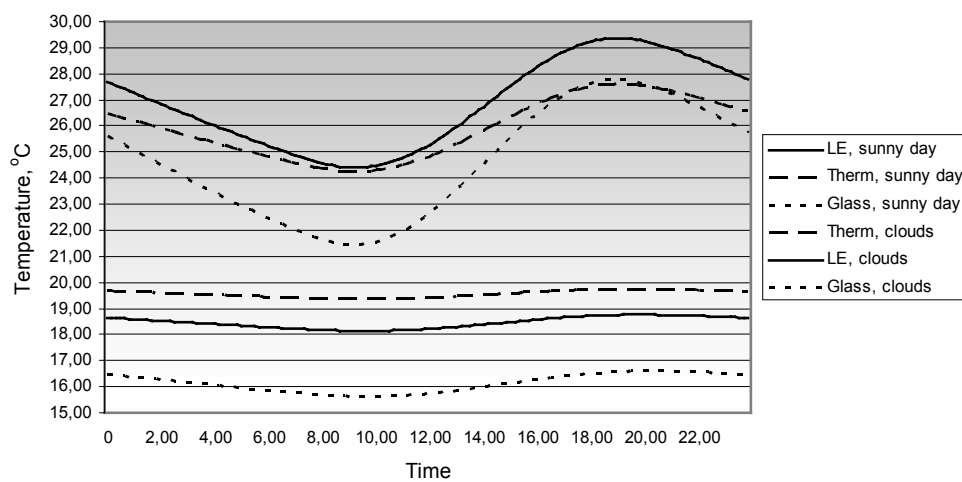


Fig. 5. Internal surface temperature during the sunny and cloudy winter day

Solar intensity amplitude on a sunny day, $550 \text{ W}/\text{m}^2$, is ten times bigger than that on a cloudy day. Due to the low insulating capability of the standard glazing, wall surface temperature is lower than in the other cases, in spite of high solar transmittance of “Glass” panes. “LE” glazing, with higher than “Therm” solar transmittance, enables to achieve better results on a sunny day, but on a cloudy day triple glazing outperforms the others.

To facilitate further comparisons it was assumed that wall performance will be described by the total surface heat flux balance for a sunny and cloudy day, Figure 6. In case of “LE” and “Therm” glazing heat balance difference was merely 3 %. It means that those two glazing systems are practically equivalent to each other in sense of energy saving but different in sense of investment cost.

During the highly advantageous sunny day conditions, in spite of the low ambient temperatures, heat balance is positive, i.e. gains are bigger than losses, for all investigated glazing systems. In these conditions CASW is a source of the net heat gains for a space. On a cloudy day heat balance is in every case negative, but distinctly diverse according to glazing insulating characteristic.

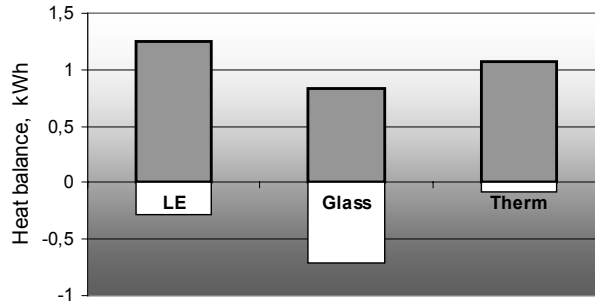


Fig. 6. Internal surface heat balance for a sunny (grey bar) and cloudy (white bar) day

Another, commonly used way of description of the resultant thermal performance of the wall is so called equivalent heat transfer coefficient U_{eq} . In the same way as above heat balance, it combines in one number heat gains and losses. Negative U_{eq} value responds to prevailing gains. Sunny day U_{eq} values for collecting and accumulating wall have been shown in Figure 7. The most beneficial sunny day results could be achieved in case of the wall with “LE” glazing (not “Therm”), as it was also shown before in Figure 6.

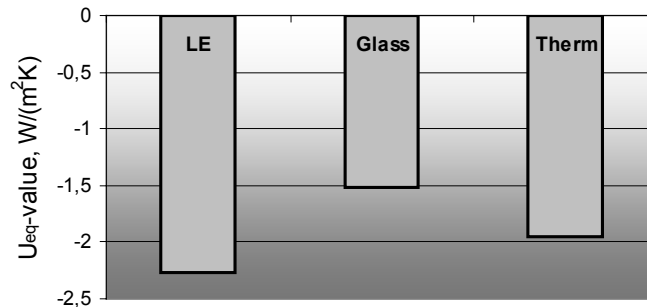


Fig. 7. Equivalent sunny day U -value

3. Long term simulation in EnergyPlus

The simple simulation model that was described in former section allowed to analyze only energy performance of a separate wall fraction in the selected boundary conditions. However the most important information for a user or designer concern usable heat gains in a whole space or even building, during the whole heating season and in real weather conditions.

One of the largest and newest simulation programs nowadays, is an American program called EnergyPlus. It was released by the American Department of Energy, its agencies and other partnering institutions, it enables dynamic simulation of a whole building and its installations [11, 12].

A geometrical outline of the portion of the building that was simulated in Energy Plus is shown in Figure 8.

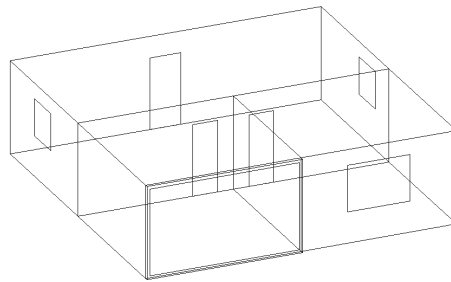


Fig. 8. Collecting and accumulating wall in south-west zone of the simulated building

It may be a storey of a single-family building or, after slight modifications a repeatable unit of a multi-storey residential or office building. Although the dimensions of the entire floor area of the unit are 10 by 10 by 3 m, the main object of the simulation reported in this paper is the unit's south-west part only (modeled as a separate thermal zone), with horizontal dimensions 5 by 5 m and a height of 3 m. Thermal insulation thickness of external walls is 20 cm and roof 25 cm. Minimum internal air temperature during the heating season is constant and equal to +20 °C. When air temperature tends to exceed +25 °C cooling system will be switched on. Ventilation rate is kept at the fixed level of 0.6 h^{-1} with seasonal average heat recovery efficiency equal to 50%. Index E , equal to ratio of the seasonal heat demand and floor area is a measure of heating demand and corresponding index EC is a unit measure of seasonal cooling demand.

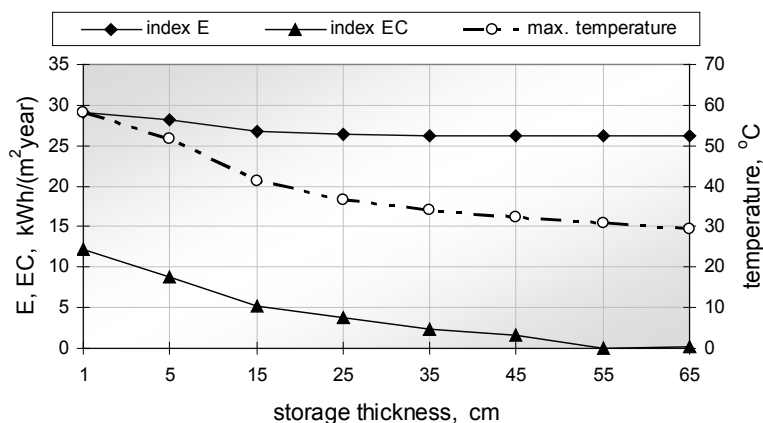


Fig. 9. Index E , EC and maximum temperature of internal CAW surface vs. the concrete storage thickness, "LE" glazing system

Relationship between indexes E and EC and concrete storage thickness has been shown in Figure 9. The third dashed line in Figure 9 is maximum temperature of the accumulator internal surface (right vertical axis). A 25 cm thick concrete storage is practically sufficient to minimize seasonal heating demand of the analyzed space. Further increase of the concrete thickness would only reduce space overheating (EC index) and maximum temperature of the surface.

Total heating demand reduction due to massive concrete storage is not very significant, ca. 10% of initial value. Essential importance of accumulator thermal capacity consists in distribution of the solar gain flux beyond sunshine period and maximum temperature decrease.

Further results of CASW modifications are collected in Table.

Table. Influence of glazing system features on CAW heat gains

Glazing	Maximum temperature of concrete external surface	Maximum temperature of concrete internal surface	Seasonal heating index E	Average heating power	Seasonal cooling index EC
	°C	°C	kWh/(m ² year)	W	kWh/(m ² year)
Glass	65.59	34.76	41.01	176	2.68
LE	60.51	34.14	26.26	113	2.48
LE+	55.16	32.65	27.07	116	1.39
Therm	56.73	33.61	19.46	83	2.86

Although increased thermal resistance of the glazing is usually combined with decreasing solar radiation transmittance, seasonal heating index is significantly reduced. Exchange of standard glazing Glass for three panes Therm glazing results in 53% reduction of the space heating demand. In case of commonly used nowadays glazing “LE” reduction is 36% of the initial value and in case of “LE+” 34%. The best protection against overheating may be achieved by means of “LE+” glazing (reduced solar transmittance due to double “LE” coating). Considering combined criterion of energy performance (heating + cooling), the most advantageous is “Therm” glazing, followed by “LE+” and “LE”. Because in simulation model neither solar shading nor increased ventilation and internal air mixing between zones have been introduced as protection against overheating, with those measures it will be possible to avoid completely overheating shown in last column of Table.

Thermal efficiency is an important parameter of the passive solar system. Sound information regarding system's efficiency would allow even inexperienced designer to evaluate heat balance of the designed space without detailed simulation. Thermal efficiency of a collecting and accumulating wall was defined in a following way:

$$\eta = \frac{Q_{loss} - Q_{heat}}{J_{vert}}, \quad (7)$$

where:

Q_{loss} – total heat losses,

Q_{heat} – conventional heating demand of the space (overheating excluded),

J_{vert} – solar radiation intensity on vertical south-oriented surface.

The efficiency lines of the direct passive systems (windows) and indirect passive system (CASW) have been presented in Figure 10. Thermal efficiency η is shown as a function of the ratio of solar intensity J_{abs} and temperature difference T_i and T_e . Efficiency values were calculated in monthly steps and finally correlated. For the all analyzed cases linear correlation was very strong ($R^2 > 0.91$).

It may be easily observed, that solar gain use for space heating is distinctly differentiated throughout the year. In transition periods, with relatively high ambient temperatures and intense solar radiation, system's efficiency is usually low. On the other hand, low supply of solar radiation is usually connected with high system's efficiency. Because of this variation designing calculations should be repeated on a monthly basis [4].

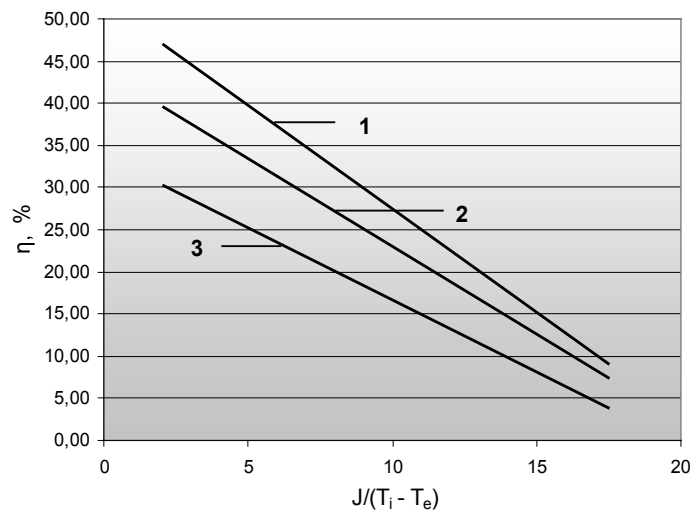


Fig. 10. Thermal efficiency vs. solar intensity and temperature difference ratio, 1: 6 m² window with “LE” glazing and massive building shell, 2: 6 m² window with “LE” glazing and lightweight building shell, 3: collecting and accumulating wall with “LE” glazing

Data presented in Figure 10 confirm that direct system thermal efficiency is higher than in case of indirect one. Discrepancy between lines 1 and 3 is particularly big in conditions of low solar radiation supply. Lines 1 and 2 show also influence of building shell thermal capacity on direct system efficiency.

Efficiency lines shown in Figure 10 may be used as a simple but very convenient designing tool for passive solar systems.

4. An example of practical modification of the indirect passive system

Passive solar systems are often modified in practical implementation because of thermal, technical or esthetic reasons. Introduced modifications may result in a hybrid system that is a combination of the features and advantages of the direct and indirect systems.

In world literature it is easy to find for example a rough description of the system in which continuous brickwork storage wall was substituted with water columns or horizontal water tanks with solar gaps between them [13]. In the other examples diode water tanks or hybrid solutions with forced air flow inside of the brickwork accumulator were used [14]. But detailed technical reports covering system specification or energy performance are usually not available.

An example of the simple indirect system modification is shown in Figure 11.



Fig. 11. Hybrid version of the modified CASW, external view on the left side, internal view on the right side

The narrow vertical element, that is a fireplace chimney shaft, was located closely to the large south window as in a typical indirect system. But the 35 cm airspace between the standard double glazing and the brickwork accumulator is fully opened to the attached room. Brickwork surface is painted dark green to enhance absorption of the solar radiation.

To investigate and illustrate heat accumulation process in the brickwork shaft, a short monitoring of the surface temperature and heat flux has been conducted.

Brickwork surface temperature and heat flux values during the 24 h sunny period are shown in Figure 12.

Surface temperature stratification at three points may be easily noticed during the early hours, when the temperatures are heading toward daily minimum, Figure 12a.

During the next few sunshine hours all the temperatures are practically equal until partial wall shading caused by the external structural elements takes place. During the sunny day surface temperatures are higher than internal air temperature but shortly after the sunset they fall down below air temperature due to the intensive long wave radiation exchange with standard glazing. As expected, accumulator location close to the poorly insulated glazing surface is connected with increased heat losses, comparing with heat accumulation in internal building shell.

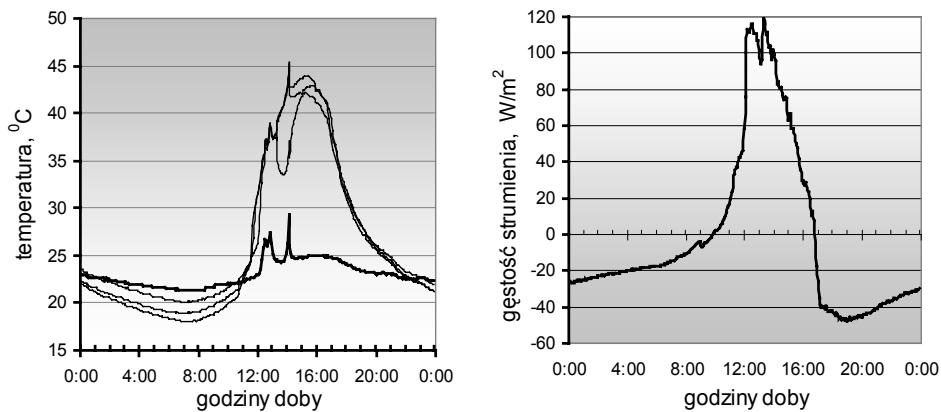


Fig. 12. a) internal air and brickwork accumulator surface temperatures, b) heat flux density

Time shift of the heat flux and temperature waves, connected with the brickwork surface thermal admittance, is equal to 2.5 h and matches the calculation results for 14 cm wall (12 cm brick and 2 cm plaster) at harmonic boundary conditions well [15].

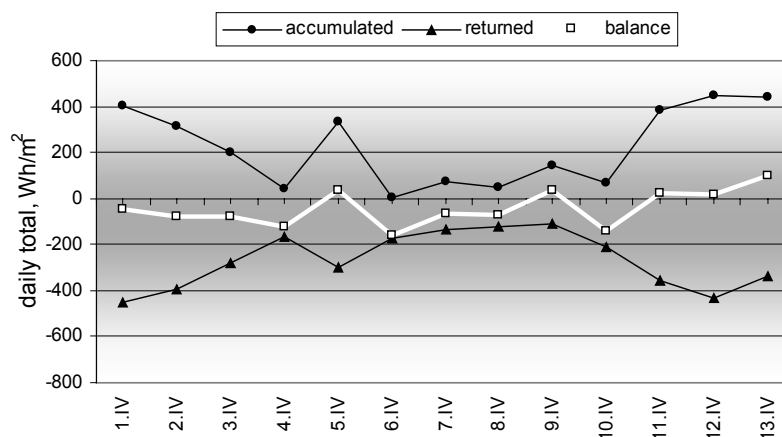


Fig. 13 Density of the heat flux accumulated, returned and daily total, measured on the external surface of a brickwork

Thermal capacity of the brickwork accumulator exposed to the 24 h harmonic oscillations (compatible with Balcomb's dhc value [4]) was calculated as a ratio of measured flux density and daily temperature amplitude. Calculated dynamic capacity value 55.47 kJ/(m²K) was close to the number given for brickwork walls by Kossecka [16].

There is no full symmetry of the flux density accumulated and released from the brickwork storage surface, Figure 13. Thermal balance of the whole monitoring period was negative, i.e. accumulator heat losses were bigger than the absorbed solar radiation.

Short time monitoring data does not allow to answer the important questions regarding the system's long-range results and usefulness. Considering the manner of operation, this kind of design may be treated as a transition version between internal storage, fully enclosed in building space and typical CASW system with air gap separated from the building interior.

5. Summary

5.1. Energy gains

The thickness of the accumulating wall and its thermal capacity affects not only solar heating fraction but also a large extent protection of the space against overheating. On the grounds of conducted simulation it may be determined that 35 cm is a rational maximum concrete storage thickness.

Since standard glass use without selective coating is not reasonable here, highly insulating glazing systems are advised. Glazing thermal resistance has a significant positive influence on space heating demand. Because higher thermal resistance of a glazing is usually connected with decreased solar radiation transmittance, so overheating load is practically not rising. Two-chamber and triple-pane glazing Therm would reduce heating demand of adjacent space by 58% comparing to opaque well insulated wall and by 53% comparing to CASW with standard glazing system. In the whole building scale heating demand reduction may reach 14%. Further reduction of heating but also cooling demand will be possible when internal air exchange between distinguished thermal zones is considered.

Total amount of the useful solar gains from a well designed indirect system (windows) is very close to the gains attainable from a large indirect system (collecting and accumulating wall). The major advantage of the indirect system consists in significantly reduced overheating risk in winter and summer. This statement concerns systems with and without external shading elements.

5.2. Economic aspects of CASW use

Analysis presented above allows to compare the solar systems on energy basis and introduce thermal evaluation of the detailed solutions. But in fact potential investors

are concerned not only in energy performance characteristic but mostly in economic aspects of their investments.

Indirect system in form of a collecting and accumulating solar wall, which is composed of large area glazing with thick and heavy storage, is doubtlessly much more expensive than regular window with 50% smaller area. Extra investment cost would be connected not only with the cost of the massive wall construction but also with the floor area covered by the storage [17]. There are no fully convincing reasons to justify high extra costs with small energy savings and improved protection against overheating. Payback period of this kind of investment would be higher than 20 years and not encouraging for a potential user.

Combined criterion comparison of direct solar system and CASW, regarding energy use and investment costs, indicates application of rationally designed direct system which would minimize space heating demand and ensure thermal comfort in summer.

Nevertheless, collecting and accumulating solar wall can be an important alternative for modern high quality buildings with big glazing area. Well designed wall offers energy efficiency and high standard thermal comfort, very important in public, commercial or exhibition buildings.

References

- [1] *Solar Low Energy Houses of IEA Task 13*, Solar Heating & Cooling Programme IEA, edited by Robert Hastings, James & James, London, 1995.
- [2] Chwieduk D.: *Low energy building-renewable energy* (in Polish), General Building, part 2, Building Physics, edited by prof. Piotr Klemm, Arkady, Warsaw, 2005.
- [3] Hastings S.R.: *Active and Passive Solar Systems in Very Low Energy Housing*, IEA SHC Task 28: ECBCS 38: Sustainable Solar Housing, Copenhagen, 2000.
- [4] Balcomb J.D., Jones R.W., McFarland R.D., Wray W.O.: *Passive Solar Heating Analysis - A Design Manual*, ASHRAE 1984.
- [5] Polish standard PN-B-02025:2001 *Seasonal heating demand calculation of the residential and public use buildings* (in Polish).
- [6] European standard EN ISO 13790:2006 *Thermal performance of buildings – Calculation of energy use for space heating*.
- [7] Athienitis A.K., Santamouris M.: *Thermal Analysis and Design of Passive Solar Buildings*, James & James Ltd., 2002.
- [8] Laskowski L.: *Passive solar buildings, functionality and effectiveness* (in Polish), Studies on engineering IPPT PAN, No. 34, Warsaw, 1993.
- [9] Incropera F.P., De Witt D.P.: *Fundamentals of Heat and Mass Transfer*, V-th edition, John Wiley & Sons, 2002.
- [10] Kisilewicz T.: *Computer Simulation in Solar Architecture Design*, Architectural Engineering and Design Management, Vol. 3, 2007, pp. 106–123.
- [11] Crawley D.B., Lawrie L.K., Winkelmann F.C. et al.: *Energy Plus: creating a new-generation building energy simulation program*, Energy and Buildings, 33/4, 2001.

- [12] Kisilewicz T.: *Influence of the dynamic features of the building shell on heating energy demand and thermal comfort* (in Polish), Technical Review of the Cracow University of Technology, s. B, No. 14-B/2004.
- [13] Mazria E.: *The Passive Solar Energy Book*, Rodale Press Emaus, 1979.
- [14] Shurcliff W.A.: *New Inventions in Low Cost Solar Heating*, 100 Daring Schemes Tried and Untried, Brick House Publ. Comp., Andover MA, 1979.
- [15] Kossecka E.: *Chosen aspects of the building walls thermal dynamics* (in Polish), Studies on engineering IPPT PAN, No. 45, Warsaw, 1998.
- [16] Kossecka E.: *Influence of the building wall structure on its periodic thermal capacity* (in Polish), Proceedings of the International Conference Energodom, Kraków, 2006.
- [17] Kisilewicz T.: *Energetic and usable aspects of the collector wall* (in Polish), *Energia i Budynek*, Vol. 9, 2007, pp. 63–70.

Przeszklona ściana jako kolektor energii słonecznej dla budynku

Mniej uciążliwym dla użytkowników niż okno, źródłem zysków słonecznych jest masywna przegroda nieprzezroczysta, od zewnątrz osłonięta zestawem szyb, nazywana przegrodą kolektorowo-akumulacyjną. W artykule sprawdzano jej przydatność w naszym klimacie i poszukiwano rozwiązań gwarantujących najlepsze rezultaty energetyczne. W skrótowny jedynie sposób przedstawiono wyniki analiz, m.in. wykresy, pozwalające na określenie sprawności cieplnej tej przegrody, a w efekcie udziału energii słonecznej w pokrywaniu zapotrzebowania na ogrzewanie. Wykresy tego typu mogą stanowić prostą pomoc we wstępnych analizach projektowych.

Uzyskane wyniki obliczeń symulacyjnych przekreślają praktycznie sens stosowania przegrody kolektorowo-akumulacyjnej ze zwykłym oszkleniem i bez izolacji termicznej. Istotną poprawę właściwości tej przegrody można uzyskać dopiero po zastosowaniu izolacyjnych zestawów szybowych.

Biorąc pod uwagę łącznie ogrzewanie i przegrzewanie wnętrza, najbardziej korzystną kombinację właściwości mają zestawy szyb o najwyższej izolacyjności termicznej. Wykazane w obliczeniach przy bardzo niekorzystnych założeniach, ograniczone przegrzewanie wnętrza w obiektach prawidłowo zaprojektowanych, może być w praktyce usunięte poprzez intensywniejszą wentylację lub wewnętrzną wymianę ciepła w budynku.

Główną zaletą przegród kolektorowo-akumulacyjnych jest ochrona warunków termicznych we wnętrzu, poprzez wygładzanie wahań pozyskiwanego strumienia energii słonecznej. Jednak związane z tym oszczędności eksploatacyjne nie uzasadniają w przekonywujący sposób znacznych różnic inwestycyjnych. Porównanie PKA z oknami, w oparciu o łączne kryteria energetyczne i inwestycyjne, sugeruje, więc raczej stosowanie okien o precyzyjnie dobranej i mniejszej niż przegroda kolektorowa powierzchni, gwarantującej niskie zapotrzebowanie na ogrzewanie i poprawne warunki termiczne w okresie lata. Przegroda kolektorowo-akumulacyjna może stanowić natomiast uzupełnienie czy nawet alternatywę dla obficie przeszklonych wnętrz, zwłaszcza w wysokiej jakości budynkach użyteczności publicznej, handlowych, wystawienniczych itp.



Spinning and flow forming hard-to-deform metal alloys

A. PLEWIŃSKI, T. DRENGER

Metal Forming Institute, Jana Pawła II 14, 61-139 Poznań, Poland

The increasing requirements of industry concerning products of hard-to-deform materials result in growing interest in the technologies of spinning and flow forming. Moreover, the tendency to manufacture short series makes those technologies more and more attractive in the case of axisymmetrical products. The paper presents works involved in the preparation of manufacture of new axisymmetrical products of hard-to-deform metal alloys. Those products often have complex shapes, difficult to obtain by the traditional methods of stamping. The elaboration of the new technologies has been preceded by material and technological investigation.

Keywords: *spinning, flow forming, hard-to-deform metal alloys*

1. Introduction

Many industrial branches increase their interest in economical manufacturing of short and medium series of products. Furthermore, the tendency to reduce the weight of products brings greater interest in the application of materials with higher strength or lower specific gravity. Those materials generally reveal higher deformation resistance. In the case of axisymmetrical products, incremental technologies of rotary forming meet the requirements of cost-effective production and the possibility to form hard-to-deform materials.

2. Flow forming technologies

Incremental rotary forming technologies are, first of all, spinning and flow forming.

Spinning means forming a sheet metal disk on a template in one or more passes of the forming roll. This is effected without intended thinning of the wall. Spinning is a very effective method of forming complex shape axisymmetrical products [1].

Flow forming means shaping a product of sheet metal, tube or drawpiece in one or more passes of the forming roll or rolls. The magnitude of wall thinning depends on the properties of the input material and the number of passes.

Flow forming is an effective method of manufacturing short series of precision tubular products of hard-to-deform materials, as well as short series of toothed products and profiled disks [2, 3].

Due to the incremental way of forming, the forming forces necessary in spinning or flow forming are much lower than those necessary in stamping, either with or without wall

thinning. This is due to small, relocating material plastification area and therefore lower friction forces occurring in the process [4]. This results in easier material flow and, consequently, the possibility to obtain larger deformations than in stamping. A consequence of this is the possibility to form hard-to-deform materials by these technologies. Some materials have to be formed at higher temperatures [5]. An interesting solution of local material heating can be the use of a laser beam [6].

One of the requirements present day technologies must meet is short time to start a product. The time can be shortened with the use of process simulation by numerical methods. This increases the technological certainty and eliminates the trial and error methods. However, incremental technologies are much more difficult to simulate due to the complicated process of shaping. Much better results have been obtained in flow forming than in spinning, but full simulation of the rotary forming process has not been solved yet [7, 8].

The Metal Forming Institute deals with spinning and flow forming as well as with the design of machines for those technologies. The machines are characterized by high installed powers and are designed so that adequate stiffness of the template-tool-machine system is assured during the forming process. Some products made by spinning and flow forming as well as a diagram of elongating flow forming can be seen (Figures 1 and 2). In the further part, investigation of flow forming technology for three hard-to-deform materials have been described.



Fig. 1. Examples of spun and flow formed products

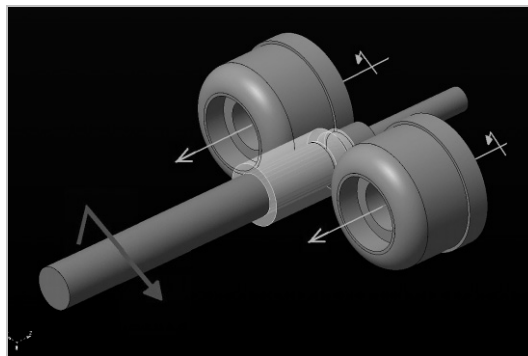


Fig. 2. A diagram of elongating flow forming

3. Examples of flow forming technology investigation for hard-to-deform materials

3.1. Investigation of flow forming of an aluminium alloy [9]

The investigation objective was to elaborate the technology of manufacturing an elongated product (Figure 3) of an aluminium alloy with complex strength properties.

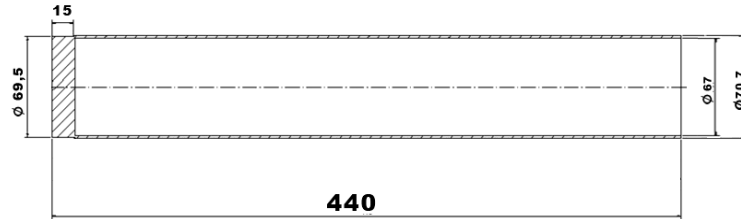


Fig. 3. A cylinder of aluminium alloy

The alloy, close to the 7075 alloy with the chemical composition shown in Table 1, has the mechanical properties shown in Table 2.

Table 1. Chemical composition and density of the alloy

Alloy	Content of elements in %									
	<i>Si</i>	<i>Fe</i>	<i>Cu</i>	<i>Mn</i>	<i>Mg</i>	<i>Cr</i>	<i>Zn</i>	<i>Ti</i>	Other	Density [g/cm ³]
7075	0.5	0.5	1.4–2.0	0.2–0.6	1.8–2.8	0.1–0.25	5.0–7.0	–	≤ 0.15	2.80

Table 2. Mechanical properties of alloy

Material condition	$R_{0.2}$ [MPa]	R_m [MPa]	A_{50} [%]	Hardness HB
As supplied	147	295	14.75	78
Annealed 480 °C, 2h, cooled with the furnace	105	236	16.15	60

Prior to the investigation of the technology, the input material has been investigated, which material was a cast shaft. The positive results of metallographic examination have allowed for further investigation of the material plasticity and the influence of heat treatment on the plasticity and the strength properties.

Further investigation sequence is as follows:

- selection of dimensions of the blank made by turning (Figure 4),
- determination of admissible relative deformation in the individual operations of flow forming after soft annealing.

The influence of deformation on the quality of semi-product in individual operations combination with softening heat treatment has been investigated. The criterion was the lack of surface cracks and the lack of significant grain growth. Maximum deformation in one operation has been determined,

- determination of technological parameters, such as roll rotational speed and feed, kind of cooling and its intensity, in respect of the assumed surface quality. During the tests, the selected parameters were ones for which scaling does not appear on the surface and ones which make it possible to obtain surface roughness of $R_a = 1.6$. The determined parameters were:

- roll rotational speed 500 r.p.m.,
- feed 6 mm/s,
- kind of cooling Rucol Ultracut 370,
- intensity of cooling $0.33 \times 10^{-3} \text{ m}^3/\text{s}$,
- determination of production technology including the final heat treatment.

Heat treatment parameters have been determined, i.e. the heating temperatures and times for softening annealing and the way of cooling for dispersion hardening have been precisely defined. The chosen parameters were:

- heating temperature 480 °C,
- time of heating 2h,
- way of cooling with furnace.

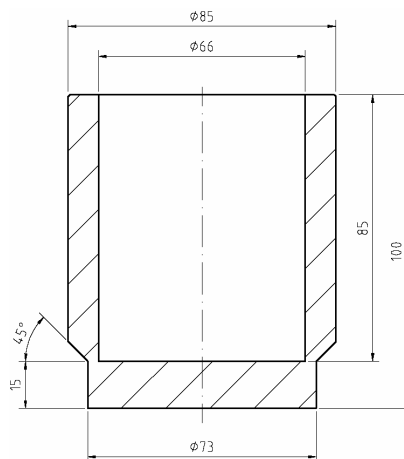


Fig. 4. A blank

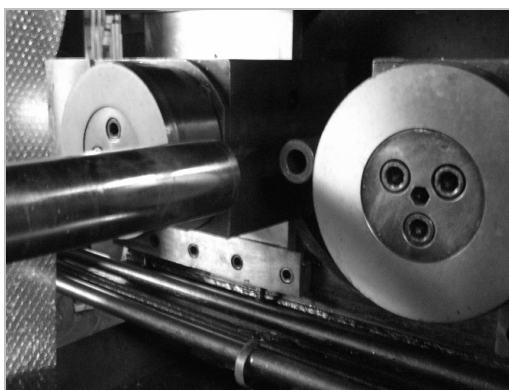


Fig. 5. The investigation stand
– MZH-400 flow forming machine

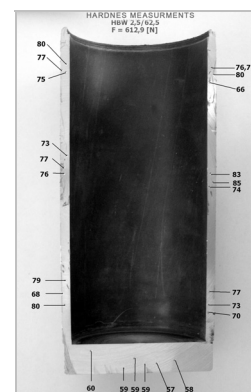


Fig. 6. Hardness measurements
for the relative deformation of 54%

The flow forming investigation has been performed on the flow forming machine shown in Figure 5.

The high strength of the product has been obtained due to hardening after flow forming (Figure 6) and heat treatment (impregnation and ageing).

The product obtained is shown in Figure 7. It has the assumed accuracy, mechanical properties and surface roughness ($R_a < 2.5$).

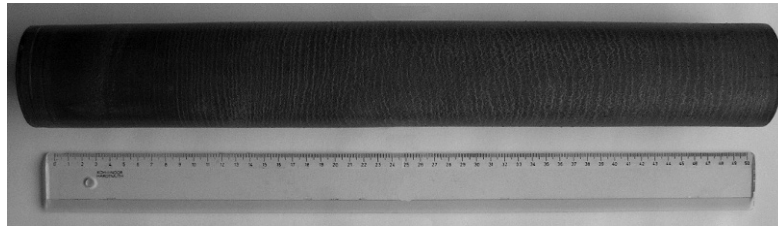


Fig. 7. Final product with the length over 500 mm

3.2. Investigation of spinning of stainless steel

The objective of the investigation was to elaborate a technology of manufacturing centric elements of a stainless steel throttle (Figure 8).

After initial elaboration of the technology for steel drawing sheet, the possibility of spinning of two stainless steel grades, 0H18N9T and 00H17N14M2, have been investigated. The problem of spinning of those material grades is high internal stresses resulting in significant spring back. As a result of the investigation, the 0H18N9 material has been selected, for which the production technology has been elaborated. The number of forming operations and interoperation impregnation has been determined. The bottom part is made in three spinning operations: initial spinning, smoothing spinning and spinning on a split template to reduce the disk diameter. Annealing, so called solution heat treatment at 1050–1100 °C and cooling in air, has been introduced. This heat treatment significantly improves dimensional accuracy of the final product after the operation of smoothing spinning.

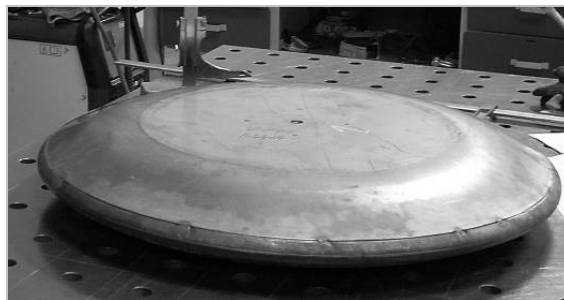


Fig. 8. Elements of a centric disk of a throttle, dia. 600, during the tests

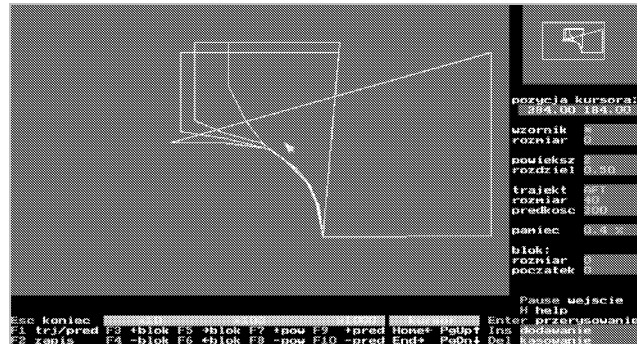


Fig. 9. Spinning path – graphic presentation in the machine co-ordinates

For each operation, optimum roll motion paths have been determined considering the springback and enabling dimension tolerances of the products being made to be closer (Figure 9) [10]. Figure 9 is a graphic presentation of the spinning roll path in the machine co-ordinates in the test stand in the Metal Forming Institute. By the introduction of the additional operation of smoothing with a smaller clearance between the roll and the template, the dimension tolerances of the product have been reduced and its circularity and flatness have been improved.

3.3. Investigation of stamping and flow forming of INCONEL 625 alloy

The purpose of the investigation was to determine the possibilities of the application of metal forming, particularly flow forming to shape products made of nickel super-alloy, INCONEL 625 [11].

The material has the chemical composition presented in Table 3 and its mechanical properties can be found in Table 4.

Table 3.

Component	Ni	Cr	Fe	Co	Mo	Nb + Ta	Ti	Al	C	Mn	Si	P	S
%	61.5	21.53	3.87	0.13	8.94	3.51	0.19	0.10	0.03	0.08	0.10	0.007	0.001

Table 4.

Yield Strength (0.2% offset) $R_{p0.2}$ [MPa]	Ultimate Tensile Strength R_m [MPa]	Elongation 50 mm (2") A_{50} [%]	Hardness [HB]
517	930	49.7	190

The investigation consisted in stamping shallow cylindrical drawpieces followed by elongating flow forming of them with sidewall thinning and elongation of the blanks. Figures 10 and 11 show the test tools for the initial trials of forming the nickel super-alloy.



Fig. 10. A test stamping die

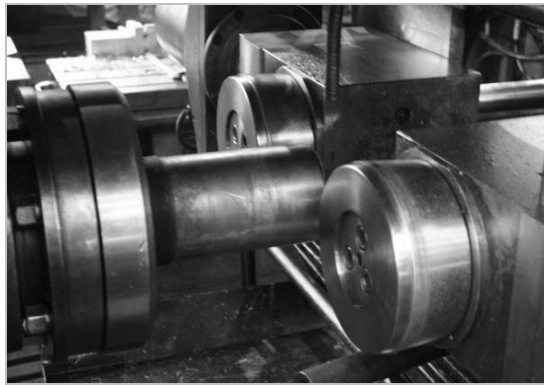


Fig. 11. A flow forming machine with the tools-for elongating flow forming

The trials have shown that the material is quickly strain hardened during deformation, which causes a rapid increase of the forming forces. In addition, it is characterized by significant values of spring back. In spite of that, the alloy can be shaped by the metal forming methods, particularly by flow forming. However, further investigation of plastic forming of the alloy should be carried on, e.g. trials of flow forming with local heating by means of a laser. Figure 12 shows a modernized test stand for spinning and flow forming.

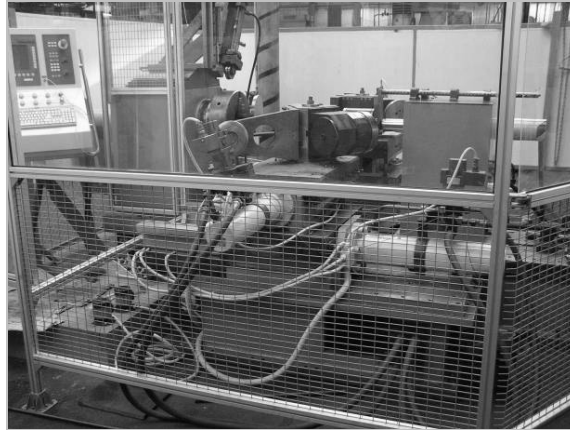


Fig. 12. MZH-500 machine

The machine brings new investigation possibilities, especially for hard-to-deform materials. It has been modernized within the program WKP_1/1.4.3/2/2005/4/123/304/2006 named: *Modern investigation stand for flow forming of sheet metal products*.

Shortly, the machine will be equipped with a diode laser to perform trials of warm and hot spinning and flow forming.

4. Conclusion

The examples presented above show that the flow forming technologies described here significantly extend the possibilities of plastic forming of hard-to-deform materials. Incremental forming, due to smaller friction resistance, makes it possible to obtain larger deformations as compared to the traditional technologies.

A consequence of this is the possibility to form hard-to-deform materials by these technologies. Further investigation should broaden those possibilities and result in larger application of the technologies of spinning and flow forming.

References

- [1] Drenger T., Wiśniewski J., Gądek T.: *Incremental rotary forming of sweet metal products* (in Polish), MM Obróbka Blach wydanie targowe Blech Business, November, 2007, pp. 29–31.
- [2] Lisunec N.L. et al.: *Razrabotka tekhnologii proizvodstva precizionnyhh trub iz trudno-deformiruemykh korrozionno-stoikikh stalej i splavov*, Stal, No. 10, 2005, pp. 79–81.
- [3] Säuberlich T., Specht G.: *Net shape Fertigung von Profilscheiben und Getriebekomponenten*, Umformtechnik, H. 1, 2000, pp. 63–68.
- [4] Herold G., Gorbauch S., Hartwig H.: *Kraft- und Drehmomentbedarf beim Drückwalzen*, Blech Rohre Profile, Jg. 42, H. 11, 1995, pp. 708–712.

-
- [5] Yoshihara S. et al.: *Design improvement of spin forming of magnesium alloy tubes using finite element*, J. Mat. Proc. Technol., Vol. 153–154, 2004, pp. 816–820.
 - [6] Klocke F., Zaboklicki A.: *Innovation in der Umformtechnik: Laserunterstützte Drückverfahren*, Blech Rohre Profile, Jg. 42, H. 5, 1995, pp. 338–343.
 - [7] Xu Y. et al.: *3D rigid-plastic FEM numerical simulation on tube spinning*, J. Mat. Proc. Technol., Vol. 113, 2001, pp. 710–713.
 - [8] Ufer R., Awiszus B.: *Möglichkeiten und Grenzen der Simulation inkrementeller Umformverfahren*, Umformtechnik, H. 2, 2005, pp. 24–27.
 - [9] Gądek T., Sosnowski S., Drenger T. et al.: *Investigation of the process of cold flow forming of hard-to-deform aluminium alloys included in the standard* (in Polish), PN-EN 573-3/AK, Metal Forming, No. 2, 2007, pp. 9–14.
 - [10] Drenger T., Wiśniewski J., Lisowski J.: *Technologies of flow forming of springing choke disks* (in Polish), Metal Forming, No. 2, 2007, pp. 19–23.
 - [11] Drenger T., Wiśniewski J., Sosnowski S.: *Investigation of the process of cold flow forming of hard-to-deform aluminium alloys included in the standard* (in Polish), PN-EN 573-3/AK, Metal Forming, No. 2, 2007, pp. 15–22.

Wyoblanie i zgniatanie obrotowe trudno odkształcalnych stopów metali

Wzrastające wymagania przemysłu dotyczące wyrobów z materiałów trudno odkształcalnych powodują zwiększone zainteresowanie technologiami wyoblania i zgniatania obrotowego. Ponadto tendencja wytwarzania wyrobów w krótkich seriach wpływa na wzrastającą atrakcyjność tych technologii przy produkcji wyrobów osiowosymetrycznych.

Referat przedstawia prace związane z przygotowaniem technologii produkcji nowych osiowosymetrycznych wyrobów z trudno odkształcalnych stopów metali. Wyroby te często mają złożone kształty, trudne do uzyskania tradycyjnymi technologiami tłoczenia. Opracowanie nowych technologii zostało poprzedzone badaniami materiałowymi i technologicznymi.



Rheological properties of alloys near solidus point intended for thixoforming

K.P. SOŁEK, A. ŁUKASZEK-SOŁEK

AGH University of Science and Technology, al. Mickiewicza 30, 30-059 Kraków, Poland

R. KUZIĄK

Institute for Ferrous Metallurgy, ul. Karola Miarki 12, 44-101 Gliwice, Poland

Thixoforming processes are more and more popular in automotive industry. At present, the shaping a lot of components from cast aluminium alloys in the semi-solid state is performed and possibility of application of both wrought aluminium and steel alloys is investigated. The main goal of this work is the analysis of the rheological properties of metal alloys at high temperatures, just below the solidus point, and in the semi-solid state with low liquid phase content. The data obtained from the analysis can form the basis of numerical simulation for designing and optimizing the thixoforming processes. The rheological properties should be known over a wide temperature range so that the simulations could also predict defects such as incomplete die filling. The analysis concerned both aluminium alloys (A356, 7075) and a steel alloy (M2). The paper also discusses development of globular microstructure in partially melted alloys.

Keywords: *thixoforming, globular microstructure, rheological properties, material test, physical modelling*

1. Introduction

The shaping of the material in the thixoforming processes is realized in the solidification temperature range. The combination of the semi-solid state and globular microstructures provides a material with thixotropic properties. Thixoforming processes operate more efficiently at conditions of forming where uniform temperature of the material is assured. However, in real industrial versions, such as thixoforging and thixocasting the uniform distribution of temperature in the formed metal alloys is not fully ensured. One reason of uneven temperature distribution is due to the intensive cooling of the material by the much lower temperature of the tools. The cooling can be intensive enough for the outer temperature of the material being formed to decrease below the solidus point during the dynamic part of the forming process. Note that thixoforming is normally carried out at fraction liquid between 20–50% [1, 2]. Numerical simulations require knowledge of the rheological properties of the alloys being shaped in order to predict both the correct pressure variables of the process and the correct die filling front. The rheological properties should be known over a wide temperature range so that the simulations could also predict defects such as incomplete die filling. This paper presents experiments, based on the compression test, used to measure the rheological properties both in the solidification temperature range and

below solidus temperatures. The experiments were executed in Institute for Ferrous Metallurgy in Gliwice on the Gleeble 3800 simulator using the Hydrowedge unit (Figure 1) [3]. In order to obtain more uniform temperature distribution and avoid oxidation a protective atmosphere was applied. The compression tests on the Gleeble[®] system are possible in semi-solid state approximately up to 20% liquid fraction.

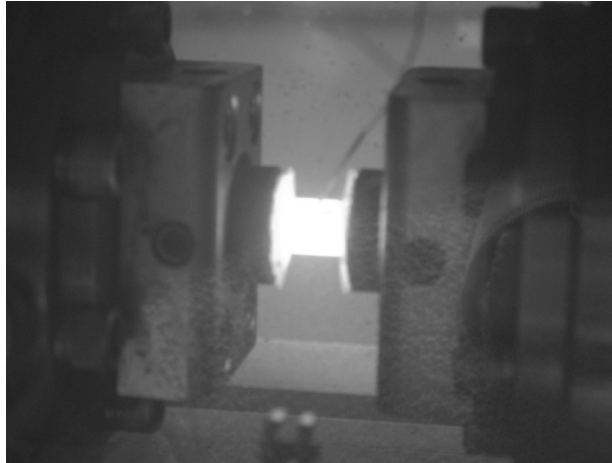


Fig. 1. Sample in the vacuum chamber before the compression test on the Gleeble[®] system during heating

2. Rheological properties of aluminium alloys near solidus point

Rheology of metallic alloys in semi-liquid state is commonly defined by means of flow stress or apparent viscosity in relation to equations of motions, for which the rheology is being established. Nevertheless both these values for such condition are strong functions of temperature, strain velocity, and time (metal in semi-liquid state demonstrates qualities of non-Newton and thixotropic liquids). With such defined approach, effect of strain has secondary significance considering domination of flow mechanisms showing low sensibility to this parameter. Gleeble system usually records stress – strain function during plastometric tests. However, in case of axial symmetric samples upset forging, it is relatively simple to determine relation of tool force and its displacement. Relation of tool forces and displacement can be used for estimation of apparent viscosity model parameters for alloys being analysed. Samples of 10 mm height and 12 mm diameter have been used in upset forging tests. Figure 2 illustrates stress – strain curves for A356 alloy. The relations shown were obtained for strain rate 10 s^{-1} .

The alloy for testing had globular microstructure obtained in process of semi-continuous casting with simultaneous magnetohydrodynamic stirring of solidifying alloy (MHD method) [4]. This method consists in forming of strong rotational electromagnetic field within crystalliser causing intensive mixing, which in effect

prevents development of dendritic microstructure. Two samples were upset forged in temperatures below solidus point (500, 550 °C), while the next two in temperatures above solidus point (560, 565 °C). Lack of strain magnitude influence on stress is observed for temperature 565 °C. This fact proves that considering relatively high content of liquid phase, flow constitutes mechanism of forming. Plot of stress in temperature 560 °C shows sudden magnitude increase, preceding its uniform decreasing. Strain mechanism in the first phase consisted in destroying of solid phase particles crystal skeleton. Material flow prevailed in the final phase. Upset forging tests at temperatures 560 °C and 565 °C were performed with small portion of liquid phase, amounting approx. to 5–10%. Low portion of liquid phase in alloy causes difficulties in process control. Increasing of forming temperature by 5 °C (from 560 to 565 °C) gave 5-times decrease of maximum flow stress (Figure 2). Taking into consideration that temperature difference obtained in die cavity can reach 3–4 °C, thixotropic forming of tested A356 alloy would be, in fact, very difficult in these temperatures.

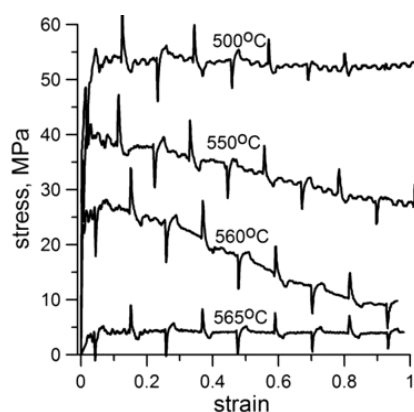


Fig. 2. Stress-strain curves for A356 aluminium alloy at temperatures near solidus point

Next the compression tests were carried out for 7075 aluminium alloy. Also, in this case, the alloy had the globular microstructure, which was obtained using the SIMA (Strain-Induced Melt Activated) method [5]. This method can be relatively easy employed for plastic metal alloys. Also, it can be applied for steels, giving good results [6]. Globular microstructure is formed in the highly strained alloy during partial melting. Starting material for this method is cast alloy of dendritic structure. Such alloy subjects to hot working (in temperature higher than recrystallizing temperature). Finally, strained alloy is partially melted to semi-solid state. Recrystallization process takes place in the material during heating, and when solidus temperature is exceeded, liquid phase penetrates boundary of recrystallized grains, causing fragmentation of solid phase. As a result globular microstructure built of equiaxial, fine grains, is obtained. Experimental works have shown that this size

largely depends on strain when in solid state, and on soaking time in semi-solid state. The advantage of this method is possibility of purchasing of metal alloys that are plastic pre-strained, at very affordable prices.

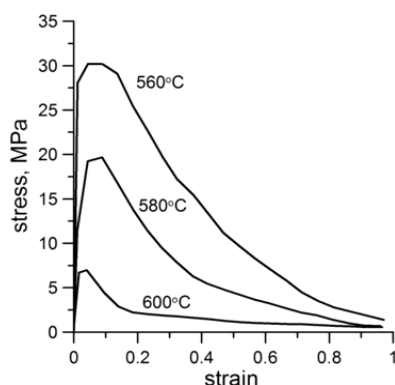


Fig. 3. Stress-strain curves for 7075 aluminium alloy at temperatures near solidus point

Flow stresses recorded for 7075 alloy are shown on Figure 3. All compression tests were performed for semi-solid state, while portion of liquid phase increasing together with temperature caused resistance decrease of solid phase particles skeleton, as well as increase of flow portion in strain mechanism. Upset forging test of 7075 aluminium alloy was performed in temperature range 560–600 °C, which corresponds to theoretically calculated 15–30% portion of liquid phase. At upset forging temperature 560 °C maximum stress reached approx. 30 MPa, while after increase of upset forging temperature up to 600 °C its value decreased down to approx. 7.5 MPa, i.e. 4-times.

3. Rheological properties of steel alloys near solidus point

The analysis of rheological properties of M2 tool steel near solidus point was the next part of the work. Prior to compression tests, a DSC-TGA analysis was carried out to estimate the solidus, liquidus temperatures and transformation reactions which are caused by phase changes. The DSC-TGA heating curve is shown in Figure 4. An analysis was carried out in the Institute of Metallurgy and Materials Science PAS in Kraków. The solidus is estimated at 1230 °C and the liquidus at 1450 °C. The DSC-TGA curve exhibits three major endothermic peaks which are caused by transformation reactions. The first and the second peaks of this curve are associated with the end of the carbides dissolution, while the third is the end of austenite dissolution.

Also, in the case of M2 steel alloy, the globular microstructure was obtained using the SIMA method. The flow stresses recorded for different temperatures are shown in Figure 5. A measurement was carried out for the strain rate of 10 s^{-1} at each temperature. Three tests are carried out for the solid state (1190, 1210, 1225 °C) and three for the semi-solid state (1235, 1245, 1300 °C). For the solid state, one can observe a decrease of

the flow stress for an increase of temperature. The flow stress for 1225 °C is lower by one third. For the semi-solid state, an increase of the liquid fraction under the influence of an increase of temperature causes a decrease of resistance of the solid particles skeleton and an increase of the liquid flow in the deformation mechanism. Compression tests in the semi-solid state for M2 steel alloys were carried out at a temperature range of 1235–1300 °C to be related to the liquid fraction of 5–15%. For a deformation temperature of 1235 °C, the maximal stress amounts to 95 MPa, and after being heated to 1300 °C, its value decreases to a level of about 50 MPa, that is twice.

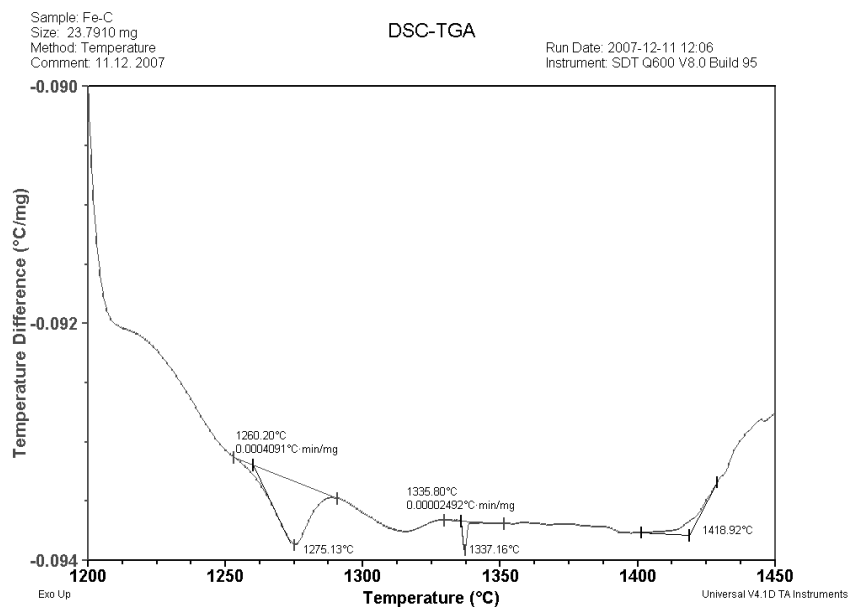


Fig. 4. DSC-TGA heating curve for M2 tool steel

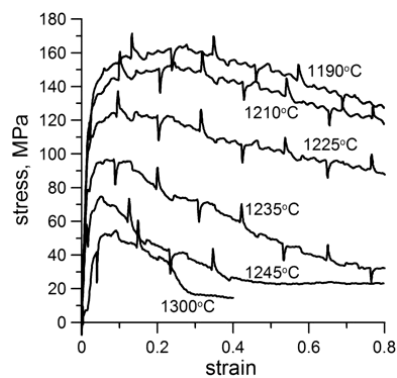


Fig. 5. Stress-strain curves for M2 tool steel alloy at temperatures near solidus point

During the experimental work an influence of the strain rates changes on the flow stresses was investigated. The flow stress is highly sensitive to changes of the strain rate. Therefore, in the solid state, the material shows viscoplastic rheological properties and in the semi-solid state, viscous properties.

4. Microstructure analysis in M2 tool steel after heating to a semi-solid state

Within the confines of this work, an analysis of microstructure evolution in hot forged tool steel after heating to a semi-solid state was carried out. The supplied material was in the form of a hot forged rod of 80 mm in diameter. The heating experiments were carried out using the Hydrowedge unit of the Gleeble[®] system. The geometry of the samples was the same as the geometry used for the compression test (10 mm in diameter, 12 mm in height). The samples were heated in an argon gas environment to reduce oxidation. The heating speed was 5 °C/s. The control thermocouple was welded to the surface in the middle of sample.

The samples were heated to 1250 °C and 1300 °C, and after heating, they were quenched in water to freeze the structures. Figure 6a and 6b show the structures at the above-mentioned temperatures. The structures show solid grains surrounded by traces of the liquid matrix. The liquid fraction includes mostly carbides. One can observe that a higher temperature gives more traces of the liquid fraction both inside solid grains and along their boundaries.

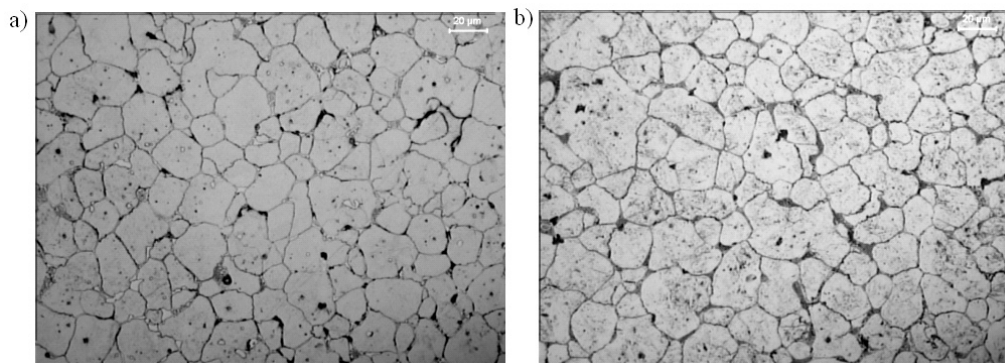


Fig. 6. Optical micrograph of M2 steel at (a) 1250 °C and (b) 1300 °C at zero minute holding

5. Summary

Thixoforming technology is very sensitive to process conditions. It results from the phase change connected with the solidification that proceeds under the influence of the cooling of shaped alloys. The experiments carried out in this work show that a small change of temperature causes a significant change of the flow stress, even a few times. Therefore, owing to the instability of thixoforming processes, problems with their

control can occur. Design and optimization require determination of the ranges of process parameters to avoid defects of products. This is why knowledge of the rheological properties in a wide range of process parameters is very important.

Acknowledgements

Scientific research financed from science financing resources for years 2007–2010, as research project No. COST/17/2007.

References

- [1] Kapranos P., Kirkwood D.H., Sellars C.M.: *Thixoforming high melting point alloys into non-metallic dies*, In: *Proc. 4th International Conference on Semi Solid Processing of Alloys and Composites*, eds.: Kirkwood D.H., Kapranos P., The University of Sheffield, Sheffield, UK, 1996, pp. 306.
- [2] Chayong S., Kapranos P., Atkinson H.V.: *Semi-solid processing of aluminium 7075*, In: *Proc. 6th International Conference on Semi Solid Processing of Alloys and Composites*, eds.: Chiarmetta G.L., Rosso M., Edimet Spa, Brescia, Turin, Italy, 2000, pp. 649.
- [3] www.gleeble.com, Dynamic Systems Inc. (DSI), 2007.
- [4] Garat M., Blais S., Pluchon C., Loué W.R.: *Aluminium semi-solid processing: From the billet to the finished part*, In: *Proc. 5th International Conference on Semi Solid Processing of Alloys and Composites*, eds.: Bhasin A.K., et al., Colorado School of Mines, Golden, Colorado, USA, 1998, pp. XVII.
- [5] Young K.P., Kyonka C.P., Courtois J.A.: *Fine grained metal composition*, US Patent No. 4 415 374, 30 March, 1982.
- [6] Omar M.Z., Palmiere E.J., Howe A.A., Atkinson H.V., Kapranos P.: *Thixoforming of GFM M2 tool steel from the as-annealed condition*, In: *Proc. 8th International Conference on Semi Solid Processing of Alloys and Composites*, eds.: Alexandrou A. et al., Limassol, Cyprus, 2004, CD-ROM.

Własności reologiczne stopów metali formowanych tiksotropowo w temperaturach bliskich punktowi solidus

Procesy formowania tiksotropowego są coraz bardziej popularne w przemyśle motoryzacyjnym. Obecnie kształtuje się w stanie stało-ciekłym dużo części z odlewniczych stopów aluminium, jak również prowadzi się badania nad wdrożeniem formowania tiksotropowego plastycznych stopów aluminium oraz stali. Celem pracy była analiza własności reologicznych stopów metali w temperaturach bliskich punktowi solidus zarówno w stanie stałym, jak również stało-ciekłym z małym udziałem fazy ciekłej. Wyniki przeprowadzonych badań mogą być zastosowane w symulacjach numerycznych w ramach projektowania i optymalizacji procesów formowania tiksotropowego. Analiza dotyczyła zarówno stopów aluminium (A356, 7075), jak również stali (M2). W pracy poddano analizie rozwój mikrostruktury globularnej w stanie stało-ciekłym w stopie stali.



Algorithms for the estimation of fatigue crack growth using energy method

MIECZYŚLAW SZATA, GRZEGORZ LESIUK

Institute of Materials Science and Applied Mechanics, Wrocław University of Technology, Poland

A new method of producing kinetic fatigue failure diagrams (KFFD) has been developed by the authors on the basis of experimental results obtained from the study of the hysteresis loop area. For experimental verification of KFFD the results of fatigue crack propagation studies for 41Cr4 (40H) and S355JR (18G2A) steels have been used.

Two kinds of kinetic fatigue failure diagrams have been produced. In the first diagram (the classic one), the stress intensity factor K that characterizes the intensity of deformation in the precrack zone ahead of a crack tip was used for building the diagram. In the second diagram (the new one), energetic parameter ΔH that corresponds to the searched energy dissipation of deformation was applied.

In contrast to the $da/dN - K_{\max}$ diagrams, in the $da/dN - \Delta H$ diagrams obtained for a given range of the crack growth rate no difference in failure kinetics has been found. It means that the energetic parameter ΔH describes fatigue crack growth rate regardless of stress ratio R in opposition to the force factor K_{\max} .

1. Introduction

Statistically, the most frequent reason of structure damage is the fatigue failure effect. For example, more than 70% of damages that concern cyclically working structures are caused by fatigue. Fatigue of materials is a particularly serious and dangerous kind of material destruction. The exploited structures may not exhibit any symptoms of increasing material decohesion for a long time. The description of the fatigue failure kinetics is very important for predicting fatigue crack growth lifetime.

The problem of material fatigue remains unresolved. Until now, the only well approved finding is the division of fatigue into 3 stages:

- phase I – a group of cyclic phenomena connected with the change of material properties (cyclic softening or hardening, etc.), dislocation motion at atomic level without breaking the bonds,
- phase II – the formation of submicrocracks (microstructurally short cracks) propagating from the surface layer into the bulk in the area of one or several grains,
- phase III – it covers the propagation of a main macroscopic crack (a subcritical one), which is initially stable and then reaches the speed of sound in a given material.

The contribution of a particular fatigue phase in the fatigue process depends on load level. Cracks are an inevitable result of the fatigue process running in the material as well as an inevitable consequence of technological, assembly and working conditions. Fracture mechanics becomes a very useful tool for estimating the time of

crack propagation. This relatively new and rapidly developing branch of science goes back to the second decade of the XX century. Its origin is closely connected with the series of disasters of “Liberty” ships. During the second world war, 1289 out of 4700 “Liberty” ships were destroyed. The use of a new welding technology contributed to the formation of cracks. A spectacular example was a half-and-half fracture of the T2 “Schenectady” tanker (Figure 1), 16th January 1943 which was in port in fine weather (air temperature $-3\text{ }^{\circ}\text{C}$, water $+4\text{ }^{\circ}\text{C}$).

Other well-known disasters of the structures caused by fatigue failure are as follows:

- destruction of a gas pipeline in Canada in 1958 along a few miles of its length,
- the Kings Bridge collapse (Melbourne, 1962),
- Mianus River Bridge collapse (28th June 1983) in Greenwich (USA) caused by corrosion and fatigue cracks growth; the result: 3 persons were killed and 5 people suffered injuries,
- Douglas DC-10-10 plane crash (19th January 1989) – United Airlines flight 23 Iowa State (USA); a result: 110 passengers were killed and 175 were injured,
- I-35W Mississippi in Minnesota State – bridge collapse (1st August 2007) result: 6 persons were killed, 100 were injured, and dozens of cars slid into the water (Figure 2), the bridge was opened in 1967.

These examples are only the representatives. Much more information can be found in papers [1, 3, 4] devoted to the analysis of similar disasters. The above-mentioned examples are the start point for proposing a new approach concerning the description of the fatigue failure process.



Fig. 1. Tanker “Schenectady” [3]

The description of kinetics of fatigue failure is very important for estimating fatigue lifetime of a component. The knowledge of crack propagation direction as well

as crack growth rate makes it possible to predict the lifetime by means of kinetic fatigue failure diagrams (KFFD). The diagrams present the crack growth rate as a function of the fracture mechanics parameters such as K (stress intensity factor), G (energy release rate), J -integral which control the fatigue failure process. KFFD diagrams make it possible to construct the approximate function for building a mathematical model which enables us to estimate crack growth period. The influence of stress ratio R on crack growth rate should be also taken into account. It should be underlined that only some structures maintain a stable value of R coefficient during working cycles. Therefore, the analysis of the influence of R coefficient on fatigue failure kinetics seems to be very reasonable. The lifetime of mechanical component of the structure is assumed to be a sum of the initiation process and precritical growth of fatigue cracks until they lose global stabilization. Structural materials always contain the defects of “a particular size which are characteristic for a given material and applied technology. At present, the size of the defect is introduced as a construction parameter and is used to calculate the prognostic lifetime (i.e. the time during which no damage to a particular structural component is done). Such approach makes it possible to resolve the problem of calculating the lifetime of a component of a structure conditioned by a precritical defect growth period from the dimension of construction parameter up to a critical defect size.



Fig. 2. Collapsed Mississippi River Bridge I35W [3]

A new method of constructing the KFFD has been presented. The method was based on the measurement results of hysteresis loop area for the isotropic body with an internal flat crack under cyclic loading. For experimental verification, the results of fatigue crack propagation studies for three types of steels have been used.

2. Formulas used for describing fatigue crack growth rate

The main way of describing the kinetics of fatigue failure in materials is the force approach. The force criterion, which is a local criterion, is frequently applied for the description of fatigue crack growth. Crack growth rate is a function of stress intensity factor K . The function was derived from experimental data and has an exponential shape in relation to K , as it has been shown in Paris' formula [4].

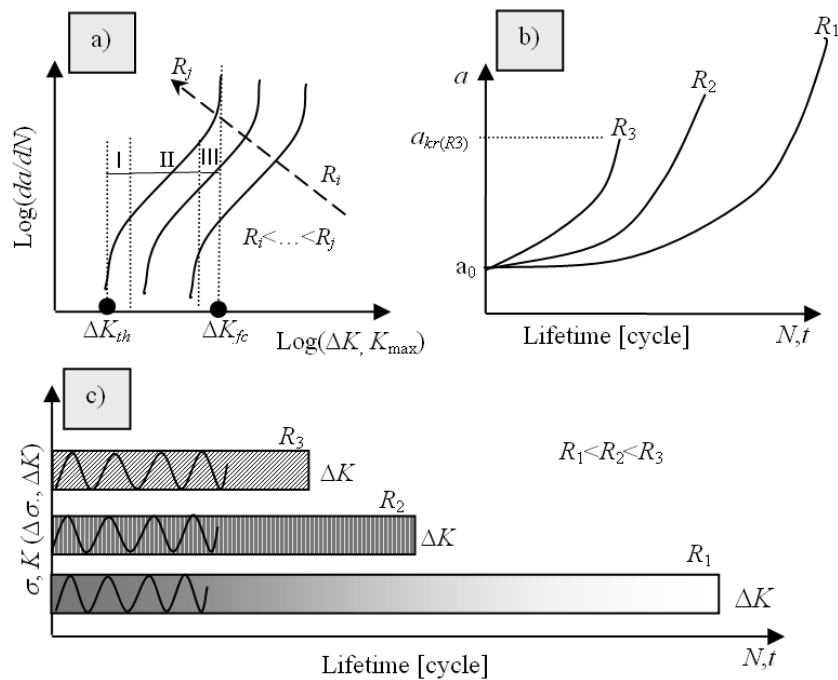


Fig. 3. Influence of stress ratio R on: a) the kinetic of fatigue failure performed on KFFD diagrams, b) crack extension against number of cycles, c) fatigue lifetime

Schematic presentation of the KFFD diagrams and the influence of stress ratio R on fatigue crack growth rate were presented in Figure 3. As it is seen in Figure 3a the curve of fatigue crack growth rate at a given R coefficient can be divided for three ranges marked as I, II, III. Within the first range, low crack growth rate changes from zero to about 10^{-9} m/cycle. The second one is the straight line range with a stable, average growth rate that runs from 10^{-9} to 10^{-6} m/cycle. Within the third range, the growth rate is higher than 10^{-5} m/cycle. Of course, the above-mentioned ranges are rather symbolic as they are interrelated with a given material and its properties as well as with environment and load. The left side of the first range is limited by the vertical asymptote ΔK_{th} which relates to the fatigue threshold ($\Delta K_{th} = K_{th,max} - K_{th,min}$). Below that threshold macroscopic long crack does not extend (except of short crack).

Subcritical (stable) crack propagation is terminated when the stress intensity factor K (SIF) reaches the critical value K_{fc} called as fatigue fracture toughness. Over that value, crack propagation rate is equal to the speed of sound. The influence of the stress ratio R is presented schematically in Figure 3a. The influence of R coefficient is especially noticeable when the range of stress intensity factor ΔK is close to ΔK_{th} and R coefficient is increasing. For higher values of R the threshold ΔK_{th} becomes evidently lower. The influence of R coefficient on fatigue crack lifetime is shown in Figure 3c.

Paris as the first introduced the functional relationship to cover experimental observation of incremental fatigue crack growth per cycle against an alternating applied stress $\Delta\sigma$, made on a variety of materials. In the literature so called Paris' law has the form:

$$\frac{dl}{dN} = C(\Delta K)^m. \quad (1)$$

where: $\Delta K = Y(l)\Delta\sigma\sqrt{\pi l}$, l is the length of crack, $Y(l)$ is the compliance function appropriate to the specimen geometry [5]. The constants C and m in Paris' law are treated as material constants and they can be easily determined when using geometrical interpretation of the relationship (1), in the following way. On double logarithmic coordinates the central part of the KFFD diagrams is linear. Constant C is the intersection point of the linear segment of kinetic fatigue failure diagrams (KFFD) with the vertical axis, and the exponent m is a tangent of this line (i.e. a slope of the straight line). The average value of the constant m is frequently in the range 2–5 and it is dimensionless. The constant C depends more significantly on the kind of materials and its values are in the ranges from 10^{-5} to 10^{-11} . Linear segments of kinetic fatigue failure diagrams (KFFD) are parallel due to the independence from stress ratio R . However, constant C , similarly to ΔK_{th} , is more sensitive to the changes and it depends on the value of stress ratio R . The values of C and m constants for Paris' law are collected in the Table 1.

Table 1. Approximate values of constants C and m for Paris' law for typical steels

Material	$R_e (R_{02})$ [MPa]	R_m [MPa]	C	m
18G2A steel	400	560	$2 \cdot 10^{-12}$	3
40H steel	780	980	$3.96 \cdot 10^{-12}$	2.97
20G steel	280	460	$2 \cdot 10^{-11}$	3
A533 steel for pressure containers	350	560–700	$2 \cdot 10^{-11}$	2.2
rustless steel (0.02% C, 18% Ni)	1700	1960	$8 \cdot 10^{-10}$	2.2
Al PA7 alloy	420	510	$7 \cdot 10^{-11}$	4

Having no proper kinetic fatigue failure diagram it is possible to obtain constants C and m for Paris' law from empirical formulas. In the literature [5] these constants are given as follows:

$$\begin{aligned} \log C &= 0.00483R_e - 12.432, \\ m &= 4.52 - 0.0026R_e, \end{aligned} \quad (2)$$

$$\begin{aligned} \log C &= 0.00556R_m - 13.726, \\ m &= 5.19 - 0.00297R_m. \end{aligned} \quad (3)$$

Due to the universality of the foregoing equations (the dependence only on R_e and R_m , and the independence from load parameters), fitting of these values is not always sufficient. The modification of the Equation (1) in relation to the influence of a stress ratio R can be expressed in the form of Forman Equation [4]:

$$\frac{da}{dN} = \frac{C(\Delta K)^m}{(1-R)K_c - \Delta K}. \quad (4)$$

The quantity K_c in the Equation (4) is equivalent to fracture toughness. If it is difficult to determine it, the stress intensity factor K_{IC} is often used ($K_c = K_{\max}$ for PSS-plane stress state (thin strips) or $K_c = K_{IC}$ in the case of PDS – plane deformation (strain) state). The exact calculation of the values of constants C and m requires the knowledge of kinetic fatigue failure diagrams for different values of stress ratio R . Another proposition was made by Walker:

$$\frac{da}{dN} = \frac{C_w}{(1-R)^{n_w}} (\Delta K)^{m_r}. \quad (5)$$

In the Walker's law, the constant C_w is fixed experimentally for different values of R . For $R = 0$ the value of C_w is equal to Paris' constant C . The power coefficient m_r , which is expressed by the relation $m_r = m + n$ is also determined by the extrapolation of crack growth rate data taken from kinetic fatigue failure diagram (KFFD). As it was mentioned earlier stress ratio R really affects ΔK_{th} . If R increases then ΔK_{th} , that is proper for a given material, decreases. Moreover, for the same material crack propagation is faster at higher value of R than at its lower value.

A regular influence of R coefficient on the threshold stress intensity factor ΔK_{th} was observed for different materials (Figure 4) [6, 7]. It is evident that at high values of R (close to 1) the start of failure takes place at lower values of stress intensity factor ΔK . In the literature one can find several empirical formulas for determining the fatigue threshold ΔK_{th} using the material properties obtained from the tension test. These equations are as follows [5]:

$$\begin{aligned}\Delta K_{th0} &= 11.17 - 0.0032R_m, \\ \Delta K_{th0} &= 11.40 - 0.0046R_e,\end{aligned}\quad (6)$$

where:

ΔK_{th0} means the value of ΔK_{th} at $R = 0$.

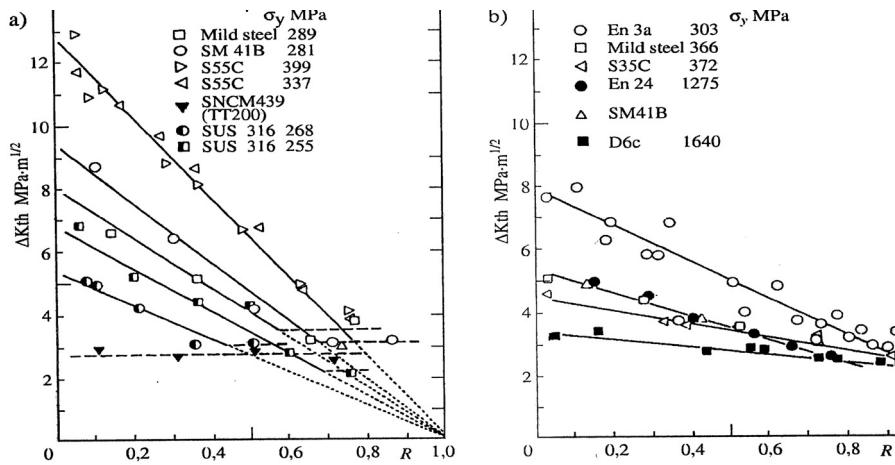


Fig. 4. Influence of stress ratio R on the threshold value ΔK_{th} . Open symbols relate to ferritic-perlitic steels, filled symbols-for martensitic steels whereas semi-filled symbols-for austenite steels [4]

There exist several other formulas for obtaining approximate values of ΔK_{th} for any value of stress ratio R , for instance [5]:

$$\Delta K_{th} = \Delta K_{th0} - BR, \quad (7)$$

where:

$$B = 10.39 - 0.0052 R_e.$$

The above considerations illustrate the way in which stress ratio R hampers the analytical description of crack propagation. The solution to this problem is the energy approach which can be applied in order to describe this process. In the diagrams $da/dN - \Delta H$ obtained for a given range of the crack growth rate no difference in failure kinetics was observed, in contrast to the $da/dN - K_{max}$ diagrams. It means that in contrast to the force factor K_{max} the energetic parameter ΔH describes synonymously the fatigue crack growth rate independently on stress ratio R .

3. Energetic description of fatigue failure kinetics

In order to determine the period N_s of a precritical crack propagation by means of the energy approach described in [8–11] the application of the first principle of

thermodynamics is required. Using the terms A , Q , W , K_e , Γ as a linear density [6] (divided by thickness B), namely $A^* = BA$, $Q^* = BQ$, $W^* = BW$, $K_e^* = BK_e$ we can present global energy balance in the following form:

$$A + Q = W + K_e + \Gamma, \quad (8)$$

where:

A – means the work done after N cycles of loading at applied stress σ_{zw} ,

Q – the heat input to the body during the loading,

W – deformation energy accumulated in the body after N loading cycles,

K_e – kinetic energy of the body,

Γ^* – damage energy associated with a free crack surface increment.

Assuming slow crack extension, no body heating and neglecting small changes of a kinetic energy (for low frequencies of cyclic loading) then after differentiating the equation (8) over the number of cycles we obtain:

$$\frac{\partial A}{\partial N} = \frac{\partial W}{\partial N} + \frac{\partial \Gamma}{\partial N}. \quad (9)$$

It was assumed more that

$$\Gamma = W_c + W_s, \quad (10)$$

where:

W_c – means an energy of cyclic plastic deformation,

W_s – a static component of energy equivalent to the product of $\sigma_{zw, \max}$ and crack length.

The components W_c and W_s both depend on the applied stress σ_{zw} and their sum Γ given by the Equation (10) can be reached on the way of different combinations of $\sigma_{zw, \max}$ and $\Delta\sigma_{zw} = \sigma_{zw, \max} - \sigma_{zw, \min}$. The term of $\sigma_{zw, \max}$ determines W_s , and W_s depends on $\Delta\sigma_{zw}$.

The term Γ can be defined as a maximum value of static energy component ($\Gamma = W_{s, \max}$) that initiate a cracking process without cyclic energy ($W_c = 0$).

The Equation (10) was transformed into the form:

$$\Gamma - W_s = W_c, \quad (11)$$

and then it was differentiated over a number of cycles, as follows:

$$\frac{\partial(\Gamma - W_s)}{\partial N} = \frac{\partial W_c}{\partial N}. \quad (12)$$

After a simple transformation we obtain

$$\frac{\partial(\Gamma - W_s)}{\partial N} = \frac{\partial(\Gamma - W_s)}{\partial S} \cdot \frac{\partial S}{\partial N} \quad (13)$$

Hence, the Equation (12) can be presented in the following form:

$$\frac{\partial(\Gamma - W_s)}{\partial S} \cdot \frac{\partial S}{\partial N} = \frac{\partial W_c}{\partial N} \quad (14)$$

After a transformation, the relationship for the free crack surface increment per one cycle loading is obtained:

$$\frac{\partial S}{\partial N} = \frac{\partial W_c}{\partial N} / \frac{\partial(\Gamma - W_s)}{\partial S}, \quad (15)$$

where:

$\partial S/\partial N$ – a free crack surface increment per one cycle loading,

S – a free crack surface.

Let us consider the terms W_c , Γ and W_s . The term $\partial W_c/\partial N$ represents the dissipation energy that relates to plastic deformation in one loading cycle ahead of a crack tip. In order to obtain the equation appropriate for constructing the experimental kinetic fatigue failure diagrams we use a simplified form [9] without accounting for the change of a function of crack-opening displacement δ . Then

$$\frac{\partial \Gamma}{\partial S} = \sigma_{plf} \varepsilon_{fc}, \quad (16)$$

where:

σ_{plf} – means cyclic yield stress,

ε_{fc} – critical deformation under cyclic loading.

Similarly, the term W_s can be expressed as

$$\frac{\partial W_s}{\partial S} = \sigma_{plf} \varepsilon_{f \max}, \quad (17)$$

$\varepsilon_{f \max}$ – maximum deformation during one cycle loading.

After substituting the Equations (16) and (17) in the Equation (13) we obtain:

$$\frac{\partial(\Gamma - W_s)}{\partial S} = \sigma_{plf} \varepsilon_{fc} - \sigma_{plf} \varepsilon_{f \max} = \sigma_{plf} \varepsilon_{fc} \left(1 - \frac{\varepsilon_{f \max}}{\varepsilon_{fc}} \right). \quad (18)$$

The following equations are satisfied for Panasiuk–Dugdale’s $\delta\kappa$ – model and for a plane stress state [2, 6]

$$\delta_{\max} = \frac{K_{I\max}^2}{E\sigma_{plc}}, \quad \delta_c = \frac{K_{fc}^2}{E\sigma_{plc}}, \quad \frac{\varepsilon_{\max}}{\varepsilon_{fc}} = \frac{\delta_{\max}}{\delta_c} = \frac{K_{I\max}^2}{K_{fc}^2}, \quad (19)$$

where:

K_{fc} – a cyclic fracture toughness,

$K_{I\max}$ – a maximum value of stress intensity factor.

The Equation (19) makes possible to express the Equation (18) in the form

$$\frac{\partial(\Gamma - W_S)}{\partial S} = \sigma_{plf}\varepsilon_{fc} - \sigma_{plf}\varepsilon_{f\max} = \sigma_{plf}\varepsilon_{fc} \left(1 - \frac{\varepsilon_{f\max}}{\varepsilon_{fc}}\right) = \sigma_{plf}\varepsilon_{fc} \left(1 - \frac{K_{I\max}^2}{K_{fc}^2}\right). \quad (20)$$

Denoting $W_c^{(1)} = \partial W_c / \partial N$ as the speed of the changes of plastic deformation energy dissipation ahead of a crack tip per one loading cycle ahead of a crack tip in one loading cycle, we obtain:

$$dS / dN = \frac{W_c^{(1)}}{\sigma_{plf}\varepsilon_{fc} \left(1 - K_{I\max}^2 / K_{fc}^2\right)}. \quad (21)$$

Due to the occurrence of the two crack surfaces – upper and lower ($S = 2Ba$) – formula for the crack propagation can be written as

$$da / dN = \frac{\alpha W_c^{(1)}}{B\sigma_{plf}\varepsilon_{fc} \left(1 - K_{I\max}^2 / K_{fc}^2\right)}. \quad (22)$$

where: $\alpha = 0.5$.

It seems that for estimating the influence of stress ratio R it is proper to construct the experimental kinetic fatigue failure diagrams $da/dN - \Delta H$ with energetic parameter ΔH that depends on $W_c^{(1)}$ equals:

$$\Delta H = W_c^{(1)} / B \left(1 - K_{I\max}^2 / K_{fc}^2\right). \quad (23)$$

It should be noticed that in all Equations (21–23) the output quantities such as dS/dN , da/dN and ΔH depend linearly on the term $W_c^{(1)} = \partial W_c / \partial N$ (the speed of the changes of plastic deformation energy dissipation ahead of a crack tip per one loading cycle).

3.1. Comparison of theoretical and fitting results

A classical constructing way the kinetic fatigue failure diagrams (KFFD) where both coordinates are dimensional, i.e. da/dN [m/cycle] and $K_{\max}(\Delta K)$ [MPa $\cdot\sqrt{m}$] is assumed. The middle part of these diagrams in double logarithmic coordinates is linear. A tangent m of this line (i.e. straight line slope) has dimension $m \left[\frac{\log(m/\text{cycle})}{\log(\text{MPa}\sqrt{m})} \right]$. The verification of line factors values should maintain their dimensions. The tangent a appears to be crucial. The values of the parameters m and b are shown in Table 2.

Table 2. The values of the parameters m and b in double logarithmic coordinates

for ΔH	m	b
12HMF	0.868	- 8.838
18G2A	0.968	- 11.514
40H(200)	1.303	- 13.009
40H(450)	1.376	- 13.118
40H(700)	1.301	- 13.078

Data presented in Table 1 concerns the rectilinear, middle part of the diagrams performed by the straight line and expressed by the equation $y = mx + b$, where

$$y = \log \frac{da}{dN}, \quad x = \log \Delta H.$$

Theoretical basis (Equations (22) and (23)), indicates that $m = 1$, i.e.

$$\frac{da}{dN} = \frac{1}{2\sigma_{plf}\epsilon_{fc}} \Delta H^m. \quad (24)$$

The logarithm of the Equation (24) has the form

$$\log\left(\frac{da}{dN}\right) = m \log \Delta H - \log(2\sigma_{plf}\epsilon_{fc}). \quad (25)$$

where:

m should theoretically equal "1".

As it was in the case of Miner's law, material does not want to generate "1"; for tested materials the value of this parameter changes in the range of 0.86 – 1.37 (Table 2). It is known from the theoretical considerations, that a free term in double logarithmic coordinates is smaller than zero. In the tests performed by the authors all the values of a free term " b " are smaller than zero (Table 2). Consequently, a qualitative agreement between theoretical and fitting models has been found out.

4. Experiment

In the experiment the compact tension specimens according to ASTM E 399-81 were tested. The determination of the energy dissipated in the unit volume of material is faced with many difficulties particularly in the case of high cycle fatigue. The hysteresis loop area is then very small and the algorithms should be of a great accuracy. This work has been realized with the help of a software package using the programming language Hewlett – Packard HP VEE version 4.0. The screen of computer during a testing procedure is presented in Figure 5. One can observe loading (forces) and the answer (displacements) diagrams. The ranges of replaceable MTS panels for the force (± 25 kN) and displacement (± 0.5 mm) are registered. A sinusoidal shaped loading diagram has been presented close the mean value level (3462.5 N) indicated in the diagram as zero.

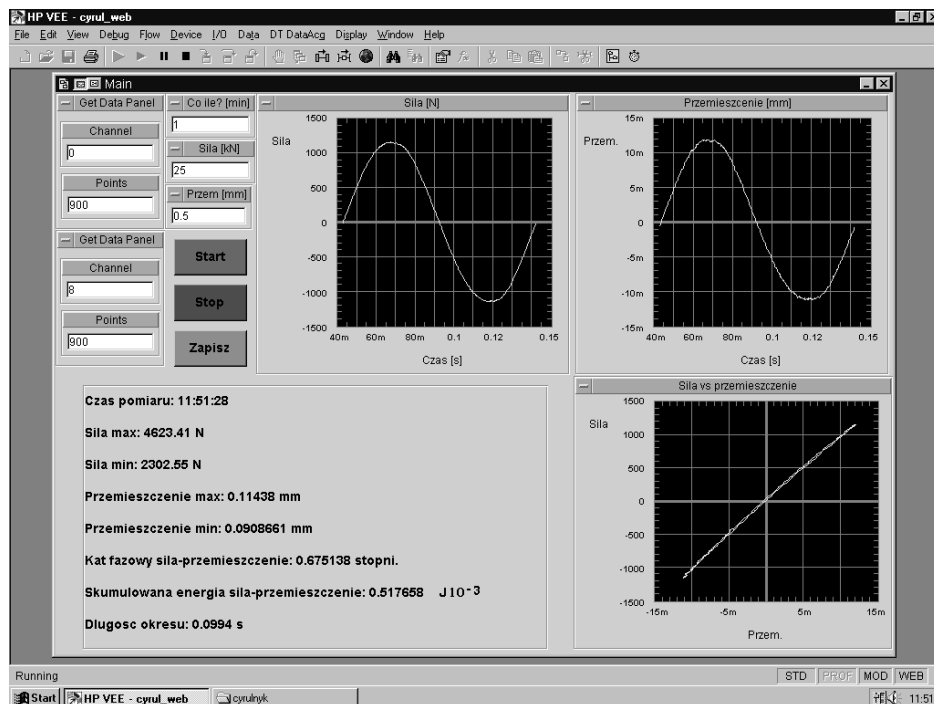


Fig. 5. Computer screen during tests [9]

Similarly, the displacement diagrams were shown around the mean values which can be determined on the basis of a maximum (0.11 mm) and minimum (0.09 mm) displacement values. The period T is equal to 0.1 s and the phase shift angle between a force and displacement is equal to 0.67° . The hysteresis loop in the coordinates force versus displacement corresponds to the energy for one cycle is equal to $0.51 \cdot 10^{-3}$ J.

5. Results and conclusions

Two kinds of kinetic diagrams for 40H steel have been constructed and performed in Figure 6 and Figure 7. In the first diagram the intensity of material cyclic deformation ahead of the crack tip was expressed by the stress intensity factor K , in the second one – dissipation of material plastic deformation energy was characterized by the energetic parameter ΔH .

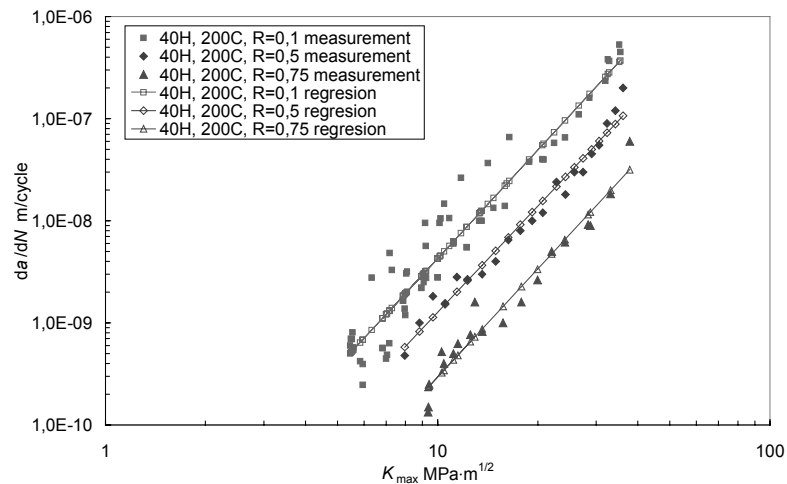


Fig. 6. Crack growth rate da/dN versus stress intensity factor K_{max} for different stress ratio R ; 40H steel, heat treatment 200 °C (classical diagram)

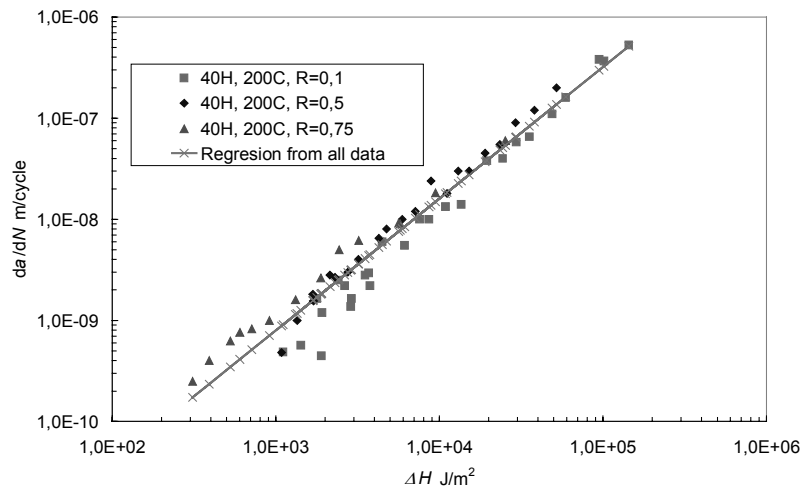


Fig. 7. Crack growth rate da/dN versus parameter ΔH for different stress ratio R ; 40H steel, heat treatment 200 °C (energetic diagram)

To illustrate fatigue crack growth rate behaviour in S355 (18G2A) steel for the sake of changing values of stress intensity factor the kinetic diagram in coordinates $da/dN - K$ was also constructed (Figure 8). According to our expectations the plots da/dN show the influence of stress ratio R on material resistance with relation to crack propagation.

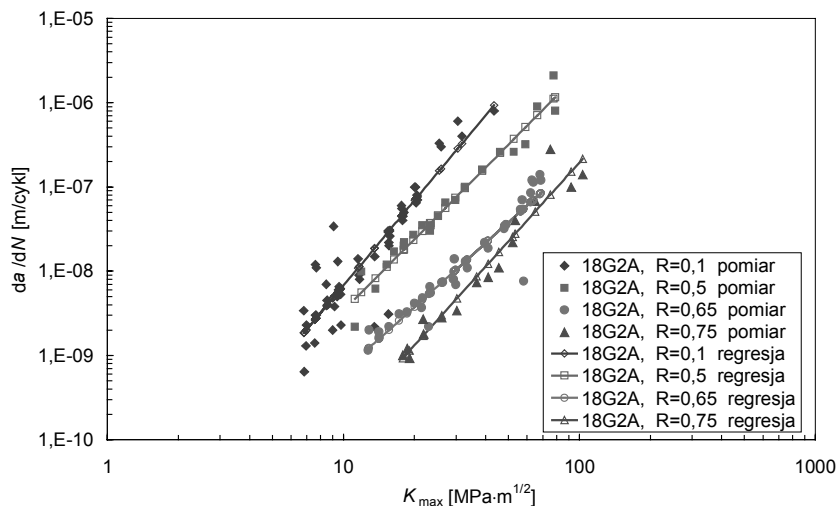


Fig. 8. Crack growth rate da/dN versus stress intensity factor K_{max} for different stress ratio R ; 18G2A steel (classical diagram)

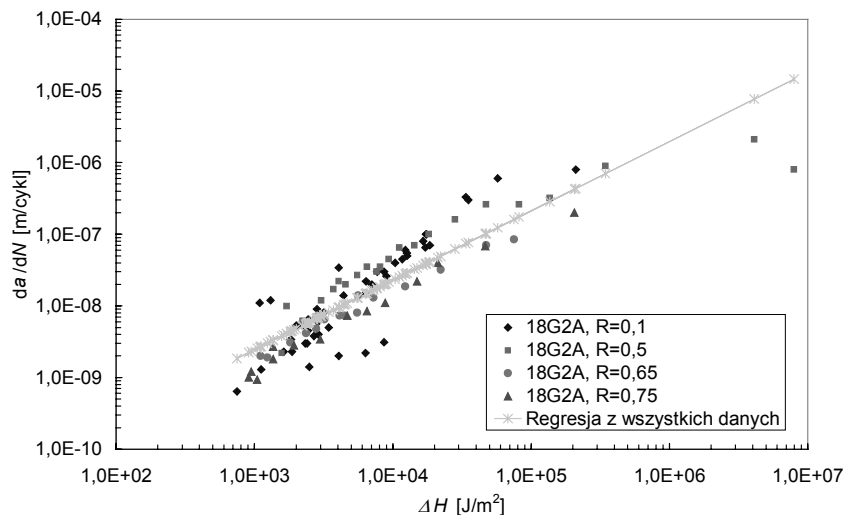


Fig. 9. Crack growth rate da/dN versus parameter ΔH for different stress ratio R ; 18G2A steel, (energetic diagram)

Kinetic diagram in coordinates $da/dN - \Delta H$ has also been constructed for S355 (18G2A) steel (Figure 9). Contrary to the classical diagrams $da/dN - \Delta K$ no differences in fracture kinetics was observed in the diagrams $da/dN - \Delta H$ when analyzing crack growth rate behaviour at different values of R coefficient. It means that unlike the force parameter ΔK , the energetic parameter ΔH explicitly describes fatigue crack growth rate, irrespective of stress ratio R .

Similar observations have been done when the diagrams $da/dN - K_{\max}$ was compared with diagrams in coordinates $da/dN - \Delta H$ for a given range of crack growth rate. It means that in contradiction to the force factor K_{\max} the energetic parameter ΔH describes synonymously the fatigue crack propagation rate irrespective of stress ratio R .

References

- [1] Babiarcz St., Dudek D.: *Chronicle of damages and disasters of main machines in polish opencast industry* (in Polish), Publishing House of Wroclaw University of Technology, Poland, Wroclaw, 2007.
- [2] German J., Biel-Gołaska M.: *Bases and application of failure mechanics in engineering problems* (in Polish), Instytut Odlewnictwa, Kraków, 2004.
- [3] Hayes B.: *Classic brittle failures in large welded structures*, Engineering Failure Analysis, Elsevier Science, Great Britain 1996, Vol. 3, No. 2, pp. 115–127.
- [4] Karolczuk A.: *Catastrophic results of fatigue fracture cracks of constructional materials* (in Polish), Transport Przemysłowy, No. 4, 2007.
- [5] Kocańda S., Szala J.: *Bases of fatigue calculation* (in Polish), PWN, 3rd ed., Poland, Warsaw, 1997.
- [6] Neimitz A.: *Fracture Mechanics* (in Polish), PWN, Poland, Warsaw, 1998.
- [7] Savruk M.: *Koeficienty intensywności naprężenia w telach z treszczinami*, t. 2. Naukowa Dumka, Kijev, 1988.
- [8] Stosiak M., Szata M.: *Experimental studies methodology in fatigue crack description* (in Polish), Górnictwo Odkrywkowe, Vol. 45, 2003, No. 2–3.
- [9] Szata M.: *Modeling of fatigue crack growth using energy method* (in Polish), Publishing House of Wroclaw University of Technology, Poland, Wroclaw, 2002.
- [10] Szata M., Lesiuk G.: *Fracture mechanics models in aspect of transportation systems degradation* (in Polish), In: *Computer systems aided science, industry and transport*, TRANSCOMP 2007. 11 International Conference, Zakopane, 3–6 December 2007, Vol. 2, Radom : Institute for Sustainable Technologies, 2007.
- [11] Yao Y., Fine M.E., Keer L.M.: *An energy approach to predict fatigue crack propagation in metals and alloys*, Int. J. Fract., Vol. 146, 2007, pp. 149–158.

Algorytmy szacowania wzrostu pęknięć zmęczeniowych metodą energetyczną

Na podstawie wyników pomiaru pola pętli histerezy energii odkształcenia próbki ze szczeliną typu compact w procesie cyklicznego obciążenia przedstawiono nową metodę budowania kinetycznych wykresów zmęczeniowego pęknięcia. Do weryfikacji doświadczalnej wykorzystano

wyniki badania rozwoju szczeliny zmęczeniowej w stali S355JR (18G2A) i 41Cr4 (40H). Analizowano wpływ współczynnika asymetrii cyklu w opisie klasycznym i proponowanym przez autorów. Wykresy klasyczne wykonano wykorzystując współrzędne $da/dN - K_{\max}$. Drugi rodzaj wykresów wykorzystuje parametr energetyczny ΔH odpowiadający dyssypacji energii odkształcenia próbki. W przeciwieństwie do wykresów $da/dN - K_{\max}$, na wykresach $da/dN - \Delta H$, otrzymanych dla danego zakresu prędkości rozwoju pęknięcia szczeliny, nie zaobserwowano różnic w kinetyce pęknięcia. Oznacza to, że w odróżnieniu od siłowego parametru K_{\max} parametr energetyczny ΔH opisuje prędkość zmęczeniowego rozwoju szczeliny, niezależnie od współczynnika asymetrii cyklu R .



The results of the so far performed investigations of Al-Cu butt cold pressure welding by the method of upsetting

H. WOŹNIAK

Poznań University of Technology, ul. Piotrowo 3, 61-138 Poznań, Poland

The paper presents the results of the author's investigation obtained so far concerning the relationships between the properties of the Al-Cu weld and the surface condition prior to welding, the properties of the welded material and the process of plastic deformation of the materials being welded. The investigation performed has shown evolution modification of the geometrical structure of the surface and the layers below it during the approximation of the welded surfaces to each other. After the first physical contacts of the surface irregularities and their squashing, new irregularities of larger sizes arise as a result of the mechanism of plastic deformation of grains in the surface layer. The new geometrical structure of the surface thus formed has no features of similarity to the primary structure. It has been found that modelling of the approximation of the welded surfaces to each other, from the first physical contact of the surface irregularities to the distance of atomic force interaction in the methods of metal forming, should incorporate evolution change of the surface geometrical structure including the phenomenon of closing the voids. Initial computer simulations of the Al-Cu cold pressure welding process confirm the possibility of applying the finite element method (FEM) for the determination strains and stresses present in the welded materials.

Keywords: *metal forming, cold pressure welding, Al-Cu joints*

1. Introduction

The development of the technology of joining metals by cold metal forming depends on the scientific description of the phenomena accompanying the preparation of the surfaces to be welded and welding itself. It is worth noting here that cold pressure welding is a technology which can economically and environmentally compete with the technologies involving heat supply or heat generation in intensive mechanical friction of the materials being welded.

Learning and scientific description of the phenomena taking place in the surface layer when preparing it and the description of the phenomena accompanying cold pressure welding, i.e. approaching of the welded surfaces to each other till a metallic bond is obtained require an interdisciplinary team of investigators, especially mechanics, physicists and chemists.

The author, due to his investigation possibilities, has concentrated on the cold pressure welding of aluminium with copper (Al-Cu) [1–5], searching for the relations between:

- surface condition prior to the pressure welding,
- properties of the material to be welded,

- the process of plastic deformation of the material to be welded, ensuring the formation of a metallic bond.

The paper presents some selected results of investigations performed so far.

2. Description and the results of the investigation

2.1. The method and conditions of welding

The pressure-welding mode shown in Figure 1 has been adopted in the investigation. It is called butt cold pressure welding by the method of upsetting. The materials used were aluminium, Al (HB = 23) and copper, Cu (HB = 82) in the form of cold drawn rods with the diameter of 23 mm corresponding to the diameter of the samples. The samples were cold pressure welded on a hydraulic press with the force of $P \leq 630$ kN and with two ram speeds: 30 mm/s and 50 mm/s.

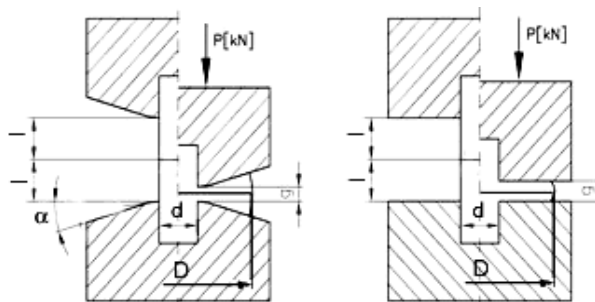


Fig. 1. A diagram of butt cold pressure welding of rods by the method of upsetting with conical and flat dies; angle α can be positive or negative

The variable parameters were: the way of preparation of the sample faces (turned, planed, milled, brushed), material condition (consolidated, recrystallized), die geometry ($\alpha = 0^\circ$, $\alpha = 16^\circ$), slenderness ratio of the sample free ends prior to welding (l/d), degree of deformation of the welded materials $\varepsilon = \ln(2l/g)$, welding velocity ($v = 30$ mm/s, $v = 50$ mm/s).

2.2. Experimental investigation results and their interpretation

In the experimental selection of the parameters of the sample surface preparation for cold pressure welding and in the selection of the parameters of cold pressure welding, it has been found that the trials of joining Al and Cu by this method brought two kinds of results: lack of metallic bond or metallic bond with the required strength. Such experiment results allowed to the elimination of the metallic bond strength factor from the program of the further investigation. This resulted in a significant reduction of the number of trials. The diameter of the metallic bond in the weld was larger than

that of the samples but smaller than the diameter of the flange and amounted $(1.2-1.4)d$ – Figure 2. In as few as 0.4% of cases the bond diameter was smaller than that of the samples.

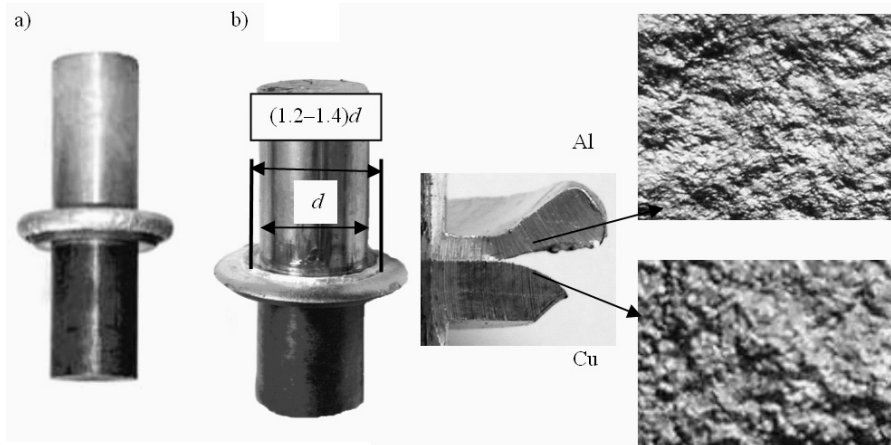


Fig. 2. Cold pressure welding: a) obtained sample with flange and b) flange structures in unwelded points Al and Cu on the flange periphery were separated manually by means of a wedge shaped tool

No traces of local metallic bonds (welds) – or traces of motion friction have been observed on the unwelded surfaces in the flange – Figure 2b. A similar structure was found in the unwelded surfaces of the samples which had been immersed in anhydrous alcohol and dried with an electric drier prior to the cold pressure welding.

Assessment of the joint strength

The joints strength was assessed in tensile, bending and rolling tests.

In tensile tests the samples underwent plastic deformation till breaking, always on the Al side beyond the area of the joint – Figure 3. The strength of the joint was, therefore, higher than that of the initial material. This is due to more plastic deformation and, consequently, higher hardening of the material within the joint as shown in the diagram of HV hardness increase – Figure 4.

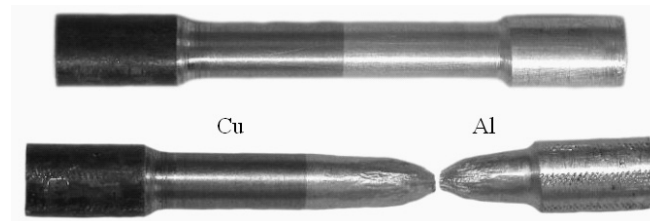


Fig. 3. A view of an Al-Cu sample before and after tensile test [4]

In the tests of bending by 90°, too, the samples did not break in the weld (Figure 5). The shift of the weld and the material during the process of bending are on the Al side at a very small distance from the Al-Cu boundary. Figure 6 and 7 show the deformation of cold pressure welding during longitudinal rolling for small and large deformation respectively. The material cracks on the Al side as in tensile test.

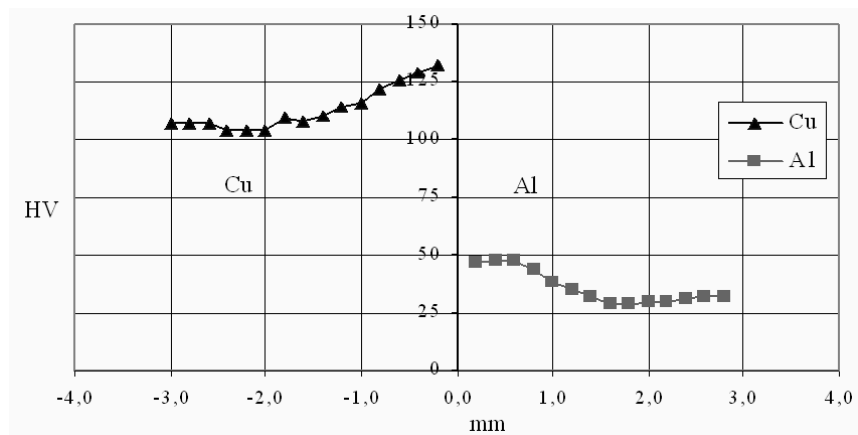


Fig. 4. Distribution of HV0.1 hardness measured in the sample axis. Distance from the place of joining, mm

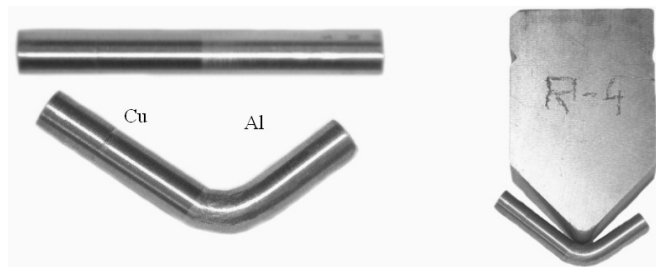


Fig. 5. A view of a cold pressure welded Al-Cu sample before and after 90° bending test [4]



Fig. 6. Al-Cu sample after longitudinal rolling with a small cold work in each pass [4]

Examining the fracture (Figure 7b), one can conclude that metallic bond has been obtained in the whole surface.

Scanning microphotography of the fracture (Figure 8) indicates clearly plastic character of the sample cracking.

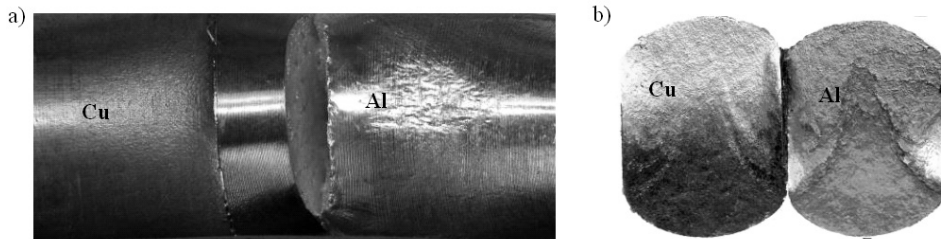


Fig. 7. Al-Cu sample after longitudinal rolling with maximum cold work in each pass:
a) crack in the weld on the Al side, b) a view of the fracture

Microanalysis of the chemical composition has also been performed on the fracture on the Cu side (Figure 8). The presence of Cu indicates diffusion character of the cold pressure welding. These problems will be the object of further investigation.

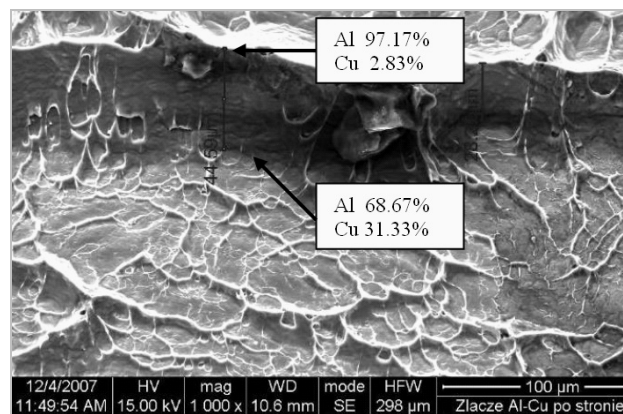


Fig. 8. View of the fracture of a sample broken in a rolling test; chemical composition microanalysis has been performed on the Cu side of the fracture by means of a scanning microscope

The influence of the sample butting face structure parameters prior to cold pressure welding and the upsetting parameters on the cold pressure welding:

1. The influence of the butting face parameters on the cold pressure welding effect was examined on samples with the following butting faces: turned ones, planed ones, milled ones, brushed ones. The Al and Cu samples with brushed surfaces ($R_a = 0.54 \mu\text{m}$, $R_z = 3.0 \mu\text{m}$, $R_t = 3.9 \mu\text{m}$, $S_m = 138 \mu\text{m}$) have not joined during the welding trials.

On the other hand, Al and Cu samples with turned, planed and milled surfaces joined in the same upsetting conditions although the geometrical structures (roughness) of the surfaces differed significantly.

As an example, Figure 9 shows the structures of planed and milled Cu surfaces. The average roughness parameters of the turned surface were: $R_a = 0.7 \mu\text{m}$, $R_z = 3.6 \mu\text{m}$, $R_t = 4.7 \mu\text{m}$, $S_m = 112 \mu\text{m}$.

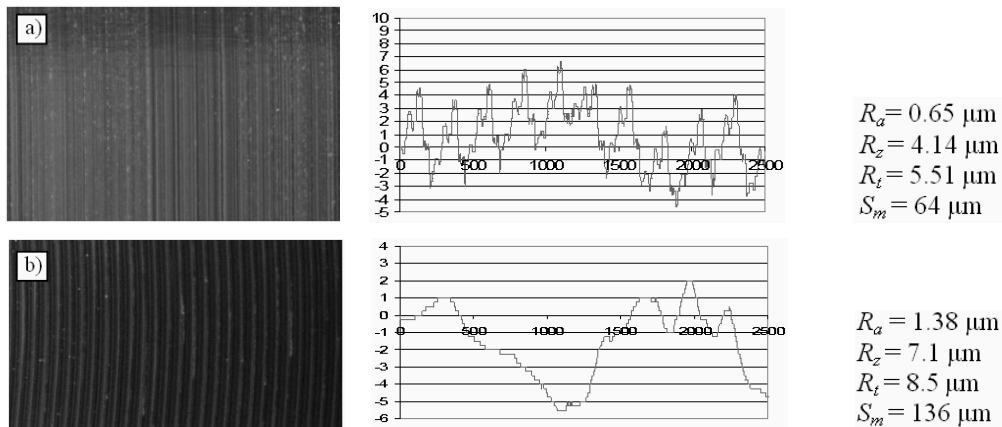


Fig. 9. Geometrical structures of Cu sample butting faces prior to cold pressure welding: a) a planed surface, b) a milled surface

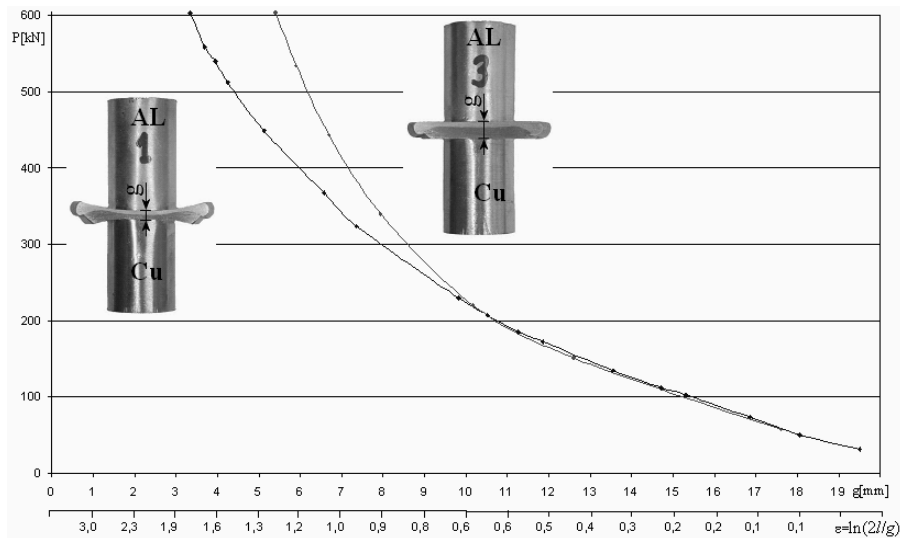


Fig. 10. Examples of the force curves in cold pressure welding with conical and flat working surface dies

2. The investigation of the influence of the upsetting parameters on the effect of cold pressure welding have shown that:

- Al and Cu samples got welded when the value of the quotient $l/d \geq 0.22$ and the deformation during upsetting was $\varepsilon = \ln(2l/g) \approx 1.4$. It can be supposed that the reason

why the samples did not get welded if the quotient $l/d < 0.22$ was too small volume of freely upset material when the final texturing of the structures of the welded materials in the contact zone took place.

- Cold pressure welding by means of conical dies significantly increases the value of material deformation as compared to upsetting with flat dies with the same value of the upsetting force (Figure 10). This is advantageous considering tool life and the amount of technological waste.

- No differences have been observed in the process and in the results of cold pressure welding of Al and Cu at the press ram speeds of $v = 30$ and 50 mm/s.

The results of the initial computer FEM simulations

FEM simulation was carried out on MSC.Marc as axisymmetrical mechanical model. The SHEAR friction model was applied with the following coefficients of friction: 0.8 between Cu and Al and 0,1 between the punches and the deformable material. The initial computer simulations of Al-Cu cold pressure welding confirm the possibility of application of the Finite Element Method (FEM) for the determination of strains and stresses present in the welded materials. The simulations were performed with aluminium and copper samples in work hardened condition and in recrystallized one (Figure 11).

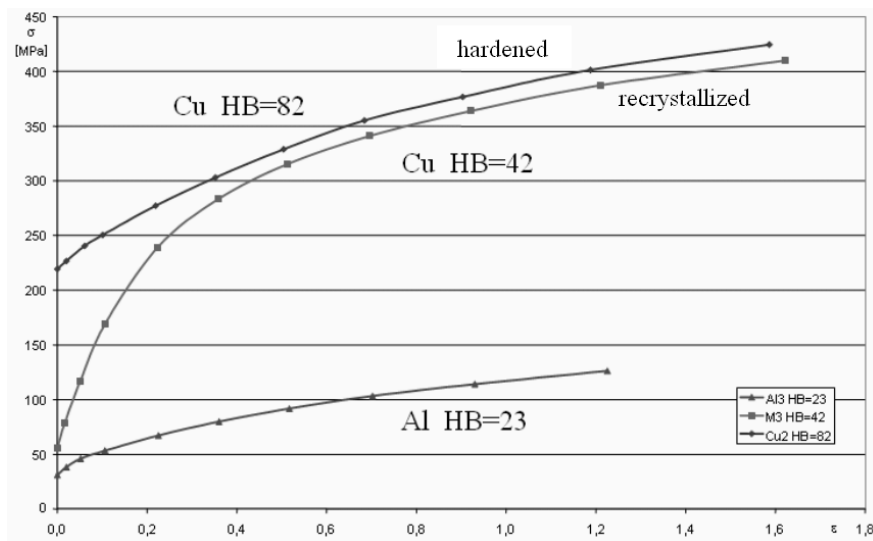


Fig. 11. Work hardening curves of the materials used in the investigation

The dimensions of the samples were the same as in the experiment. A very good shape conformance of the freely flowing surfaces and the Al-Cu contact surfaces in FEM has been obtained as well as welding forces of the virtual samples with the forces measured during the experiment (Figure 12).

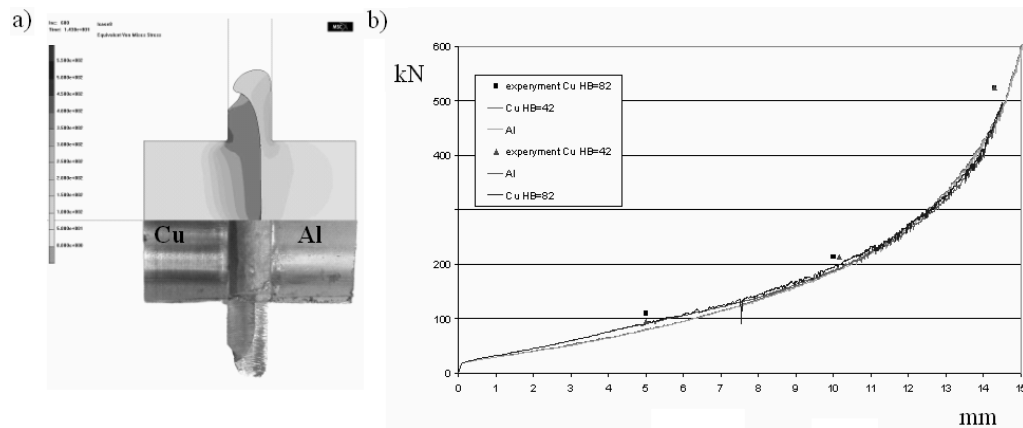


Fig. 12. Shape comparison of a virtual sample to a real one a) and a comparison of the welding force curves b). The continuous lines are simulation results while the plotted points are the results of the welding force measurements in cold pressure welding of aluminium samples to copper ones in work hardened condition and in recrystallized one

3. The results of the analysis of evolution change of the surface geometrical structure during the process of cold pressure welding

The surface approaching each other (“matching”) is a process of continuous plastic deformation of surface irregularities when upsetting the free ends of the samples. The matter is difficult to describe quantitatively because, in the author’s opinion, two kinds of surface irregularities should be considered, namely:

- primary surface irregularities, i.e. ones formed in the process of preparation for the cold pressure welding – Figure 9 and 13a,
- secondary surface irregularities, i.e. the ones which form during the cold pressure welding process (even if the primary irregularities are close to zero), Figure 2b and 13.

The primary irregularities are related to the technology of surface preparation and they deform (flatten) most intensely in the first phase of cold pressure welding. In the final phase, the primary irregularities disappear. They have less influence on the final result of cold pressure welding than the secondary irregularities.

The secondary irregularities are a result of deformation of the individual grains making up the surface to be welded. The process takes place simultaneously with the deformation of the primary irregularities and it accompanies the surfaces’ approaching each other. The intensity of the surface layer restructuring increases as the depth of the substrate plasticization grows. At the final stage of the surfaces approaching each other, the secondary structure has no features of similarity to the primary structure – Figure 13.

For comparison, Figure 14 shows the geometrical structure of the surface of a Cu sample upset in a frictionless test. The initial surface was turned $R_a = 1.73 \mu\text{m}$.

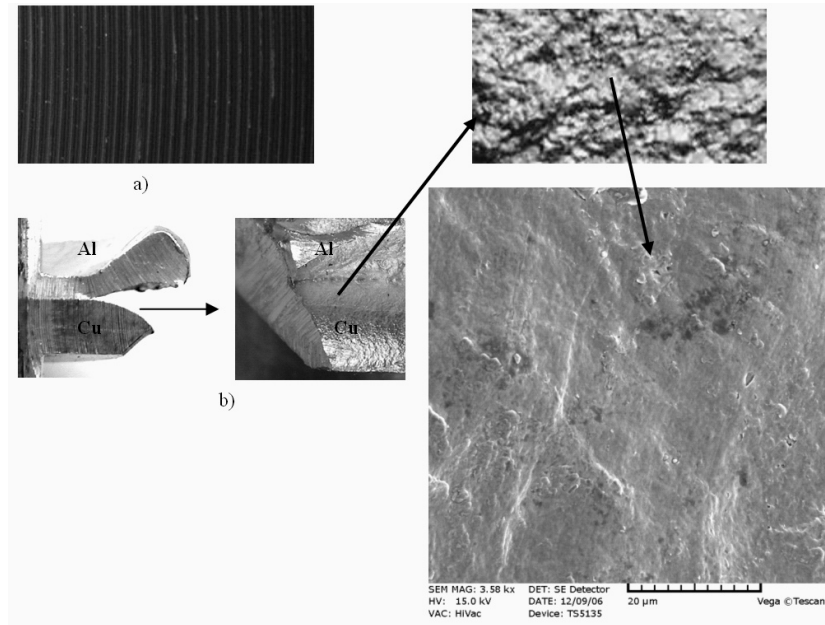


Fig. 13. Surface structure (Figure 9b) prepared for cold pressure welding a) and surface structure from the region of the joint b)

The test was performed on an INSTRON testing machine in accordance with the recommendations for the determination of the cold work curves $\sigma_p(\varepsilon)$. The relieves on the front faces of the samples were filled with paraffin.

The geometrical structure of the surfaces after upsetting did not show traces of the primary structure. The lack of traces of contact of the vertices of the irregularities with the pressing plates confirms the progress of the frictionless test.

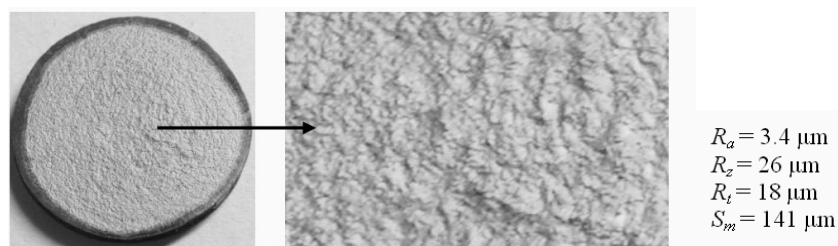


Fig. 14. Geometrical structure of the surface of a Cu sample upset in a frictionless test; the initial surface turned $R_a = 1.73 \mu\text{m}$

There is a clear similarity between the surface formed in the conditions of outer hydrostatic pressure due to the paraffin (Figure 14) and the surface formed during cold pressure welding (Figure 2b and 13b).

It should be pointed out here that to learn the evolution of the welded surface geometrical structure is an important thing. At the final stage, the surface irregularities cause a state in which areas of physical contact and isolated spaces-voids, filled or not filled with air, appear next to each other. Closing of the voids is possible provided that they are subjected to triaxial external pressure. If the possibility of further plastic deformation of materials in the welding zone is limited and a hydrostatic pressure, p , is made within it, assuming that both the void and the material surrounding have spherical shapes with the radii of R and r , respectively, plasticization of the material around the void (on the r radius) would take place provided that [6]

$$p \geq \frac{2}{3} \cdot \sigma_p \left(\frac{R^3}{r^3} - 1 \right). \quad (1)$$

The above formula indicates that “closing a void”, i.e. when $r \rightarrow 0$ in hydrostatic pressing requires a pressure increasing up to $p \rightarrow \infty$. Therefore, completion of cold pressure welding on the whole surface is possible when voids are surrounded by triaxial uneven pressure and an adequate state of strain.

Experiment results confirm the relationship between the force compressing the welded surfaces and plastic deformation of the surfaces during the welding process. For example, the application of conical dies (Figure 1) causes bond of metals with more deformation of the welded surfaces (due to lower friction) but with a smaller force than in the case of the use of flat dies – Figure 10.

4. Conclusions

1. A scientific description of the phenomena taking place both in the preparation of surfaces for cold pressure welding and in welding itself is a condition of the development of the technology bonding metals and their alloys by the methods of cold plastic forming.

2. Learning and scientific description of the phenomena taking place in the surface layer during its preparation and description of those accompanying welding require an interdisciplinary team of researches, especially mechanics, physicists and chemists.

3. The investigation performed has shown evolution rebuilding of the geometrical structure of the surface layer and the subsurface ones when the welded surfaces approach each other.

4. It has been found that, after the first physical contacts of the surface irregularities of the two welded materials and after the first phase of plastic flattening of those irregularities, new larger irregularities arise; they are an effect of the mechanism of plastic deformation of the grains in the surface layer and in the subsurface ones.

5. The new geometrical surface structure formed in this way has no features of similarity to the primary structure.

6. It has been determined that the evolution change of the geometrical surface structure, as well as the phenomenon of closing the voids should be taken into consideration in modelling the surfaces approaching each other.

7. Preliminary computer simulations of Al-Cu cold pressure welding confirm that the Finite Element Method (FEM) can be applied to determine the strains and stresses present in the cold pressure welded materials.

References

- [1] Woźniak H.: *Assessment of Cu-Cu and Al-Cu welds made by cold pressure welding method*, Metal Forming, No. 1, 2004.
- [2] Woźniak H.: *The application of the method of butt cold pressure welding of Al-Cu in the manufacture of energetic cable ends*, Materials of the 2nd International Scientific and Technical Conference, Poznań, 4–5.11.2004, Manufacturing '04, Poznań University of Technology, 2004.
- [3] Woźniak H.: *Investigation of butt cold pressure welding parameters and assessment of the weld strength*, Paper, 7th Seminar of the Metal Forming Section of Machine Construction Commission of the Polish Academy of Sciences, Poznań University of Technology, 16.12.2004.
- [4] Woźniak H. et al.: *The influence of the temperature on the strength of a butt Al-Cu bond obtained by the method of cold metal forming*, Metal Forming, No. 4, 2005.
- [5] Woźniak H.: *Modification of the surface structure of butt welded Al and Cu rods bonded by the method of cold upsetting*, Paper, 9th Seminar of the Metal Forming Section of Machine Construction Commission of the Polish Academy of Sciences, Poznań University of Technology, 14.12.2006.
- [6] Höganäs: *AB Höganäs Handbook for sintered components*, Handbook 2, 1997.

Wyniki dotychczasowych badań spajania doczołowego na zimno Al-Cu metodą spęczania

W referacie przedstawiono dotychczasowe wyniki badań autora odnoszące się do związków pomiędzy własnościami spoiny Al-Cu i stanem powierzchni przed spajaniem, własnościami materiału spajanego oraz przebiegiem odkształcania plastycznego spajanych materiałów. Przeprowadzone badania wykazały ewolucyjną przebudowę struktury geometrycznej powierzchni i warstw podpowierzchniowych podczas zbliżania do siebie powierzchni spajanych. Po pierwszych fizycznych kontaktach nierówności powierzchni i ich plastycznym zgniataniu powstają nowe nierówności, będące efektem mechanizmu odkształcania plastycznego ziaren w warstwie wierzchniej. Powstała w ten sposób nowa struktura geometryczna powierzchni pozbawiona jest cech podobieństwa do pierwotnej struktury. Stwierdzono, że ewolucyjna zmiana struktury geometrycznej powierzchni, łącznie ze zjawiskiem zamykania pustek, powinny być uwzględnione w modelowaniu przebiegu zbliżania do siebie powierzchni spajanych. Wstępne symulacje komputerowe przebiegu spajania Al-Cu potwierdzają możliwość zastosowania metody elementów skończonych (MES) do wyznaczania odkształceń i naprężeń panujących w spajanych materiałach.

